ulm university universität
uulm

Scattering in Non-Stationary Mobile-to-Mobile Communications Channels

DISSERTATION

zur Erlangung des akademischen Grads eines

DOKTOR-INGENIEURS
(DR.-ING.)

der Fakultät für Ingenieurwissenschaften,
Informatik und Psychologie der Universität Ulm

von

Michael Walter
aus Ulm

Gutachter:	Prof. Dr.-Ing. Robert Fischer
	Prof. Dr.-Ing. Uwe-Carsten Fiebig
Amtierende Dekanin:	Prof. Dr. Tina Seufert

Ulm, 01. Dezember 2015

Vorwort

„Φύσις κρύπτεσθαι φιλεῖ."
- Ἡράκλειτος

Gerade weil sich die Natur gerne verbirgt, macht die Erforschung derselben sehr viel Spaß. Die vorliegende Dissertation entstand während meiner Tätigkeit als wissenschaftlicher Mitarbeiter am Institut für Kommunikation und Navigation des Deutschen Zentrums für Luft- und Raumfahrt in Oberpfaffenhofen. Die Grundlage für die Ergebnisse dieser Dissertation bilden eine Fahrzeug-Fahrzeug und eine Flugzeug-Flugzeug Messkampagne. Für die Gelegenheit solch komplexe und interessante Messkampagnen mitzugestalten und auch für die Unterstützung während meiner Promotion, möchte ich mich deshalb bei meinen Gruppenleitern Dr. Michael Schnell und Dr. Armin Dammann bedanken.

Der aeronautische Teil der Arbeit basiert zu großen Teilen auch auf Ergebnissen aus einem Drittmittelprojekt mit der Firma Rohde & Schwarz. Für die erfolgreiche Zusammenarbeit und die Erlaubnis, die hier gezeigten Messdaten in der Dissertation verwenden zu können, bedanke ich mich.

Für die Betreuung der Dissertation sowie die hilfreichen Kommentare geht mein Dank an Prof. Robert Fischer, der mir ermöglichte an der Uni Ulm zu promovieren. Des Weiteren bedanke ich mich bei Prof. Uwe-Carsten Fiebig, der in seiner Funktion als Abteilungsleiter und Zweitgutachter mit fachlichen Diskussionen zur Entwicklung des Themas beigetragen hat. Für die Einladung und Zusammenarbeit während eines dreimonatigen Forschungsaufenthaltes am Georgia Institute of Technology in Atlanta würde ich gerne Prof. Alenka Zajić meinen Dank aussprechen. Ebenso bedanke ich mich bei Prof. Fleury für den Aufenthalt und die fruchtbaren Diskussionen an der Universität Aalborg sowie bei Priv.-Doz. Thomas Zemen für die Einladung ans Telekommunikationsforum des FTW und der TU Wien als auch für die gute Zusammenarbeit bei den Publikationen.

Für die vielseitige Unterstützung bei der Vorbereitung und Durchführung der zwei Messkampagnen danke ich den DLR Forschungsflugabteilungen in Braun-

schweig und Oberpfaffenhofen, Rücker Aerospace und allen daran beteiligten Personen, insbesondere Thomas Jost, dem Meister der Messkampagnen. Ohne die Unterstützung aller involvierten Kollegen wären solche aufwändigen Messkampagnen nicht möglich gewesen!

Besonderer Dank gilt Ulrich Epple, meinem Bürokollegen, für die schöne gemeinsame Zeit in unserem Büro sowie Dmitriy Shutin, der viele theoretische Herleitungen mit mir zusammen erarbeitet hat. Ferner danke ich Nicolas Schneckenburger, Christian Gentner, Snježana Gligorević, Martin Frassl, Michael Lichtenstern, María García Puyol, Sinja und Kai Wendlandt, Nico Franzen, Michael Angermann und Seunghwan Kim für die fachlichen Diskussionen und Aufmunterungen ebenso wie für das angenehme Arbeitsumfeld während der Promotionszeit.

Abschließend möchte ich mich bei meinen Eltern und meinem Bruder für deren ununterbrochene Unterstützung auf meinem bisherigen Lebensweg bedanken. Da meine Eltern meine nicht enden wollenden Fragen im Kindesalter unermüdlich beantworteten, ist die Neugier auf die Geheimnisse der Natur bereits früh geweckt worden.

Gilching im Februar 2016,

Michael Walter

Kurzfassung

Das Ziel dieser Dissertation ist Einführung eines nicht-stationären Modells für Kanäle zwischen zwei mobilen Teilnehmern. Durch den Fortschritt in der drahtlosen Nachrichtentechnik, werden Kommunikationssysteme für die Informationsübertragung zwischen Basisstation und mobilen Teilnehmern durch solche für die Informationsübertragung zwischen mobilen Teilnehmern untereinander komplementiert.

Im Automobilsektor werden Kommunikationssysteme zwischen zwei mobilen Teilnehmern dazu verwendet intelligente Verkehrssysteme zu entwickeln. Eine solche Technologie zielt darauf ab den Verkehr sicherer und effizienter zu gestalten, indem Sensordaten zwischen Fahrzeugen übertragen werden. Im aeronautischen Sektor überträgt ein Kommunikationssystem zwischen zwei mobilen Teilnehmern z.B. die Positions- und Geschwindigkeitsinformationen der Teilnehmer untereinander, so dass der Flugverkehr enger gestaffelt werden und somit eine höhere Verkehrsdichte erreicht werden kann.

Stochastische Modelle für Kanäle zwischen Basisstation und mobilen Teilnehmern basieren auf der Annahme, dass der Kanal im weiteren Sinne stationär ist und unkorreliertes Streuverhalten besitzt. Es wurde jedoch gezeigt, dass viele Kanäle zwischen zwei mobilen Teilnehmern kein solches Verhalten zeigen, insbesondere der Fahrzeug-Fahrzeug- und der Flugzeug-Flugzeug-Kanal. Der Bedarf für neue Modelle ist daher auf die Tatsache zurückzuführen, dass die Kanäle zwischen Basisstation und mobilem Teilnehmer fundamentale Unterschiede zu den Kanälen zwischen zwei mobilen Teilnehmern besitzen.

Um die Einschränkungen der gegenwärtigen Kanalmodelle aufzuheben, wurden zwei Messkampagnen durchgeführt, um sowohl den Fahrzeug-Fahrzeug- als auch den Flugzeug-Flugzeug-Kanal zu charakterisieren. Die Messungen bestätigen, dass die Kanäle nicht stationär sind. Anschließend wird ein theoretisches Modell auf Basis der Messdaten entwickelt. Das verwendete Modell ist ein geometrisch-stochastisches Kanalmodel und damit aus zwei Teilen aufgebaut. Im geometrischen Teil werden mathematische Beschreibungen für Verzögerungungszeit und Dopplerfrequenz hergeleitet. Im stochastischen Teil ermöglichen diese Beschreibungen ge-

schlossene Lösungen für die benötigten Wahrscheinlichkeitsdichten zu berechnen. Das hier eingeführte Modell kann als Generalisierung des Models mit den Annahmen zur Stationarität im weiteren Sinne und unkorreliertem Streuverhalten gesehen werden.

Da die Berechnungen der Wahrscheinlichkeitsdichtefunktionen sehr zeitaufwändig sind, wird in der Folge die Verwendung eines anderen Koordinatensystems untersucht. Wir zeigen, dass eine Verkürzung der Rechenzeit durch die Benutzung eines rotationsellipsoiden Koordinatensystems verringert werden kann. Zusätzlich können andere wichtige Kanalparameter wie die mittlere Dopplerfrequenz sowie die Varianz der Dopplerfrequenz hergeleitet werden.

Das hier vorgestellte theoretische Kanalmodell wird mit Hilfe von Messdaten, die sowohl für den Fahrzeug-Fahrzeug- als auch den Flugzeug-Flugzeug-Kanal aufgenommen wurden, validiert. In beiden Fällen ergibt sich eine sehr gute Übereinstimmung zwischen Messdaten und Kanalmodell. Das Modell passt außerdem zu Messdaten, die von anderen Institutionen für unterschiedlichen Szenarien aufgenommen wurden. Diese Flexibilität zeigt, dass unser Modell sehr generell gehalten ist und daher auf eine Vielzahl an Szenarien angewendet werden kann.

Abstract

The aim of this thesis is to introduce a non-stationary model for the scattering in mobile-to-mobile channels. Due to the evolution of wireless technology, fixed-to-mobile communications systems are nowadays complemented by mobile-to-mobile communications systems.

In the vehicular sector, mobile-to-mobile communications systems are used to enable intelligent transportation systems. Such systems aim to make transportation safer and more efficient by distributing sensor information among the cars. In the aeronautical sector, mobile-to-mobile communications systems will be used, for example, to exchange position, altitude, speed, and heading data between aircraft during flight thus allowing a reduced separation between them. Hence, these systems are necessary to further increase the air traffic density.

Stochastic channel models for the fixed-to-mobile channel are based on the assumption that the channel is wide-sense stationary and exhibits uncorrelated scattering behavior both in a stochastic sense. It has been shown that many mobile-to-mobile channels do not adhere to such assumptions, especially vehicle-to-vehicle and air-to-air channels. The need for new models is therefore due to the fact that mobile-to-mobile channels are fundamentally different from fixed-to-mobile channels.

To overcome the limitations of current channel models, two measurement campaigns to characterize both the vehicle-to-vehicle and the air-to-air channel as exemplary mobile-to-mobile channels were conducted. The measurements confirm the non-stationary behavior of those channels and subsequently, a theoretical model is created on the basis of the measurement data. The employed model is a geometry-based stochastic channel model, which means it consists of two parts. In the geometric part, new expressions for channel parameters, such as delay and Doppler frequency, are derived. In the stochastic part, those expressions enable us to determine closed-form solutions for the required time-variant probability density functions. The presented model can be seen as a generalization of the wide-sense stationary, uncorrelated scattering models.

Since the calculations of the probability density functions are time consuming, the application of a different coordinate system is investigated and we show that computational gains are achieved by using prolate spheroidal coordinates. Additionally, other important channel parameters, such as mean Doppler and Doppler spread, are derived.

The presented theoretical channel model is validated by the measurement data that has been recorded for both the vehicle-to-vehicle and the air-to-air channel. In each case, there is a remarkable agreement between measurement data and the channel model. The model also matches with measurement data recorded by other institutions that used different scenarios. This versatility allows the model to be very general and it can be applied to a wide range of scenarios.

Contents

Chapter 1

Introduction

In the 1860s, Scottish physicist James Clerk Maxwell predicted the existence of electromagnetic waves. Maxwell's equations were the beginning of the wireless communications age. However, it took more than twenty years to experimentally prove that the predictions of the electromagnetic theory were right. Heinrich Hertz, a German physicist, succeeded in 1886 to transfer electromagnetic waves from a transmitter (TX) to a receiver (RX) and thus confirmed Maxwell's theory. Guglielmo Marconi then extended the work of Hertz to achieve long-distance communications. Marconi started at a young age sending wireless messages across his father's garden. After immigrating to England, Marconi continued to increase the distance of the wireless telegraphy. The biggest success was the first transatlantic wireless transmission. He built a transmitter station in Poldhu, Cornwall, UK, and a receiver station on what is today known as Signal Hill in St. John's, Newfoundland, Canada. He reportedly received the first message, the Morse code letter S, on 12th December 1901, which started the inexorable usage of wireless communications systems.

One of the early application fields of wireless communications was the transmission of messages between oceangoing vessels, especially in case of emergency. Since the wired telegraphy already connected Europe and America since 1858, transmissions to and from ships seemed to be a very useful application of the new wireless technology. Interestingly, wireless technology has been used from the beginning for the purpose of mobile-to-mobile (M2M) communications, as transmitter and receiver are mobile and not connected via cable. One of the most famous examples of early M2M communications is the use of the new technology during the sinking of the Titanic.In this example, M2M communications was used to notify the HMS Carpathia about the accident allowing the HMS Carpathia to change course saving many passengers from the freezing cold water. Thus, the usefulness of M2M communications became clear.

Due to the size of the equipment, ship-to-ship communications remained the only civil M2M application for a long time. In the 1920s, radio stations began using the wireless technology for radio broadcast, i.e., fixed-to-mobile (F2M) communications. The difference between F2M and M2M communications is that only the receiver moves while the transmitter is located at a fixed position. F2M communications became the dominant form of wireless communications for the next decades. Television broadcast was introduced at the end of the 1920s. The next important wireless development was the cellular phone system. The first hand-held phone was presented by Motorola in 1973, and in 1983 the first commercial cell phone became available. In the cellular phone system, transmitter and receiver can be mobile, but both transmitter and receiver are connected via a base station. Therefore, the cellular phone system is another example of F2M communications.

Except for military applications, M2M communications became negligible compared to F2M communications due to the size of the transmit equipment. Only in the last couple of years M2M communications systems have been deployed again due to the miniaturization of the electronic components. The new emerging communications systems, e.g., IEEE 802.22, IEEE 802.11p, and IEEE 802.16 allow two mobile users to be directly connected without the need of a base station. The mobility and direct connectivity opens up a broad new field of applications, especially in the vehicular and aeronautical sectors.

The M2M communications systems may be used in the future to connect two aircraft while being airborne to establish a mobile ad-hoc network in order to exchange flight critical data [WFS10]. An even bigger area of operations foreseen to change is in cars. In the vehicular sector, the applications of M2M communications systems are mentioned in the context of intelligent transportation systems (ITSs), which comprise even more than the pure communications systems. Cars are foreseen to exchange sensor data about traffic, weather conditions, movement parameters, etc. to increase the safety and efficiency of automobile transportation. Furthermore, swarms of unmanned vehicles, like unmanned underwater vehicles (UUVs) or unmanned aerial vehicles (UAVs) use M2M communications to coordinate their movements in an unknown environment [LLZ+08]. M2M communications is also a very promising technology for military communications especially on the battlefield, where mobile units need to be coordinated by means of communications systems [SN11].

In order to properly design efficient M2M communications systems, the propagation conditions have to be investigated and modeled. The signal propagation mechanisms between transmit antenna and receive antenna, e.g., attenuation, sig-

nal shadowing or multipath effects are modeled by the wireless channel: The channel describes the electromagnetic environment for the communications signal on its way from transmitter to receiver.

Accurate channel models have always been very important for the design and testing of new communications systems. This is due to the fact that communications systems are usually tested by numerical simulations, and a channel model is needed to accurately represent the impact of the propagation effects onto the system. With such models, the capacity, bit error rate, quality of service, etc, can be assessed even before the actual system is built. If the channel model is accurate, the performance of the simulated communications system comes very close to the real communications system. For F2M channels like the ones occurring in cellular phone systems, there exist numerous different channel models that are in good agreement with measurement data. The channel models at the beginning of cellular telephony age in the 1980s and 1990s relied heavily on a stochastic description of the channel. Those channel models are based on the assumption that the channel is stationary for a certain time.

However, M2M channels are *fundamentally* different from F2M channels. Since both transmitter and receiver move at high velocities in the vehicular and aeronautical case, the channel becomes non-stationary. Therefore, the F2M channel models can only be used for particular M2M scenarios, where the geometry remains constant, and needs to be extended. Due to the channel being non-stationary, propagation conditions can vary rapidly. Non-stationary channel models are needed for the description of a rapidly changing environment.

In this thesis, a new channel model for M2M communications is presented. The model is based on a geometric-stochastic approach that includes non-stationarity and time-variance. The probability density functions (pdfs) for delay and Doppler frequency are derived. Hereby, the mathematical description corresponds to the geometry of the scenario. The proposed channel model is used to simulate the time-variant scattering effects in M2M channels. The geometry of the scenarios becomes important when simplifications for the model are implemented. As the model is theoretical in nature, the model is validated with measurement data for the vehicle-to-vehicle (V2V) and air-to-air (A2A) channel.

The thesis is structured as follows:
In Chapter 2, we provide an extensive overview of three different channel modeling techniques: stochastic channel modeling, geometric channel modeling, and geometric-stochastic channel modeling. The most important results of stochastic channel models are summarized and its shortcomings for the M2M channel mold-

ing are explained. The main drawback for purely stochastic models is the wide-sense stationary uncorrelated scattering (WSSUS) assumption. It is shown, how the WSSUS models can be generalized to incorporate non-WSSUS models. Purely geometric models include the non-stationarity, but the analytical analysis of these models can be cumbersome for calculations if the propagation environment is difficult. A combination of stochastic and geometric channel modeling techniques merges the advantages of both. Applications for such modeling techniques are found in V2V and A2A channel models, for which we do a literature survey.

In order to model these two M2M channels adequately, we conducted two measurement campaigns for both the V2V and the A2A channel. The details of the measurement campaigns are described in Chapter 3. The channel sounding equipment and measurement parameters are illustrated as well. For the vehicular measurement campaign, we provide information about the measurement vehicles, vehicular antennas, and routes. For the aeronautical campaign, the measurement aircraft, aircraft antennas, and flight profiles are described. The data collected in these campaigns is later used to validate the theoretical models.

In Chapter 4, a new V2V channel model for road-side scattering is presented. A theoretical two-dimensional geometric-stochastic channel model (GSCM) is introduced and the choice for this particular model is explained both in the geometric and stochastic part. To validate the model, we compare the theoretic results with the data obtained from the V2V measurement campaign. The comparison reveals a very good agreement between the theoretical channel model and the measured channel. Since the calculations of the probability density functions of the channel are only feasible numerically, two additional ways of describing them are proposed. In the prolate spheroidal coordinate system it is possible to obtain rational solutions for the probability density functions. Furthermore, stochastic descriptions of the channel like the characteristic function, the mean Doppler and the Doppler spread can be calculated. The second approach uses means from algebraic geometry to parameterize the trigonometric functions in order to obtain polynomial solutions.

The V2V channel model is extended in Chapter 5 towards a three-dimensional A2A channel model. By increasing the dimension of the Euclidean space, the same mathematical methods can be applied for the aeronautical channel. Principally, increasing the dimension means using three-dimensional geometric objects instead of two-dimensional ones. Similar to the previous chapter, a theoretical channel model for the joint delay Doppler frequency pdfs are derived. The obtained channel model is compared to the measured A2A channel. Moreover, similarities and differences to the V2V channel are explained.

Chapter 6 summarizes the contributions of the thesis focusing on the new geometric-stochastic modeling techniques together with the problems that were solved by those contributions. An outlook addresses the open question and challenges of future research.

Chapter 2

Introduction to Channel Modeling

2.1 Overview

In this chapter we provide an overview over the propagation mechanisms and the different components of the wireless channel. Subsequently, various channel modeling techniques together with its advantages and disadvantages are introduced. At the end, we present a review of existing channel models for V2V and A2A communications.

2.1.1 Propagation Mechanisms

In the theory of communications, the channel describes the physical propagation medium between transmitter and receiver. On its way from transmitter to receiver the signal, which conveys the information, is modified by the channel. Depending on the channel these modifications can be very different.

The channel is called wireless, when there is no connection via cable between transmitter and receiver. An example for a wireless channel in mobile communications is the link between the base station and the cellular phone. The receiver has to deal with multiple copies of the transmit signal due to multipath propagation and with the Doppler effect due to the mobility of the participants [BD91]. There are three propagation mechanisms that cause multipath, namely

- reflection,
- scattering, and
- diffraction.

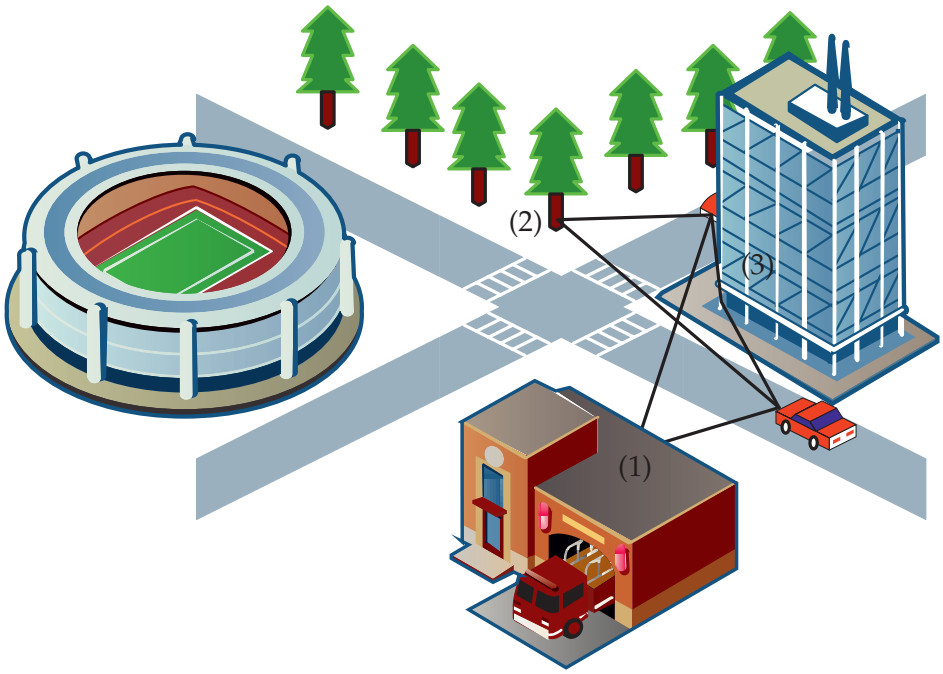

Figure 2.1. *(1) Reflection at the fire department's wall, (2) scattering at the tree trunks, and (3) diffraction at the edge of the office building for an exemplary V2V communications scenario.*

A reflection occurs on smooth surfaces. For this particular propagation mechanism the incident angle always equals the reflection angle. The law that governs these relations is called Snell's law . The strength of the reflected signal depends on the reflection coefficient ρ_{v}, which in turn depends on the electric properties of the surface [Par00].

If the signal bounces off a rough surface, the electromagnetic wave is not only reflected in one single direction, but scattered in all directions. This propagation mechanism is therefore called scattering [BS87]. There are three types of scattering: If objects are small compared to the wavelength, the scattering is called Rayleigh scattering. For objects with the same size in relation to the wavelength, it is called Mie scattering, and for objects that are larger than the wavelength, it is called geometric scattering.

Diffraction is the term for the third propagation mechanism. It describes the bending of waves around edges or openings. The wavelength must be in the order of the object, so that the propagation mechanism occurs.

For all three propagation mechanisms a signal might be received, even when the geometrical line-of-sight (LOS) is blocked or shadowed, cf. Fig. 2.1. In the thesis we focus on the second propagation mechanism, i.e., geometric scattering and its effects on the received signal.

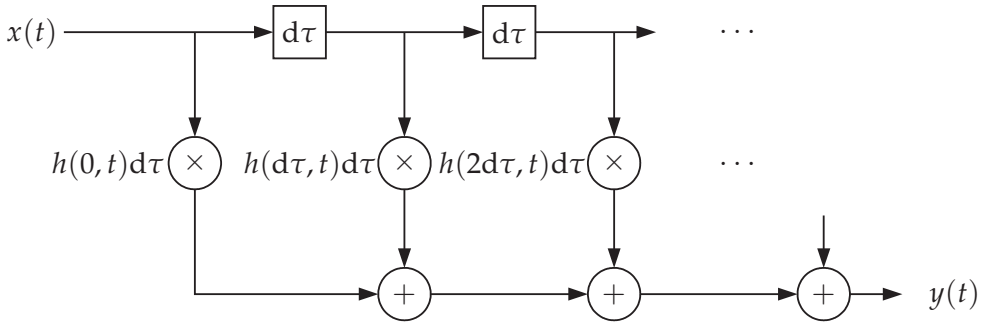

Figure 2.2. *Input delay line structure as realization of input-output relation [Höh11].*

2.1.2 Wireless Channel Components

In order to model the M2M channel appropriately, the channel model introduced by Bello in [Bel73] is presented in the following. Bello proposed the so called surface scatter channel. The transmitted signal $x(t)$ becomes the received signal $y(t)$ after being modified by the time-variant weight function[1] $h(\tau, t)$. The input-output relation is mathematically represented as

$$y(t) = \int_{\infty}^{\infty} x(t-\tau)h(\tau,t)\,\mathrm{d}\tau + n(t)\,, \tag{2.1}$$

with $n(t)$ being the additive white Gaussian noise (AWGN). Hereby, the variable t describes the absolute time and the variable τ represents the delay induced by the propagation. A model of the input-output relation is shown in Fig. 2.2. The time-variant weight function $h(\tau, t)$ of the surface scatter channel consists of three different components and thus becomes

$$h(\tau,t) = h_{\mathrm{dir}}(\tau,t) + h_{\mathrm{ref}}(\tau,t) + h_{\mathrm{sc}}(\tau,t)\,, \tag{2.2}$$

where h_{dir}, h_{ref}, and h_{sc} represent the direct or LOS component, the reflected components, and the scattered components, respectively. The direct component is influenced by the free-space attenuation, the phase shift due to the propagation path length, and the antenna patterns G_{t} and G_{r}. The direct component can be represented as

$$h_{\mathrm{dir}}(\tau_{\mathrm{dir}},t) = A_{\mathrm{dir}}(t)\delta(t-\tau_{\mathrm{dir}}(t))\exp(-\mathrm{j}2\pi f_{\mathrm{c}}\tau_{\mathrm{dir}}(t))\,, \tag{2.3}$$

where $A_{\mathrm{dir}}(t)$ is the product of the free space attenuation and the antenna gains, $\delta(t)$ the Dirac delta distribution, f_{c} the carrier frequency, and $\tau_{\mathrm{dir}}(t)$ the propagation

[1] The time-variant weight function is also often denoted as time-variant impulse response in the literature.

delay. The total attenuation between transmitter and receiver is given by the Friis formula

$$A_{\mathrm{dir}}(t) = \left(\frac{1}{4\pi\tau_{\mathrm{dir}}(t)f_{\mathrm{c}}}\right)\sqrt{G_{\mathrm{t}}\left(\varphi_{\mathrm{t}}(t),\theta_{\mathrm{t}}(t)\right)G_{\mathrm{r}}\left(\varphi_{\mathrm{r}}(t),\theta_{\mathrm{r}}(t)\right)}\,, \tag{2.4}$$

where $\varphi_{\mathrm{t}}(t)$ and $\theta_{\mathrm{t}}(t)$ are the time-variant angles of departure and $\varphi_{\mathrm{r}}(t)$ and $\theta_{\mathrm{r}}(t)$ the time-variant angles of arrival. The amplitude of the direct component is therefore proportional to the inverse of the delay due to the distribution of the power for a spherical wave. The delay $\tau_{\mathrm{dir}}(t)$ in the complex exponential function in (2.3) introduces a time-variant phase shift and thus a Doppler frequency shift at the receiver is observed. The Doppler frequency shift can be calculated using the geometric information of the two mobile entities. The amplitude of the direct component can be composed of multiple copies of the signal with similar delays $\tau_{\mathrm{dir}}(t)$ for a finite measurement bandwidth. This is, however, an effect caused by the limited bandwidth of the RX and is not a property of the channel itself. If fading influences the amplitude of the LOS component due to receiving multiple copies of the signal with the same delay, the distribution of the amplitude is often modeled as a Rice process, which characterizes the small scale fading [TAG03].

The second component in (2.2) describes the weight function caused by the specular reflections. The mathematical description of $h_{\mathrm{ref}}(\tau_{\mathrm{ref}},t)$ is similar to the description of the direct component. The reflection coefficient $\rho_{\mathrm{v}}(t)$ for vertically polarized waves induces extra loss and phase shift due to the reflection of the electromagnetic wave on a smooth surface. The description for the reflected component in the channel becomes

$$h_{\mathrm{ref}}(\tau_{\mathrm{ref}},t) = \sum_{i=1}^{N_{\mathrm{ref}}} \rho_{\mathrm{v},i}(t)A_{\mathrm{ref},i}(t)\delta(t-\tau_{\mathrm{ref},i}(t))\exp(-\mathrm{j}2\pi f_{\mathrm{c}}\tau_{\mathrm{ref},i}(t))\,. \tag{2.5}$$

The differences between $h_{\mathrm{dir}}(\tau_{\mathrm{dir}},t)$ and $h_{\mathrm{ref}}(\tau_{\mathrm{ref}},t)$ are the higher attenuation due to the reflection, the longer delay $\tau_{\mathrm{ref}}(t)$, and the different Doppler frequency $\nu(t) = -f_{\mathrm{c}}\dot{\tau}_{\mathrm{ref}}(t)$. For the measured A2A channel the amplitude of the specular reflection (SR) component can realistically be modeled, e.g., as Nakagami process [Nak60]. For the measured V2V channel the path length difference between direct and SR components from the ground can be so small that they end up with the same delay due to the measurement bandwidth. In this case, the amplitudes of the direct component and the SR components in the same tap are modeled by a Ricean distribution.

The third component of the channel is composed of the contributions caused by the signal that is scattered at different objects. Such an object is subsequently designated as scatterer. Therefore, in contrast to $h_{\mathrm{dir}}(\tau_{\mathrm{dir}},t)$ and similar to $h_{\mathrm{ref}}(\tau_{\mathrm{ref}},t)$,

$h_{\mathrm{sc}}(\tau_{\mathrm{sc}}, t)$ can consist of more than one component. The mathematical description of $h_{\mathrm{sc}}(\tau_{\mathrm{sc}}, t)$ is given by

$$h_{\mathrm{sc}}(\tau_{\mathrm{sc}}, t) = \sum_{i=1}^{N_{\mathrm{sc}}} \gamma_{\mathrm{v},i}(t)\delta(t - \tau_{\mathrm{sc},i}(t)) \exp(-\mathrm{j}2\pi f_{\mathrm{c}} \tau_{\mathrm{sc},i}(t)) \,, \tag{2.6}$$

where N_{sc} is the number of scatterers. Each contribution from a scatterer obtains its own attenuation factor γ_{v} for vertical polarization and delay τ_{sc}. The power of the contributions that are received from the scattered signals can be above the noise power of the AWGN. The distribution of the received power from the scattering possesses a distinctive shape in the delay Doppler domain, which depends on the geometry of the scenario. The influence of the geometric scenario on the distribution of the Doppler frequency is derived later in the thesis.

The last component that we consider is the additive white Gaussian noise term $n(t)$, which is usually used to describe stochastic effects in the receiver. Its noise spectral density is assumed to be white, i.e., $\Phi_{nn}(f) = N_0/2$ [Pro00]. This leads to an infinite power of the noise process, if the power spectral density is integrated over all frequencies. Although this assumption is physically not realistic, it is a well used model due to its mathematical tractability.

2.2 Channel Modeling Techniques

The modeling of wireless communications channels can be achieved in many different ways. The different techniques to model a communications channel may be, according to [ABB+07], split into three categories: deterministic modeling, stochastic modeling, and geometry-based stochastic modeling.

In the beginning of digital communications, mostly narrow-band channel models were used. This is due to the fact that the measurement equipment could only process narrow-band data at that time. When evaluating the data, the multipath components could not be resolved. Therefore, the amplitude of the signal was modeled according to the fading that occurred in the measurements. Since the fading seemed to occur in a random manner, stochastic methods were applied to describe the channel and the modeled amplitudes were fit to the amplitudes in the measurement data.

Another channel modeling technique attempts to trace every single ray from transmitter to the receiver, which is called ray tracing. This modeling technique is very exact, since for a specific propagation environment all the propagation mechanisms are considered. For the calculation of the channel the Maxwell equations,

which are partial differential equations, have to be solved. If, however, the channel is composed of a myriad of components that reflect, scatter of diffract the signal, the method becomes prohibitive due to the complexity of the calculations.

Taking the geometry of a scenario into account, but still using stochastic means to characterize the channel combines the advantages of both stochastic and geometric channel modeling. This channel modeling technique is called geometric-stochastic channel modeling. Such a technique is necessary to model M2M channels, since they incorporate non-stationary effects. Additionally, the large bandwidth of the measurement systems nowadays make it possible to resolve multipath effects. Therefore, a wide-band model is required, which the GSCM can provide.

2.3 Stochastic Channel Modeling

Stochastic channel models were used from the beginning of channel modeling to provide a suitable description of the channel. By using the stochastic theory it was possible to describe a wide range of different scenarios [Cla68].

The seminal work of stochastic channel modeling was published by Bello [Bel63] in the 1960s. In his paper he used four kernel functions or input-output functions. In total he described twelve different channel functions. Nowadays only four of this original functions are still used to describe the channel [Pät02]:

- time-variant weight function

  $$h(\tau, t) \tag{2.7}$$

  The time-variant weight function $h(\tau, t)$ describes the time-variant dispersion of the channel. Discrete components of the channel can be tracked over time t with this representation. A model of the influence of the time-variant weight function on a transmit signal, realized as a filter structure, is shown in Fig. 2.2.

- spreading function

  $$s(\tau, \nu) = \int_{-\infty}^{\infty} h(\tau, t) \exp\left(-\mathrm{j}2\pi\nu t\right) \, \mathrm{d}t \tag{2.8}$$

  The spreading function $s(\tau, \nu)$ describes the dispersion in delay and Doppler frequency of the channel. Since the delay and Doppler frequency are physically bounded, it is according to [Gli08] suitable to use the spreading function to describe the channel.

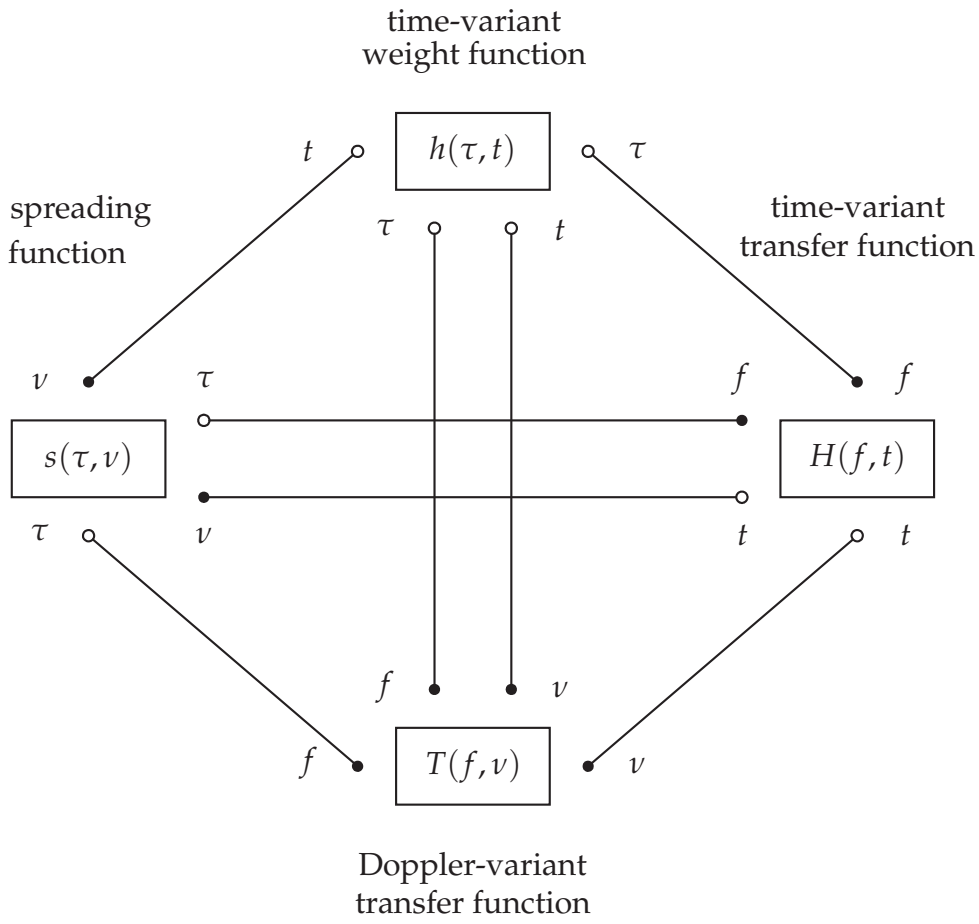

Figure 2.3. *System functions of the WSSUS channel [Pät02].*

- time-variant transfer function

$$H(f,t) = \int_{-\infty}^{\infty} h(\tau,t) \exp\left(-\mathrm{j}2\pi f\tau\right) \mathrm{d}\tau \tag{2.9}$$

  The time-variant transfer function $H(f,t)$ describes the time-variant fading effects of the multipath components of the channel in the frequency domain.

- Doppler-variant transfer function

$$T(f,\nu) = \int_{-\infty}^{\infty}\int_{-\infty}^{\infty} h(\tau,t) \exp\left(-\mathrm{j}2\pi\left(\nu t + f\tau\right)\right) \mathrm{d}t\,\mathrm{d}\tau \tag{2.10}$$

  The Doppler-variant transfer function $T(f,\nu)$ is the double Fourier transform of the time-variant weight function, where the time-variance is shown in both frequency domains.

These functions completely describe the behavior of the channel in time and/or frequency domain.

More important concerning the stochastic modeling are the correlation functions of the channel. They describe the stochastic relation between two system functions for different time and/or frequency. In general, these correlation functions are four-dimensional functions. The four stochastic system functions are given by correlating the system function of the respective channel system functions [Pät02]:

- $r_{\mathrm{hh}}(\tau_1, \tau_2, t_1, t_2) = \mathbb{E}\{h(\tau_1, t_1)h^*(\tau_2, t_2)\}$, (2.11)
- $r_{\mathrm{ss}}(\tau_1, \tau_2, \nu_1, \nu_2) = \mathbb{E}\{s(\tau_1, \nu_1)s^*(\tau_2, \nu_2)\}$, (2.12)
- $r_{\mathrm{HH}}(f_1, f_2, t_1, t_2) = \mathbb{E}\{H(f_1, t_1)H^*(f_2, t_2)\}$, (2.13)
- $r_{\mathrm{TT}}(f_1, f_2, \nu_1, \nu_2) = \mathbb{E}\{T(f_1, \nu_1)T^*(f_2, \nu_2)\}$, (2.14)

with $(\cdot)^*$ being the complex conjugate and $\mathbb{E}\{\cdot\}$ the expectation operator. The correlation functions can be simplified, if stationarity and uncorrelated scattering are assumed.

2.3.1 Wide Sense Stationarity (WSS)

A simplification of the correlation functions arises, if the channel is thought to be wide-sense stationary in time direction t. This simplification is only valid, if the mobile transmitter and/or receiver moves a short distance during the description of the channel. WSS means that the first and second moment do not depend on the absolute time t, but only on the time difference Δt. The delay-Doppler auto-correlation function becomes

$$r_{\mathrm{ss}}(\tau_1, \tau_2, \nu_1, \nu_2) = S_{\mathrm{ss}}(\tau_1, \tau_2, \nu_1)\delta(\nu_2 - \nu_1)\,. \tag{2.15}$$

This relation means that scattering is uncorrelated for different Doppler frequencies ν. The correlation function r_{ss} will behave like non-stationary white noise in the Doppler shift variable ν [Bel63].

2.3.2 Uncorrelated Scattering (US)

Uncorrelated scattering means that two scatterers with different delays are stochastically uncorrelated. The delay-Doppler auto-correlation function is therefore described by

$$r_{\mathrm{ss}}(\tau_1, \tau_2, \nu_1, \nu_2) = S_{\mathrm{ss}}(\tau_1, \nu_1, \nu_2)\delta(\tau_2 - \tau_1)\,. \tag{2.16}$$

As for the stationarity in time, this relation leads to a non-stationary white noise process for the delay variable τ.

2.3.3 WSSUS Model

Bello combined in [Bel63] the presented simplifications in (2.15) and (2.16) resulting in the WSSUS model. The delay-Doppler auto-correlation function becomes

$$r_{\mathrm{ss}}(\tau_1, \tau_2, \nu_1, \nu_2) = S_{\mathrm{ss}}(\tau_1, \nu_1)\delta(\tau_2 - \tau_1)\delta(\nu_2 - \nu_1)\,. \tag{2.17}$$

where $S_{\mathrm{ss}}(\tau_1, \nu_1) = S_{\mathrm{ss}}(\tau, \nu)$ is called the scattering function and only depends on two instead of the four variables in r_{ss} as in (2.12). Thus, r_{ss} behaves like a non-stationary white noise process with respect to the delay τ and the Doppler frequency ν and the time-frequency auto-correlation function r_{HH} is wide-sense stationary with regard to the frequency f and the time t.

The scattering function has been used in many channel models, e.g., in [Fai89] to describe the channel for the respective communications system. In the WSSUS case Schulze and Höher showed in [Sch89, Hoe92] that the scattering function $S_{\mathrm{ss}}(\tau, \nu)$ is proportional to the joint pdf $p(\tau, \nu) = p(\tau)p(\nu|\tau)$ with $p(\nu|\tau)$ being the conditional probability density function. The proportionality is given by

$$S_{\mathrm{ss}}(\tau, \nu) \propto p(\tau, \nu)\,. \tag{2.18}$$

Thus, the probability density function represents, except for a constant factor, the average power received at a certain delay and Doppler frequency. This is a central result in the WSSUS theory and makes it possible to interchange the pdf and the Doppler power spectrum (DPS). In the thesis, we extend this crucial relationship to the non-WSSUS case and explain, why an approximate proportionality in such circumstances can be assumed in Chapter 4.

For the DPS, which is the integral of $S_{\mathrm{ss}}(\tau, \nu)$ over the delay, there exists already a number of pdfs, which are in use nowadays. The Doppler power spectral density is defined as

$$P_\nu(\nu) = \int_{-\infty}^{\infty} S_{\mathrm{ss}}(\tau, \nu)\,\mathrm{d}\tau\,. \tag{2.19}$$

Note that the DPS is proportional to the Doppler pdf $P_\nu(\nu) \propto p(\nu)$. A graphical representation of the relationships between correlation functions and power spectral densities for the WSSUS case can be found in Appendix A.

2.3.4 Doppler Probability Density Functions

Since the Doppler pdfs for M2M channels are a key result of this thesis, a short survey over the existing and practically used Doppler pdfs is given. The three most used Doppler pdfs are: the Jakes pdf for isotropic scattering [Cla68, Gan72, Jak94],

the pdf due to non-isotropic scattering, which we call von Mises pdf in the following [AK98, ABK02], and the Gaussian Doppler pdf [Bel73]. The pdfs for isotropic and non-isotropic scattering can be derived by transforming the angular distribution $p(\varphi)$ into the Doppler frequency domain, which we show in the subsequent paragraph. This methodology is later used to derive the time-variant pdfs for M2M channels. The Doppler frequency ν is determined by the angle φ between the scattering object and the direction of movement by

$$\nu = \cos(\varphi) \frac{\|\mathbf{v}\|}{c} f_c \,, \tag{2.20}$$

with $\|\mathbf{v}\|$ being the magnitude of the velocity vector and c the speed of light. The Doppler spectrum can then be calculated by the following transformation [Pät02]

$$p(\nu) = \sum_{\varphi' \in \left\{\mathcal{F}^{-1}(\nu)\right\}} \frac{p(\varphi')}{\left|\frac{\mathrm{d}\nu}{\mathrm{d}\varphi'}\right|} = \sum_{\varphi' \in \left\{\mathcal{F}^{-1}(\nu)\right\}} p(\varphi') \left|\frac{\mathrm{d}\varphi'}{\mathrm{d}\nu}\right| \,, \tag{2.21}$$

where $\mathcal{F} : \varphi \mapsto \nu(\varphi)$ is a many-to-one mapping and $\mathcal{F}^{-1}$ is the inverse relation $\nu(\varphi) \mapsto \varphi$. The Jacobi determinant is defined as

$$\left|\frac{\mathrm{d}\,\varphi}{\mathrm{d}\,\nu}\right| = \left|\frac{\mathrm{d}}{\mathrm{d}\,\nu} \arccos\left(\frac{\nu}{f_{\mathrm{d,max}}}\right)\right| = \frac{1}{f_{\mathrm{d,max}} \sqrt{1 - \left(\frac{\nu}{f_{\mathrm{d,max}}}\right)^2}} \,, \tag{2.22}$$

and the maximum Doppler frequency is given by $f_{\mathrm{d,max}} = \|\mathbf{v}\| f_c / c$.

Jakes Doppler PDF

For isotropic scattering an angular probability density of $p(\varphi) = 1/(2\pi)$ is assumed. Therefore, the Jakes spectrum, which was originally derived by Clarke, becomes

$$p(\nu) = \frac{1}{\pi \sqrt{1 - \left(\frac{\nu}{f_{\mathrm{d,max}}}\right)^2}} \,, \quad |\nu| \leq f_{\mathrm{d,max}} \,. \tag{2.23}$$

The Jakes spectrum as shown in Fig. 2.4 is mainly used for fixed-to-mobile communications, where one can assume that the contribution from the scattering comes equally from all directions. A detailed description of the derivation of the Jakes spectrum can be found in [Zaj12]. The derivation is straightforward due to the fact that the angular pdf $p(\varphi)$ is constant and does not depend on the angle φ.

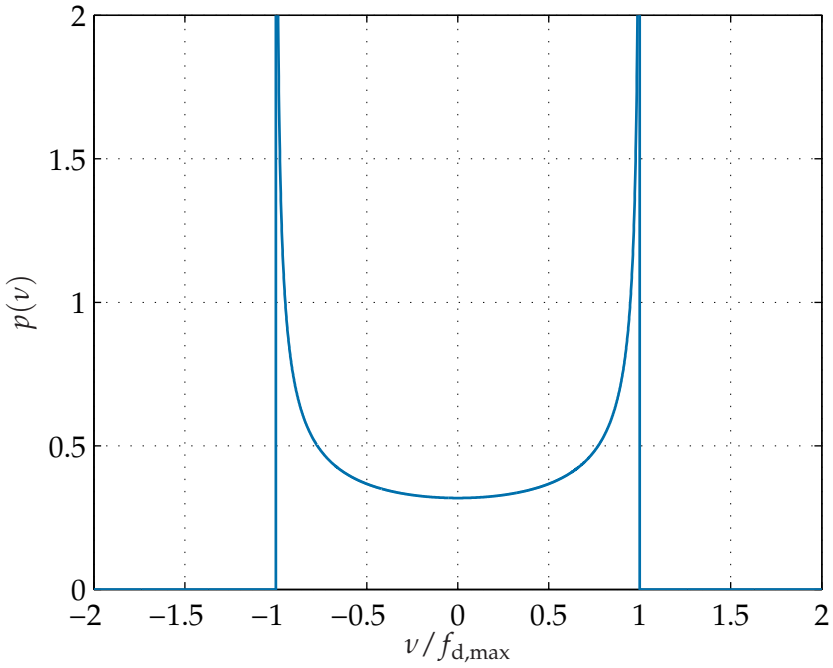

Figure 2.4. *Jakes Doppler pdf for normalized Doppler frequency.*

Von Mises Doppler PDF

For the non-isotropic scattering the angular pdf becomes more involved. A pdf often used in directional statistics is called von Mises distribution [vM18] and is also known as circular normal distribution. The pdf shown in Fig. 2.5 is given by

$$p(\varphi|\kappa,\mu) = \frac{1}{2\pi \mathrm{I}_0(\kappa)} \exp\left(\kappa \cos\left(\varphi - \mu\right)\right) . \tag{2.24}$$

where $\mathrm{I}_0(\kappa)$ is the zeroth order modified Bessel function of the first kind. The coefficient κ determines how strongly the distribution is concentrated around the mean angle μ. The Doppler pdf resulting from a von Mises distribution $p(\varphi|\kappa,\mu)$ is obtained by invoking (2.21) on (2.24). We get

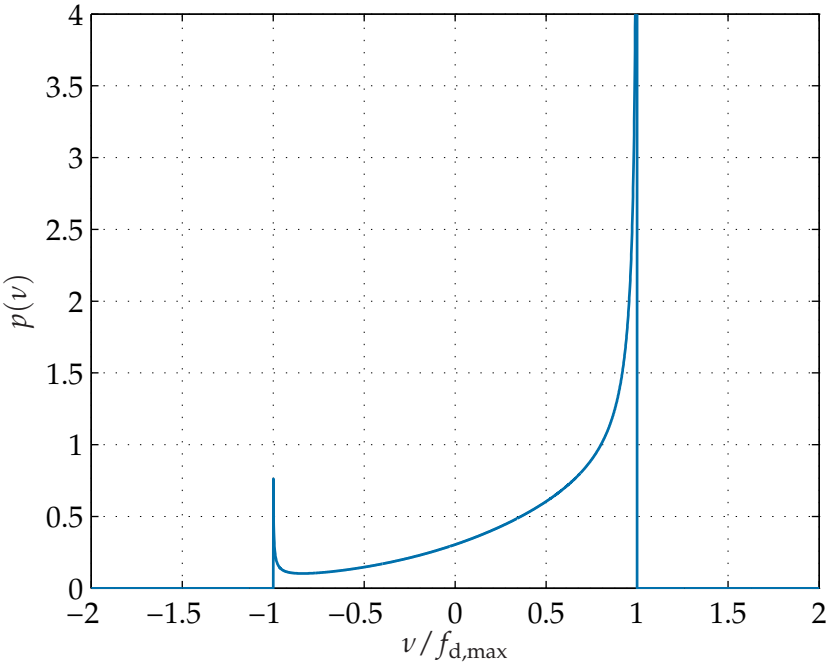

Figure 2.5. *Doppler pdf for non-isotropic scattering with $\kappa = 2$, $\mu = \pi/4$ and normalized Doppler frequency.*

$$
\begin{aligned}
p(\nu|\kappa,\mu) &= \frac{1}{2\pi f_{\mathrm{d,max}} \mathrm{I}_0(\kappa)\sqrt{1-\left(\frac{\nu}{f_{\mathrm{d,max}}}\right)^2}} \left[\exp\left\{\kappa\cos\left(\arccos\left(\frac{\nu}{f_{\mathrm{d,max}}}\right)-\mu\right)\right\}\right. \\
&\left. + \exp\left\{\kappa\cos\left(-\arccos\left(\frac{\nu}{f_{\mathrm{d,max}}}\right)-\mu\right)\right\}\right] \\
&= \frac{1}{2\pi f_{\mathrm{d,max}} \mathrm{I}_0(\kappa)\sqrt{1-\left(\frac{\nu}{f_{\mathrm{d,max}}}\right)^2}} \times \\
&\left[\exp\left\{\kappa\left(\cos(\mu)\frac{\nu}{f_{\mathrm{d,max}}} + \sin(\mu)\sqrt{1-\left(\frac{\nu}{f_{\mathrm{d,max}}}\right)^2}\right)\right\}\right. \\
&\left. + \exp\left\{\kappa\left(\cos(\mu)\frac{\nu}{f_{\mathrm{d,max}}} - \sin(\mu)\sqrt{1-\left(\frac{\nu}{f_{\mathrm{d,max}}}\right)^2}\right)\right\}\right] \\
&= \frac{\exp\left\{\kappa\cos(\mu)\frac{\nu}{f_{\mathrm{d,max}}}\right\}}{\mathrm{I}_0(\kappa)} \frac{\cosh\left(\kappa\sin(\mu)\sqrt{1-\left(\frac{\nu}{f_{\mathrm{d,max}}}\right)^2}\right)}{\pi f_{\mathrm{d,max}}\sqrt{1-\left(\frac{\nu}{f_{\mathrm{d,max}}}\right)^2}}.
\end{aligned}
\tag{2.25}
$$

This is a similar result as in [ABK02], but there the Doppler pdf is derived by a Fourier transformation of the normalized correlation function, i.e., the characteristic function.

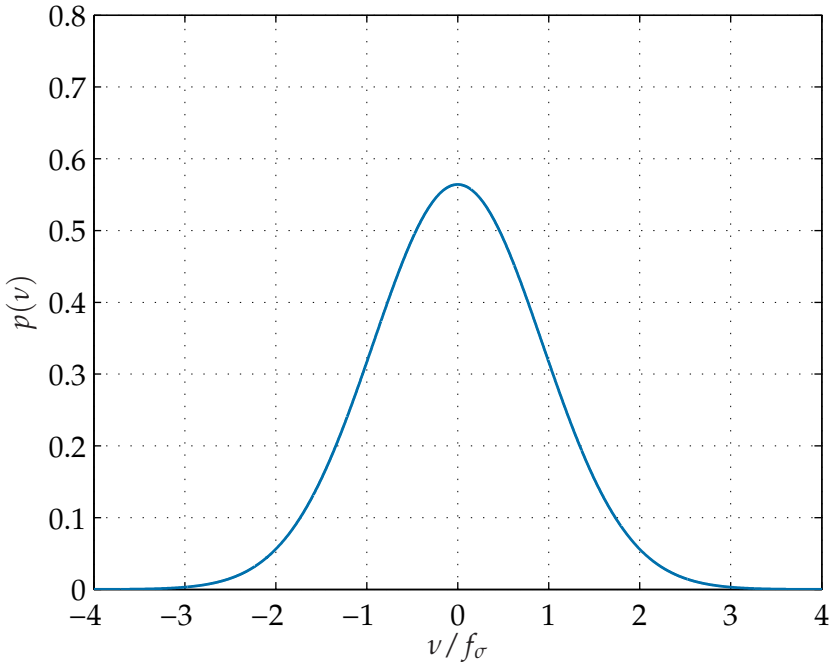

Figure 2.6. *Gaussian Doppler pdf with* $f_\sigma = \sqrt{\ln(2)}$ *,*Hz *and normalized Doppler frequency.*

Gaussian Doppler PDF

The Gaussian Doppler pdf is mainly used in aeronautical channel models [Bel73] and cannot be derived as straightforwardly as the previous two pdfs. In aeronautical channels the Doppler frequency according to Bello possesses a strong directivity and decays exponentially. The pdf of the Doppler frequency is shown in Fig. 2.6 and is given by

$$p(\nu) = \sqrt{\frac{\ln(2)}{\pi f_\sigma^2}} \exp\left(-\ln(2)\left(\frac{\nu}{f_\sigma}\right)^2\right), \tag{2.26}$$

with f_σ being the 3 dB cut off frequency. Since infinite Doppler frequencies have still non-zero probability in this case, it can only be seen as approximation of the actual Doppler pdf.

Mean Doppler and Doppler Spread

Important stochastic parameters for the Doppler pdf are the mean Doppler μ and the Doppler spread σ. The mean Doppler describes the mean Doppler frequency shift

of the signal, whereas the Doppler spread describes the square root of the second central moment. The mean Doppler μ is defined as

$$\mu = \frac{\int_{-\infty}^{\infty} \nu P_\nu(\nu)\,\mathrm{d}\nu}{\int_{-\infty}^{\infty} P_\nu(\nu)\,\mathrm{d}\nu} = \int_{-\infty}^{\infty} \nu p(\nu)\,\mathrm{d}\nu\,, \tag{2.27}$$

where $P_\nu(\nu)$ is the DPS and $p(\nu)$ the Doppler pdf. The Doppler spread σ comes to

$$\sigma = \sqrt{\frac{\int_{-\infty}^{\infty} (\nu-\mu)^2 P_\nu(\nu)\,\mathrm{d}\nu}{\int_{-\infty}^{\infty} P_\nu(\nu)\,\mathrm{d}\nu}} = \sqrt{\int_{-\infty}^{\infty} (\nu-\mu)^2 p(\nu)\,\mathrm{d}\nu}\,. \tag{2.28}$$

The normalized auto-correlation function or characteristic function $\Phi(u)$ is the inverse Fourier transform of the normalized DPS or the pdf, respectively. The characteristic function is given by

$$\Phi(u) = \int_{-\infty}^{\infty} p(\nu) \exp\left(\mathrm{j}2\pi\nu u\right)\,\mathrm{d}\nu\,. \tag{2.29}$$

The characteristic function describes the temporal correlation of the stochastic process. With the help of the characteristic function it becomes possible to calculate the mean Doppler and Doppler spread in a different way. The mean Doppler and Doppler spread result in

$$\mu = \frac{\dot{\Phi}(0)}{\mathrm{j}2\pi} \qquad \text{and} \qquad \sigma = \frac{1}{2\pi}\sqrt{\dot{\Phi}(0)^2 - \ddot{\Phi}(0)}\,. \tag{2.30}$$

The characteristic functions of the aforementioned three Doppler pdfs become

$$\Phi(u) = \mathrm{J}_0(2\pi f_{\mathrm{d,max}} u) \tag{2.31}$$

$$\Phi(u) = \frac{\mathrm{I}_0\left(\sqrt{\left(\kappa\cos\left(\mu\right) + \mathrm{j}2\pi f_{\mathrm{d,max}} u\right)^2 + \left(\kappa\sin\left(\mu\right)\right)^2}\right)}{\mathrm{I}_0(\kappa)} \tag{2.32}$$

$$\Phi(u) = \exp\left(-\left(\frac{\pi f_\sigma u}{\sqrt{\ln(2)}}\right)^2\right)\,, \tag{2.33}$$

where $\mathrm{J}_0(\cdot)$ is the zeroth-order Bessel function of the first kind. It can be seen that for $\kappa = \mu = 0$ and $\mathrm{J}_0(2\pi f_{\mathrm{d,max}} u) = \mathrm{I}_0(\mathrm{j}2\pi f_{\mathrm{d,max}} u)$ the characteristic function of the von Mises pdf turns into the characteristic function of the Jakes spectrum.

The mean Doppler and the Doppler spread for Jakes, von-Mises and Gaussian Doppler pdfs are given by [Akk94]

$$\mu = 0\,, \quad \sigma = \frac{f_{\mathrm{d,max}}}{\sqrt{2}} \tag{2.34}$$

$$\mu = f_{\mathrm{d,max}} \cos(\mu) \frac{\mathrm{I}_1(\kappa)}{\mathrm{I}_0(\kappa)}\,,$$

$$\sigma = f_{\mathrm{d,max}} \sqrt{\frac{\mathrm{I}_0(\kappa) + \mathrm{I}_2(\kappa)}{2\mathrm{I}_0(\kappa)} \cos^2(\mu) + \frac{\mathrm{I}_1(\kappa)}{k\mathrm{I}_0(\kappa)} \sin^2(\mu) - \left(\frac{\mathrm{I}_1(\kappa)}{\mathrm{I}_0(\kappa)}\right)^2 \cos^2(\mu)} \tag{2.35}$$

$$\mu = 0\,, \quad \sigma = \frac{f_\sigma}{\sqrt{2\ln(2)}}\,, \tag{2.36}$$

with $\mathrm{I}_n(\cdot)$ being the nth-order modified Bessel function of the first kind. The Doppler pdfs are derived later on for M2M channels, where a *time-variant* pdf is needed. The derived pdfs are the building blocks of the time-variant joint delay Doppler pdfs. For such pdfs the mean Doppler and Doppler spread also become time-variant and the wide-sense stationary assumption is *not* valid anymore.

2.3.5 Theory of Non-Stationary Channels

As mentioned above, the stationarity assumption is used to simplify the description of the correlation functions, but stationarity is hardly a property that occurs in practice: Recent measurements for the V2V channel unveiled that the channel is not stationary anymore [PZB+08, Ber12, BZT+12] due to the high velocities of the mobile participants. Therefore, the two-dimensional correlation functions in (2.17) cannot be used to adequately describe the channel. Additionally, channel parameters like delay spread, correlation bandwidth, and Rician K factor lose their meaning [Bul02] in a non-stationary environment.

A more general approach has to be employed to account for the non-stationarities of the channel. A useful theory of non-stationary processes can be found in the field of time-frequency analysis, e.g., short-time Fourier transform (STFT) or wavelets [MH06]. Matz introduces in [Mat05] the stochastic description for non-WSSUS channels. He generalizes Bello's concept of WSSUS channels and derives time-frequency dependent scattering functions. A problem arises, if the analysis is done in time and frequency for a single time instant. Such a limit on time and frequency resolution is similar to the uncertainty principle in quantum theory discovered by Heisenberg and is called the Gabor limit [Gab46]. Analytically, however, it is possible to define an instantaneous Doppler frequency that is proportional to the derivative of the distance [SK98] and which is computable for every time instance.

A thorough survey on WSSUS and non-WSSUS models can be found in [HM11]. In the following, we introduce the theory of non-stationary channels, show the applicability for M2M channels and show the relation to the work presented in this thesis.

The theory of the stochastic description for non-stationary channels was introduced by Matz in [Mat03a] and [Mat03b]. A more elaborate version can be found in his journal publication [Mat05]. The author presents the local scattering function (LSF) and the channel correlation function (CCF) to characterize the mean power and the correlation of non-WSSUS channels. A different concept called local WSSUS assumption is shown in [OHN+10]. Note that Bello already mentioned quasi-WSSUS channels in [Bel63].

In the case of non-stationary channels a four-dimensional correlation function $r_{\mathrm{hh}}(\tau, t, \Delta\tau, \Delta t)$ is needed to describe the correlation of the channel. The correlation function is given by

$$r_{\mathrm{hh}}(\tau, t, \Delta\tau, \Delta t) = \mathbb{E}\left\{h(\tau + \Delta\tau, t) h^*(\tau, t - \Delta t)\right\} , \tag{2.37}$$

with $\tau = \tau_2$, $\Delta\tau = \tau_1 - \tau_2$, $t = t_1$, and $\Delta t = t_1 - t_2$ and therefore corresponds to (2.11). $r_{\mathrm{hh}}(\tau, t, \Delta\tau, \Delta t)$ describes the correlation between the time-variant weight function at time t and $t + \Delta t$ and at delay τ and $\tau + \Delta\tau$. Since the stochastic processes are non-stationary, the correlation function depends on the time t and the delay τ. For non-stationary channels a power spectrum in the original sense does not exist. But from the theory of time-frequency analysis, time-dependent power spectra can be defined [MF85]. They cannot, however, be defined in a non-ambiguous way.

By adopting the time-frequency theory, Matz defined a time-frequency-dependent scattering function. It can be seen as a Fourier transform over the four-dimensional correlation function in $\Delta\tau$ and Δt. The local scattering function $\mathcal{C}_{\mathrm{H}}(t, f; \tau, \nu)$ is hereby defined as

$$\mathcal{C}_{\mathrm{H}}(t, f; \tau, \nu) = \int_{-\infty}^{\infty} \int_{-\infty}^{\infty} r_{\mathrm{hh}}(\tau, t, \Delta\tau, \Delta t) \exp\left\{-\mathrm{j}2\pi\left(\nu\Delta t + f\Delta\tau\right)\right\} \mathrm{d}\Delta t \, \mathrm{d}\Delta\tau \tag{2.38}$$

and provides a complete second-order stochastic description of the channel. In order to visualize such a function two variables (usually time t and frequency f) have to be fixed. The problem compared to WSSUS channels is that the function can be complex and/or negative. Therefore, $\mathcal{C}_{\mathrm{H}}(t, f; \tau, \nu)$ does not directly correspond to a power spectral density, which is always real and positive.

Matz additionally showed that for doubly-underspread (DU) channels the local scattering function can be interpreted as mean power for the scattering at a certain

time t and frequency f, thus providing a physical meaning for this function. To the author's knowledge, there is no theoretically derived local scattering function for an example scenario. In this thesis, we derive time-variant probability density functions that are proportional to the LSF. The pdfs enable us to theoretically describe the channel and relate them to the measurement data. In a sense, we provide mathematically tractable functions to calculate the average received Doppler power for an arbitrary time t. Since the stochastic functions are time-variant, the mean is thought of as an ensemble mean of the stochastic process and not as a temporal mean as it is the case in WSSUS channels. Therefore, the ergodicity assumption has to be dropped.

As mentioned before, purely stochastic models lack the ability to incorporate the time-variance of the channels. For this reason a geometric component is added so that the time-variance is included into the model. The geometry has direct influence on the stochastic functions and makes them time-variant. After presenting the stochastic simulation model, we shortly describe purely geometric models and then combine geometric and stochastic modeling techniques.

2.3.6 Stochastic Simulation Model

A general simulation model for linear time-variant stochastic channels is presented in the following. The simulation model for WSSUS channels is often implemented by the Ricean sum of sinusoid method [PKLL98, Ric44, Ric45]. The sum of sinusoids method is used to create a Gaussian noise process with the correct Doppler spectrum. The spectral shape of the Gaussian process, however, is normally *time-invariant*. For M2M channels a *time-variant* model is needed for most scenarios.

Frequency selective channel models are obtained by using such a Gaussian process for different delays. Pätzold calls this method deterministic Gaussian uncorrelated scattering (DGUS). A stationary scattering function can be perfectly modeled by this method. The DGUS method is extended in this section in order to account for the time-variance of the Doppler spectrum of M2M channels.

For this reason time-variant coefficients $c(t)$ are used in order to create the Gaussian process like in [TGZ96]. The creation of a non-stationary process is shown in Fig. 2.7. It is a graphical representation of (2.39). The first and second moment of the process $g(t|\tau)$[2] become time-variant, which means that the stochastic process is not stationary and not ergodic.

[2]The Gaussian process $g(t|\tau)$ is dependent on the time t under the condition of the delay τ similar to a conditional pdf $p(\cdot|\cdot)$.

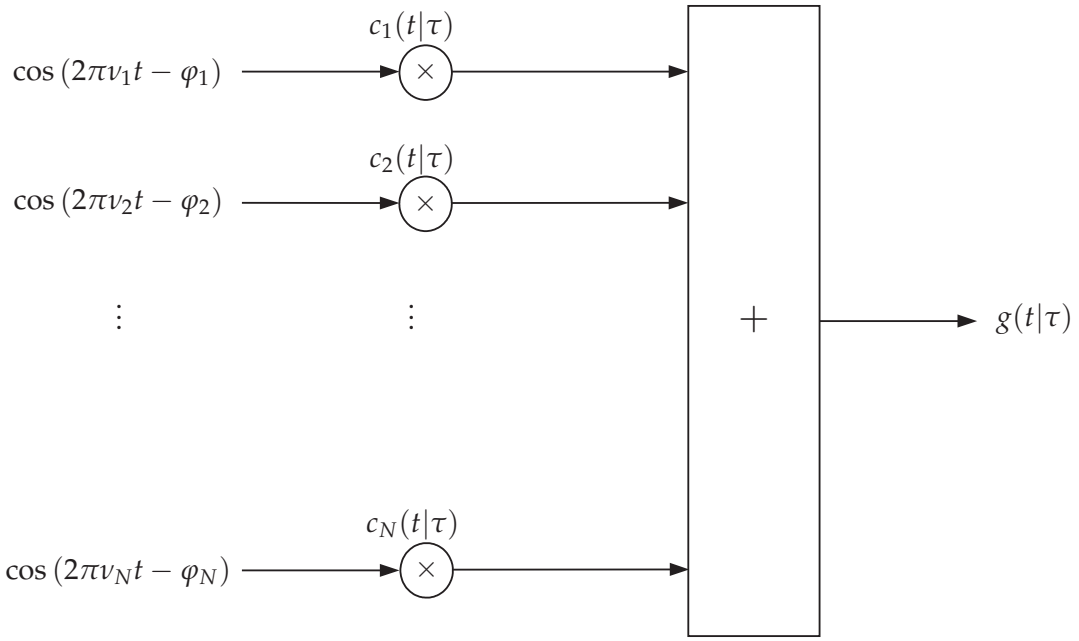

Figure 2.7. *Model for creating a non-stationary colored Gaussian process.*

As mentioned before, scattering of the channel is modeled by a colored Gaussian process for arbitrary delays τ. The time-variant nature of the channel model reflects the change of the geometry by the moving transmitter and receiver. The calculation of the Gaussian process is given by

$$g(t|\tau) = \sum_{n=1}^{N(t)} c_n(t|\tau) \cos(2\pi\nu_n t - \varphi_n) \; . \tag{2.39}$$

In contrast to Rice's sum of sinusoid method, *delay-dependent, time-variant* coefficients $c(t|\tau)$ for creating the Gaussian noise process $g(t|\tau)$ are used. The coefficients are calculated by

$$c_n(t|\tau) = 2\sqrt{\Delta\nu p(t;\nu_n|\tau)} \, , \tag{2.40}$$

with the frequencies ν_n calculated by

$$\nu_n = n\Delta\nu \, . \tag{2.41}$$

Equation (2.40) shows that the coefficients $c_n(t|\tau)$ of the sine waves reflect the distribution of the Doppler frequencies, which is dependent on time t. Therefore, the spectral power of the Gaussian process $g(t|\tau)$ is proportional to the time-variant probability density function $p(t;\nu_n|\tau)$ similar to (2.18).

The scattering channel is simulated by a time-variant tapped delay line model according to Fig. 2.8, where the delays τ_p are arbitrarily spaced. The Gaussian noise

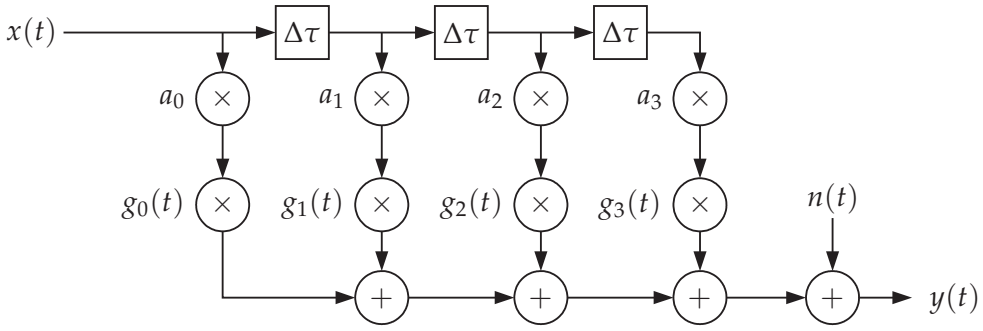

Figure 2.8. *Tapped delay line with time-variant colored Gaussian noise processes $g_p(t)$ [Pät02].*

$g(t|\tau)$ simulating the scattering in the channel is multiplied onto every tap separately. For a discrete model there are only a finite, discrete number of delay taps, i.e. $g(t|\tau) \hat{=} g_p(t)$. The simulated weight function becomes

$$h(\tau, t) = \sum_{p=0}^{P-1} a_p g_p(t) \delta(\tau - \tau_p) \,, \tag{2.42}$$

with p different Gaussian processes for the p delay taps

$$g_p(t) = \sum_{n=1}^{N_p(t)} c_{i,p}(t) \cos\left(2\pi \nu_n t - \varphi_n\right) \,. \tag{2.43}$$

It is assumed that the Gaussian processes $g_p(t)$ are uncorrelated for different delay taps p. Equation (2.42) is a version of the time-variant weight function with discrete paths and a graphical representation in Fig. 2.8. With the time-variant weight function the time-variant spreading function is obtained as

$$s(t^*; \tau, \nu) = \sum_{p=0}^{P-1} a_p \Xi_p(t^*; \nu) \delta(\tau - \tau_p) \,, \tag{2.44}$$

with $\Xi_p(t^*; \nu)$ being the Fourier transform of $g_p(t)$ at an arbitrary time instant $t = t^*$. According to [Pät02] the power delay profile (PDP) is given by

$$P_\tau(\tau) = \sum_{p=0}^{P-1} a_p^2 \delta(\tau - \tau_p) \,, \tag{2.45}$$

which means that the power spectrum is a discrete line spectrum weighted by the coefficients a_p. If the coefficients are normalized by

$$\sum_{p=0}^{P-1} a_p^2 = 1 \quad \text{and} \quad \sum_{n=1}^{N_p} c_{n,p}^2 = 1, \tag{2.46}$$

then the time-variant joint delay Doppler pdf $p(t;\tau,\nu)$ approximates the local scattering function $\mathcal{C}(t;\tau,\nu)$ with the frequency f being left out.

The presented simulation model generalized the WSSUS result by allowing coefficients that are calculable by time-variant pdfs of the Doppler frequency. The time-variant coefficients of the Gaussian processes gradually change the shape of the Doppler spectrum and therefore create a non-stationary stochastic process, which is needed for M2M channel models.

2.4 Geometric Channel Modeling

Pure geometric or deterministic channel modeling is principally based on ray tracing techniques. An exact propagation environment from transmitter to receiver is considered in such a model and the propagation is completely deterministic. All propagation paths and mechanisms have to be known in advance in order to implement a realistic scenario. For all occurring propagation mechanisms the electric properties of the interacting objects have to be known. As every single interaction of the electromagnetic waves with every possible object that causes reflection, scattering or diffraction on its way from transmitter to receiver has to be taken into account, the complexity of the model grows very fast with the size of the scenario.

However, for limited scenarios quite accurate channel models can be created. A selection of ray tracing modeling techniques are provided , e.g., in [MFSW04, Mau05]. Since geometric channel modeling is not the topic of this thesis, it is left to the reader to explore the rich literature.

2.5 Geometric-Stochastic Channel Modeling

The third channel modeling technique combines the advantages of stochastic and geometric channel models and is called geometric-stochastic channel modeling in [PRR02]. As the name implies a GSCM uses elements from both geometric and stochastic models.

Especially in the non-WSSUS case, this particular modeling technique becomes very useful. The GSCM departs from a purely stochastic model and allows to incorporate the geometry of the propagation environment, thus introducing the non-stationarity. The earlier presented purely stochastic channel models lack such a non-stationarity and represent an average over all possible environments.

In the geometric-stochastic modeling technique, the location of the transmitter, receiver and scatterers are taken into account. With this geometric setting, the

stochastic distributions of the delay and Doppler frequency are derived. The benefit of such a modeling technique for V2V communications is presented in [KTC+09a]. In this paper, the authors explain the measurement data presented in [PZB+08] from a GSCM perspective. The authors distribute the diffuse scatterers randomly in two stripes along the highway and determine their contribution to the channel impulse response (CIR). Monte Carlo simulations are used to determine the CIR, since an analytic solution cannot be obtained.

Other theoretical approaches to obtain closed form solutions for a geometric setup are given in [PHY08, ZS08, ZS09]. A prerequisite for these approaches is the knowledge of the stochastic distribution of the scatterers. In [PHY08, PHYK05] the scatterers are distributed on a circle, whereas in [ZS08] the scatterers are distributed on the surface of a cylinder. These distributions make a mathematical derivation tractable. The obtained results are, however, not easily adaptable to other propagation environments. Additionally, they do not fully agree with the measurement data, e.g., presented in [PZB+08]. In this thesis, certain stochastic distributions for the scatterers are used and they are distributed on ellipses, which are the geometric shapes of an equal delay. The purely geometric description of the Doppler frequency then allows for a closed form solution of the Doppler pdf.

The development of new communications systems continues and in the last couple of years M2M channels came into the focus of the scientific community. Since for those channels both the transmitter and the receiver are mobile, the models describing such channels must be non-stationary. The use of geometric-stochastic modeling methods is therefore recommended. In the following two paragraphs, we present two prominent examples of M2M channels: the V2V channel and the A2A channel.

2.6 Vehicular Channel Models

The V2V channel is the most used M2M channel at the moment and there exists a large scientific community doing research in this area. The United States Department for Transportation, for example, funds and promotes the development of ITSs. In Europe ERTICO was established as a platform for the cooperation of all relevant stakeholders to develop and deploy ITSs. Such systems consist of advanced applications that make transportation safer and more efficient. In order to provide these services, cars need to share information or sensor data. V2V communications is needed as an enabler for ITSs, since cars have to communicate with each other. There are already two V2V communications standards. They are called wireless access in vehicular environments (WAVE) and dedicated short-range communica-

tions (DSRC) [IEE10]. Both systems work in the ITS licensed frequency band of $f_c = 5.9\,\text{GHz}$. As the name indicates, both standards are intended for short-range communications in this frequency band.

If every car is connected to its neighbors, the cars will form an ad-hoc network, where all cars share their information. This mesh network can distribute information from infrastructure next to the road. Another field, where vehicular networks might be advantageous, are military networks. Military vehicles should exchange tactical information in order to coordinate their movements.

After showing the applications of V2V communications, it becomes clear that a good understanding of the propagation conditions is necessary. Since there is a lot of activity in this field, there are already a large number of publications. We summarize the most important papers, show their contributions and point out open questions. A good survey of vehicular channel modeling campaigns is presented in [MTKM09]. The article describes current V2V measurement campaigns in different environments and presents the most important parameters thereof. Surveys of V2V channel modeling techniques are found in [Mat08, MW09, MMK+11]. There, the authors explain the two most commonly used channel modeling approaches in the V2V sector: stochastic and geometry-based modeling. A survey on different channel models for V2V environments can be found in [Zaj12], where Zajić dedicates a whole chapter to this particular propagation channel. She concentrates on small scale fading and shows analytic results for determining the correlation functions for the two ring and two cylinder model, respectively. A glimpse of V2V channels for next generation wireless systems is presented in [MT14].

Among the first papers presenting measurement data for a vehicular environment are [ATI04, AI06, AMI06, AMI07]. The authors show, what we later introduce as delay-dependent Doppler pdf. The carrier frequency is $f_c = 2.45\,\text{GHz}$, i.e., exactly half of the dedicated carrier frequency located around 5.9 GHz. The measurement results from these publications will be used to confirm our theoretical model later in the thesis.

A large wide-band V2V measurement campaign was conducted in Lund, Sweden. The results from this campaign are presented in [PKC+07a]. Delay-Doppler plots from this campaign can be found in [PKC+07b] and show both the delay-dependence of the Doppler power spectrum and its non-stationarity. The invalidity of the WSSUS assumption for V2V channels based on those measurements is shown in [PZB+08]. An extensive elaboration of the vehicular channel in the 5 GHz band including measurement data is presented in Paier's PhD thesis [Pai10]. Another PhD thesis working partially with the same measurement data and investigating the

non-stationarity in vehicular wireless channels was done by Bernadó [Ber12]. Both authors use an approximation of the LSF to describe the channel. The parametrization of the LSF is shown in [BZP+09]. In this thesis, we want to put our results in relation with the LSF and show that the time-variant pdfs describe essentially similar properties of the channel. Since our description of the channel only concerns the scattering caused by objects close to the roadside, it is difficult to compare measurement data from others with our theoretical results. Hence, we conducted a V2V measurement campaign ourselves.

Other theoretical non-stationary models have been proposed. A non-stationary one-ring model for V2V channels is presented in [BP13], whereas in [CP11] a non-stationary V2V multiple-input/multiple-output (MIMO) model is shown. A model for non-isotropic scattering is presented in [CWL+09b,CYW+13,YWC+14]. Another model is describe in [ZXZJ14], which combines ellipses and rings. Most of these models are actually based on two ring models, e.g., [HPYK05, PHYK05].

The vast number of publications shows that there are a lot of aspects that need to be considered in the vehicular environment. There are publications concentrating on LOS and non-LOS environments. Other publications treat MIMO systems for vehicles. Furthermore, there are many factors that influence the V2V channel. For example traffic density, vehicles' velocities, vehicles' distances, and the type of road have an impact on the channel in these scenarios. There is a myriad of combinations possible, so that it is unlikely that there will be one single vehicular channel model that manages to describe all the different facets of the V2V channel.

We deliberately choose to concentrate on scattering in V2V channels, since the scattering causes the largest Doppler spread. The measurement data indicates that scattering effects cannot be neglected in the received signal, since the received power is not considerably lower than that of the direct component. Furthermore, the time-varying nature of the Doppler pdf makes the channel model non-stationary. One of the advantages of our model is that it can be combined with other models that describe different aspects of the channel like the direct and the reflected multipath components.

2.7 Aeronautical Channel Models

Another example of an M2M channel is the A2A channel. An overview over aeronautical radio communications systems is given in [Sta08]. The aeronautical channel describes the propagation environment between two aircraft. The channel can be seen as an extension of the V2V channel, where the two-dimensional geometry

of the environment is extended to the three-dimensional case. A three-dimensional angle of arrival (AOA) is presented in [ANBS10]. The Doppler power spectrum for scattering coming from all directions is shown in [CK97]. An ellipsoidal model for air-to-ground communications is presented in [NR02].

Differences occur in the directions, where the scattered signals come from. In the V2V case, the scattering mainly comes from the sides, whereas in the A2A case the scattering comes from below. Another difference is the almost always present LOS component of the aeronautical channel together with the ground-dependent specular reflection.

According to Bello [Bel73], the surface scatter channel for air-to-satellite communications includes three main components: the direct component, the specular reflection component, and the scatterer components. The first two components ideally consist of only one contribution. In measurements, however, fading is induced due to the non-resolvability of components arriving at the same discretized time step due to the finite bandwidth of the receiver. The third component consists of a sum of contributions with different delays and Doppler frequencies. Thus, the scattering components cause a considerable spread in delay and Doppler, whereas the first two components of the channel only cause a delay and Doppler shift. Naturally, the first component possesses the strongest power at the receiver in level flight. The power of the second component depends on the reflection properties of the ground. Above flat water, for example, the reflected component becomes almost as strong as the direct component. If the aircraft bank and the main lobe of the antenna is pointing towards the ground, the reflected component might even become stronger than the direct component. The power of the scattered components depends on the ground properties as well. In addition to the reflection coefficient, the roughness of the ground plays an important role. The roughness determines how much of the signal is reflected or scattered. Typical values for the reflection properties of different surfaces can be found in Table 1 of [Jak94] and values for the surface roughness are found in [Bel73].

A good survey on aeronautical channel models, especially on air-to-ground channel models, is presented in [Mat12]. Bello was also interested in aeronautical channel modeling and presented his findings in [Bel73]. In his paper, he focuses on the scattering components and derives expressions for channel correlation functions. For this he uses the WSSUS theory presented before.

Haas and Höher investigate in [Haa02,HH99] air-ground and air-to-air channels for the very-high frequency (VHF) band for different phases of flight, i.e., parking, taxiing, take-off, landing, and en-route. The stochastic description is based on the

WSSUS framework by Bello. Theoretical considerations based on the geometry lead to the derivation of delay and DPS. Notably, the presented Doppler power spectra were not known before, since they differed vastly from terrestrial communications channels. A validation with measurement data, however, is not provided.

A working group of the International Civil Aviation Organization (ICAO) presented a channel model for the VHF band. In [RC99] a large and small scale fading model is used to model the propagation effects for a digital system like VHF data link (VDL).

Apart from models, aeronautical channel measurements were conducted in order to see how the channel behaves in reality. Darian and Wilson determined the path loss and fading characteristics for the VHF propagation channel in [DW96]. Large and small scale fading statistics were presented by Dyer and Gilbert in [DG97].

Airport surface area channel models were presented by Gligorević in [Gli13] and Matolak in [MSX08, SM08a]. Those models are similar to terrestrial channel models and they use the same stochastic parameters to describe the channel. The similar description is motivated by the fact that only one entity is moving. Furthermore, the terminal buildings are comparable to buildings in urban channel models, where the LOS component is often blocked.

Air-to-air communications has only recently come into the focus of the research community. Such channels are needed for example for the propagation environment of automatic dependent surveillance-broadcast (ADS-B) transmissions during the flight or passenger internet communications via a mobile ad-hoc network [MHRR12, WFS10]. Data exchange between aircraft might be useful in all phases of the flight and applications are still being developed.

Common to many of the models presented before is that they are an adapted version of terrestrial channel models. For air-to-ground communications such assumptions are reasonable, since the ground station stays fixed during the communications process. Furthermore, the strong direct component makes the channel models relatively simple compared to terrestrial communications. The A2A channel, however, is a highly time-variant and non-stationary channel [AWL08], where the terrestrial models must not be applied anymore. The intended range for an A2A communications systems is much higher than the range of V2V communications. The critical scenarios for aircraft, when it comes to scattering, are when they are close to the ground, i.e., shortly after take-off and shortly before landing. The en-route scenario with an unobstructed LOS component should not distort the signal much.

In this work, we present a novel geometric-stochastic modeling technique, where the non-stationarity is included by the geometry. Therefore, we extend the two di-

mensional model derived for V2V communications to a three dimensional model in order to use it for A2A communications as well. The similarities and differences of both models are discussed. Furthermore, a comparison with measurement data validates the derived theoretical model.

Chapter 3

Measurement Campaigns

Prior to modeling an unknown communications channel, measurement data needs to be recorded. Measurement campaigns are therefore an essential activity before the modeling starts. In the following, we describe the preparation and execution of two measurement campaigns for measuring the V2V and A2A channel. The evaluation of the collected data then allows to create a mathematical model of the propagation environment. Measurement data is also essential in verifying theoretical models that have been developed by others.

3.1 Channel Sounder

3.1.1 Parameter Selection and Devices

Before conducting the measurements, thorough consideration has to go into the planning of the measurement campaign. The most important task is the selection of suitable measurement parameters. The selection of the measurement parameters is mainly influenced by the propagation mechanisms that need to be investigated. The transmit power P_t determines the maximum distance, for which the propagation effects can still be distinguished from the receiver noise. The carrier frequency f_c should be as close as possible to the carrier frequency of the intended communications system. The bandwidth B determines the resolution of the multipath components, i.e., specular reflection components or scattering components, which can be calculated by

$$\Delta\tau = \frac{1}{B}\,. \tag{3.1}$$

The bandwidth should always be larger than the bandwidth in the intended communications system in order to resolve the multipath components. Furthermore,

the detectable multipath components depend on the maximum measurable delay of the impulse response $\tau_{\max}$. If the objects causing multipath components are too far away, either the received power is too small or it appears as alias in the CIR.

The channel sounder sends its test signal every T_g seconds and hence the CIR is periodic. Consequently, the maximum detectable Doppler frequency ν is determined by the periodic transmit interval T_g of the CIR. It is given by

$$\nu = \pm \frac{1}{2T_g} . \tag{3.2}$$

The measurement of the Doppler frequency should be adapted to the expected velocities of transmitter and receiver.

After the measurement parameters have been selected, a measurement device, which fulfills the prerequisites, is needed. For the measurements presented throughout this thesis, a MEDAV channel sounder [Med] was used. The channel sounder can be operated at carrier frequencies of $f_c = 250\,\text{MHz}$, $1.51\,\text{GHz}$, $3.5\,\text{GHz}$, and $5.2\,\text{GHz}$. In the thesis, carrier frequencies of $f_c = 250\,\text{MHz}$ for the A2A measurements and $f_c = 5.2\,\text{GHz}$ for the V2V measurements are utilized.

The channel sounder itself consists of three main components:

- portable transmitting station (PTS),
- radio-frequency tuner (RFT),
- digital receiving unit (DRU).

The PTS creates the transmission signal, i.e., an OFDM-like signal in the frequency domain. The maximum measurable delay of the CIR can be selected out of the following six values of $\tau_{\max} \in \{0.8, 1.6, 3.2, 6.4, 12.8, 25.6\}\mu\text{s}$. The corresponding base-band signal is then modulated onto the carrier frequency f_c. The PTS creates a $0\,\text{dBm}$ output signal, which is then amplified by a power amplifier. In both measurement campaigns we use solid-state amplifiers from Bonn Elektronik: for the V2V campaign we work with the BLMA 2060-5 and for the A2A campaign with the BLMA 0525-35, respectively.

The transmitted signal is received and processed by the RFT. In the RFT the radio signal is amplified and down-converted to an intermediate frequency of $f_{IF} = 70\,\text{MHz}$. The down-converted signal is sent to the DRU. The DRU correlates the received signal by the known transmit signal and thus obtains an estimation of the frequency response. The DRU stores the estimated frequency response and controls the AGC of the RFT.

Apart from the estimated frequency response data, the DRU additionally stores the time and position of the receiver from an external global positioning system (GPS) device via a serial connection. We use the Septentrio PolaRx2e GPS receiver [Sep], which is a highly accurate GPS receiver that allows to pinpoint its position in the meter range using the standalone mode.

The position of the transmitter is recorded with a GPS device as well. In the V2V case, we use another Septentrio PolaRx2e GPS receiver, whereas for the A2A campaign, we used the IGI GPS receiver of the aircraft, which had a similar accuracy. In order to align the position data of the transmitter with the position data of the receiver, the GPS time of the receiver was extracted from the estimated frequency response data and the corresponding TX position was determined.

3.1.2 Synchronization

In order to synchronize transmitter and receiver, the highly accurate Rubidium atomic clocks LPFRS from Temex Time are used. According to the data sheet [Tem], the Allan deviation [All66] in stable temperature, gravity, pressure, and magnetic field conditions is given by $\Gamma \leq 5 \cdot 10^{-11}$ within 1 h after being 24 h switched off. For the V2V measurements with a carrier frequency of $f_c = 5.2\,\mathrm{GHz}$, the frequency deviation at transmitter and receiver is therefore calculated as

$$\Delta\nu \leq \Gamma f_c = 5 \cdot 10^{-11} \cdot 5.2\,\mathrm{GHz} = 0.26\,\mathrm{Hz}\,. \tag{3.3}$$

With the carrier frequency of $f_c = 250\,\mathrm{MHz}$ in the A2A campaign the resulting deviation in the frequency at transmitter and receiver is

$$\Delta\nu \leq \Gamma f_c = 5 \cdot 10^{-11} \cdot 250\,\mathrm{MHz} = 0.0125\,\mathrm{Hz}\,. \tag{3.4}$$

Compared to the resolution of the Doppler frequency in both cases, the error can be neglected. Therefore, the clocks on transmitter and receiver are sufficiently synchronized.

Another concern for the stability of the clocks are the vibrations induced by the aircraft or vehicle and the temperature dependency of the clock. For this purpose the Rubidium clock is installed in a 19" housing on springs that absorb most of the vibrations caused by vehicles and aircraft. Furthermore, a heating and a temperature sensor are added in the housing to keep the clock at a constant ambient temperature. The clock itself is run with 24 V DC in order to avoid fluctuations of the voltage source.

3.2 V2V Campaign

In the V2V campaign, the propagation mechanisms between two vehicles are investigated. Similar campaigns are described in [MFW02, ZSPN08, CWL09a, KP08, WCL09, AKT+11, SM08b]. In [MFW02] a narrow-band measurement with $B = 3\,\text{kHz}$ is presented, where the statistical distribution of the amplitude is evaluated. A MIMO V2V measurement campaign at $f_c = 2.435\,\text{GHz}$ is shown in [ZSPN08]. The theoretical double cylinder model presented in [ZS09] is validated in [ZSPN08] by measurement data. In [CWL09a] the Doppler spectrum of a GSCM is compared with measurement data from [AMI07]. Kunisch provides in [KP08] path loss models, PDPs, and DPSs for the V2V channel at $f_c = 5.9\,\text{GHz}$ with a bandwidth of $B = 3\,\text{kHz}$. In [AKT+11] MIMO measurements at $f_c = 5.6\,\text{GHz}$ with a bandwidth of $B = 240\,\text{MHz}$ are shown to identify the underlying propagation mechanisms. The delay spread, amplitude statistics, and correlations are investigated in [SM08b] at $f_c = 5.12\,\text{GHz}$ with a bandwidth of $B = 50\,\text{MHz}$. An overview over both channel measurements and channel models can be found in [WCL09]. In our measurement campaign, we explicitly concentrate on the scattering focusing on its non-stationary effects. Thus, the route is specially chosen to provide a rich scattering environment. In the following, the selected measurement parameters as well as the vehicles, the chosen route and the installed antennas are described.

3.2.1 Measurement Parameters

The carrier frequency for the V2V campaign is chosen to be close to the frequency of V2V communications systems, which operate at $f_c = 5.9\,\text{GHz}$. The closest available and freely usable frequency is $f_c = 5.2\,\text{GHz}$. This frequency is close enough to the deployment frequency in order to observe similar propagation mechanisms. We use a measurable CIR length of only $\tau_{\max} = 12.8\,\mu\text{s}$ compared to $\tau_{\max} = 25.6\,\mu\text{s}$ in the A2A campaign, since multipath components with a larger delay are not expected at a carrier frequency of $f_c = 5.9\,\text{GHz}$.

The shorter CIR, however, allows to record the CIR every $T_g = 1.024\,\text{ms}$ instead of $T_g = 2.048\,\text{ms}$ for a longer CIR, which leads to a maximum detectable Doppler frequency of $\nu_{\max} = \pm 488\,\text{Hz}$. For the measurements, we therefore had to restrict the absolute velocities of the cars to $\|\mathbf{v}\| = 30\,\text{km/h}$ in order to avoid aliasing. The model, however, can be scaled to higher Doppler frequencies for highway environments.

The selected bandwidth is the maximum bandwidth of the channel sounder with $B = 120\,\text{MHz}$, which results in a delay resolution of $\Delta\tau = 1/B = 8.33\,\text{ns}$. The

Table 3.1. *Measurement parameters for the V2V campaign*

Parameter	Value
Center Frequency, f_c	5.2 GHz
Bandwidth, B	120 MHz
Max. Delay, τ_{max}	12.8 µs
Delay Resolution, $\Delta\tau$	8.33 ns
Time Grid, T_g	1.024 ms
Max. Doppler Frequency, ν_{max}	±488 Hz
Doppler Resolution, $\Delta\nu$	1 Hz
Frequency Grid, F_s	78.074 kHz
TX/RX Antenna	Magnetic-Mounted Vehicular Antenna
Polarization	Vertical
Transmit Power, P_t	37 dBm EIRP

resolution in Doppler frequency is $\Delta\nu = 1/\left(2N_bT_g\right) = 1\,\text{Hz}$, if the selected block size is $N_b = 1024$. All measurement parameters are summarized in Table 3.1.

As the channel sounder provides an estimate of the time-variant transfer function, we obtain

$$\hat{H}[q,n] = \hat{H}\left(qF_s, nT_g\right), \tag{3.5}$$

where $n \in \{0,\ldots,N_b-1\}$ and $q \in \{0,\ldots,Q-1\}$ denote the time and frequency indices, respectively. The resolution in the frequency domain is thus given by the sampling frequency $F_s = B/Q = 78.074\,\text{kHz}$ with $Q = 1537$. The estimated spreading function becomes $\hat{s}[m,k] = \hat{s}\left(m\Delta\tau, k\Delta\nu\right)$ with $m \in \{0,\ldots,Q-1\}$ and $k \in \{\lfloor -N_b/2+1\rfloor,\ldots,\lfloor N_b/2\rfloor\}$.

3.2.2 TX and RX Vehicle

The measurement vehicles that are used in the measurement are an suburban utility vehicle (SUV) for the transmitter and a van for the receiver. Since the transmit equipment fits into a small rack, we use the SUV and put the rack in its trunk. The larger number of recording devices on the RX side and the fact that the DRU has to be operated during the measurements make it necessary to use a van as RX vehicle. Both vehicles are shown in Fig. 3.1.

The SUV has a second battery as backup supply power for the measurement devices, if the main engine is turned off. The TX rack is equipped with the 24 V DC source EA-PS 5032-30A from Elektro Automatik, the Rubidium atomic clock LPFRS from Temex Time, the PTS from MEDAV, the high-power amplifier BLMA

Figure 3.1. *TX vehicle on the right and RX vehicle on the left are connected via cable, while the measurement crew conducts the calibration procedure to synchronize the atomic clocks.*

2060-5 from Bonn Elektronik, and the Rohde & Schwarz signal generator SMR 20 for upconversion of the signal, see Fig. 3.2a.

The RX racks are installed in the van. The van is equipped with a generator that provides electricity in case the engine is not running. The RX racks comprise the 24 V DC source EA-PS 5032-20A from Elektro Automatik, the DRU, the RFT, the low-noise amplifier (LNA) from MEDAV, the Rubidium atomic clock, LPFRS from Temex Time, a laptop recording the GPS data, the Septentrio PolaRx2e GPS receiver, the self-constructed power box that distributes the power, and an uninterruptible power supply, see Fig. 3.2b.

(a) *From top to bottom: amplifier, PTS, atomic clock, 24 V power supply, and signal generator in the TX vehicle.*

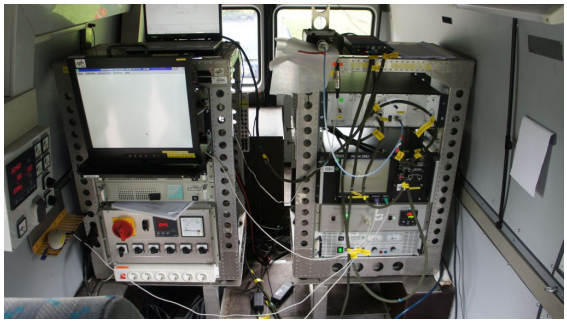

(b) *From top to bottom: monitor, USP, power box on the left, LNA, GPS receiver, RFT, DRU, atomic clock, and 24 V power supply on the right in the RX vehicle.*

Figure 3.2. *Measurement devices installed in the TX (left) and RX (right) vehicle.*

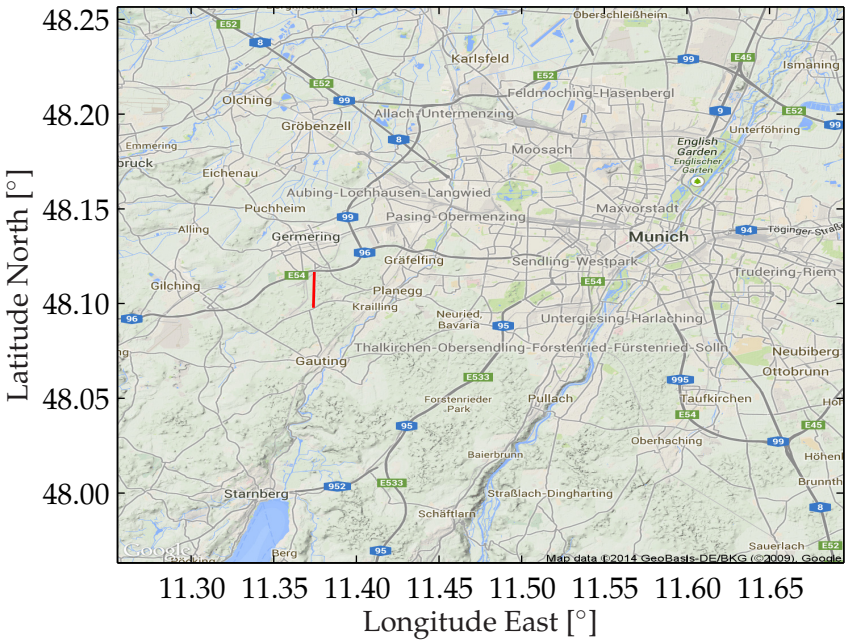

Figure 3.3. *The map shows the area southwest of Munich. The route through the forest is depicted by the red line. Image by Google, Map Data ©2014 GeoBasis-DE/BKG (©2009).*

3.2.3 Route

The route is selected in such a way that the scattering from the side of the road is strong. Therefore, we choose a road going through a forest in the southwest of Munich. The selected road is shown in Fig. 3.3. In doing so, we assume that the round tree trunks at the side of the road are perfectly suited to scatter back the transmitted signal. This assumption is later confirmed during the evaluation of the measurement results. The road is not highly frequented, so we avoid specular reflection components from other cars, since only scattering is in the focus of this investigation. An investigation on the specular reflection components can be found, for example, in [KTC+09a]. An additional advantage of the less frequented road is that we don't disturb the traffic, since as mentioned above the vehicles are restricted to drive with a maximum speed of $\|\mathbf{v}\| = 30\,\mathrm{km/h}$ due to the aliasing of the Doppler frequency.

The route begins south of the Germering and runs completely straight for about 2 km. The road consists of one lane per direction with a speed limit of 100 km/h. The measurement vehicles drive both in the same direction at a fixed distance and in opposite directions in different measurement scenarios. More details on the scenarios are provided in Chapter 4.

Table 3.2. *Electrical parameters of the vehicular antennas according to the data sheet*

Parameter	Value
Frequency, f_c	5 GHz to 6 GHz
Gain, G	6 dBi
VSWR	2 : 1
Impedance, Z	50 Ω
Power, P_t	10 W CW
Polarization	Vertical
Radiation	Omni-Directional in Azimuth Plane
Antenna RF Connector	SMA Male

3.2.4 Antennas

The employed antennas are the magnetic-mounted, vertically polarized, omni-directional, dipole antennas ECOM6-5500 from Mobile Mark [Mob]. Omni-directional antennas are used so that the scattering components contribute equally from all directions. The gain of the antennas is $G = 6\,\text{dBi}$. The electrical parameters of the antennas are summarized in Table 3.2.

3.3 A2A Campaign

The goal of the campaign is to characterize the channel in the aeronautical VHF band. An A2A campaign, however, is much more complex to prepare and conduct in comparison to a V2V campaign, since a certification process for the equipment is necessary. Such a certification process can only be provided by a lawful empowered company. The certification process for the A2A took about one year and was done by Rücker Aerospace. Eventually, we obtained a supplemental type certificate (STC) by the European Aviation Safety Agency (EASA) for both aircraft.

Since the certification process is elaborate and the aircraft expensive to fly, there are not as many measurement campaigns as in the V2V sector. For the air-to-ground channel a few measurement campaigns were conducted. The beyond the horizon propagation for the VHF air-to-ground channel is investigated in [VLC62]. The air-to-ground channel at $f_c = 2.05\,\text{GHz}$ is evaluated in terms of PDP and delay spread in [NMD+03]. The multipath statistics and path loss for the air-to-ground channel at $f_c = 5.7\,\text{GHz}$ is presented in [ML11]. Matolak studies the air-to-ground channel for UAVs at $f_c = 968\,\text{MHz}$ and $f_c = 5.06\,\text{GHz}$ in [MS14]. To the author's knowledge there are no publications on A2A measurement campaigns for VHF frequencies.

Figure 3.4. *TX aircraft Cessna C-208B Grand Caravan (D - FDLR) on the right and RX aircraft Dornier Do 228-101 (D - CODE) on the left. Both aircraft belong to DLR Flight Operations in Oberpfaffenhofen and Braunschweig, respectively.*

In the following we describe the measurement parameters, the two research aircraft, the routes, the antennas and the physiological training of the measurement crew.

3.3.1 Measurement Parameters

The selection of measurement parameters followed a similar path as in the V2V campaign. The chosen parameters for the A2A measurement campaign are summarized in Table 3.3. A carrier frequency of $f_c = 250\,\text{MHz}$ is used. This frequency is located in the aeronautical VHF band, where military communications takes place. Due to the large wavelength of $\lambda = c/f_c = 1.2\,\text{m}$ with respect to the terrain features, the scattering properties of the ground are good, which means the observed scattering is visible for longer delays in the measurement data than in the V2V scenario.

The originally in the project foreseen measurement bandwidth was $B = 50\,\text{MHz}$. But as we conducted some test measurements in front of the aircraft shelter, we detected the signal of the DAB transmitter Hohenpeißenberg, which transmits at a frequency of $f_c = 229.072\,\text{MHz}$ with an ERP of $P_t = 60\,\text{dBm}$. Therefore, the measurement bandwidth had to be reduced to $B = 20\,\text{MHz}$ in order to avoid interference from the DAB station. The delay resolution that is achieved with this bandwidth is $\Delta\tau = 1/B = 50\,\text{ns}$, which is still within the requirements.

The maximum measurable delay $\tau_{\max}$ is selected to be twice as long compared to the V2V campaign, since we expect scattering components with delays $\tau > 12.8\,\mu\text{s}$. Therefore, a maximum measurable delay of $\tau_{\max} = 25.6\,\mu\text{s}$ is chosen. For an altitude of $h_t = h_r = 600\,\text{m}$ of both aircraft a maximum horizontal distance of $d_{\max} = 7585\,\text{m}$ between transmitter and receiver is possible, before aliasing of the SR component

Table 3.3. *Measurement parameters for the A2A campaign*

Parameter	Value
Center Frequency, f_c	250 MHz
Bandwidth, B	20 MHz
Max. Delay, τ_{max}	25.6 µs
Delay Resolution, $\Delta\tau$	50 ns
Time Grid, T_g	2.048 ms
Max. Doppler Frequency, ν_{max}	$\pm$244 Hz
Doppler Resolution, $\Delta\nu$	0.5 Hz
Frequency Grid, F_s	38.986 kHz
TX/RX Antenna	Aeronautical Blade Antenna
Polarization	Vertical
Transmit Power, P_t	40 dBm ERP

occurs. During the measurement flights, the pilots have to ensure that the actual distance between the aircraft is always smaller than d_{max}.

The time-variant frequency response is recorded every $T_g = 2.048\,\text{ms}$, which leads to a maximum recordable Doppler frequency of $\nu_{max} = 1/(2T_g) = \pm 244\,\text{Hz}$. The maximum speed of the two aircraft is $\|\mathbf{v}\| = 300\,\text{km/h}$, which leads to a maximum achievable Doppler frequency of $f_{d,max} = 2\|\mathbf{v}\|f_c/c = 138.9\,\text{Hz}$. Therefore, the achievable Doppler frequency was below the maximum recordable Doppler frequency ν_{max}. In order to evaluate the Doppler frequency ν, we combine blocks of $N_b = 1024$ CIRs. The Doppler resolution is equal to $\Delta\nu = 1/(2N_bT_g) = 0.5\,\text{Hz}$. The parameters are summarized in Table 3.3.

The description of the estimated time-variant transfer function that is measured by the channel sounder $\hat{H}[q,n] = \hat{H}\left(qF_s, nT_g\right)$ and the estimated spreading function $\hat{s}[m,k] = \hat{s}\left(m\Delta\tau, k\Delta\nu\right)$ remains the same as in the V2V case. The sampling frequency however changes and is given as $F_s = B/Q = 38.986\,\text{kHz}$ with $Q = 513$.

3.3.2 TX and RX Aircraft

The A2A channel is measured by installing both the transmitter and receiver into two aircraft of DLR's research fleet. The transmitter was placed in a Cessna C-208B Grand Caravan (registration: D - FDLR) from DLR Flight Operations in Oberpfaffenhofen, see Fig. 3.4. The Cessna is a single-engine turboprop aircraft, which is capable of doing instrument flight rules (IFR) flights. However, we use the aircraft for visual flight rules (VFR) flights, since the scenarios can only be flown with this

(a) *From top to bottom: power box, PTS and amplifier installed in rack 2 of the TX aircraft.*

(b) *From top to bottom: Skymap GPS and CIR from the RUSK displayed on the monitors in rack 2 of the RX aircraft.*

Figure 3.5. *Measurement devices installed in the TX (left) and RX (right) aircraft.*

set of flight rules due to the desired low altitude. The cabin of the aircraft is non-pressurized, which means that the aircraft has to stay below 10,000 ft in order to fly without oxygen masks and not to damage the magnetic hard disks of the equipment. The measurement crew, however, has to conduct a special physiological training to get certified for flights which oxygen masks, see Section 3.3.5. The maximum speed of the Cessna is 184 knots true airspeed (KTAS). The Cessna is equipped with two 19" racks with the following components: 24 V DC source EA-PS 5032-20A from Elektro Automatik, a laptop to synchronize the clocks between transmitter and receiver, and the Rubidium atomic clock LPFRS from Temex Time in rack 1. The signal generator SSG2 from WORK Mircrowave, the PTS from MEDAV, the high power amplifier BLMA 0525-35 from Bonn Elektronik and the self-constructed power box are installed in rack 2, see Fig. 3.5a.

The RX aircraft is the twin-engined Dornier Do 228-101 (registration: D - CODE) from DLR Flight Operations in Braunschweig, see Fig. 3.4. The RX aircraft is larger than the TX aircraft, so that there is more space in the cabin for the slightly bigger RX equipment. The aircraft does not have a pressurized cabin. The maximum speed is 200 knots indicated airspeed (KIAS). The Do 228 is equipped with two 19" racks with the following components: the 24 V DC source EA-PS 9032-40A from Elektro Automatik, a computer to store both the VHF audio of the pilots and the GPS data, and the Rubidium atomic clock LPFRS from Temex Time in rack 1. The signal generator SSG2 from WORK Mircrowave, the RFT and DRU from MEDAV, the Septentrio PolaRx2e GPS receiver, the Skymap GPS receiver, and the self-constructed power

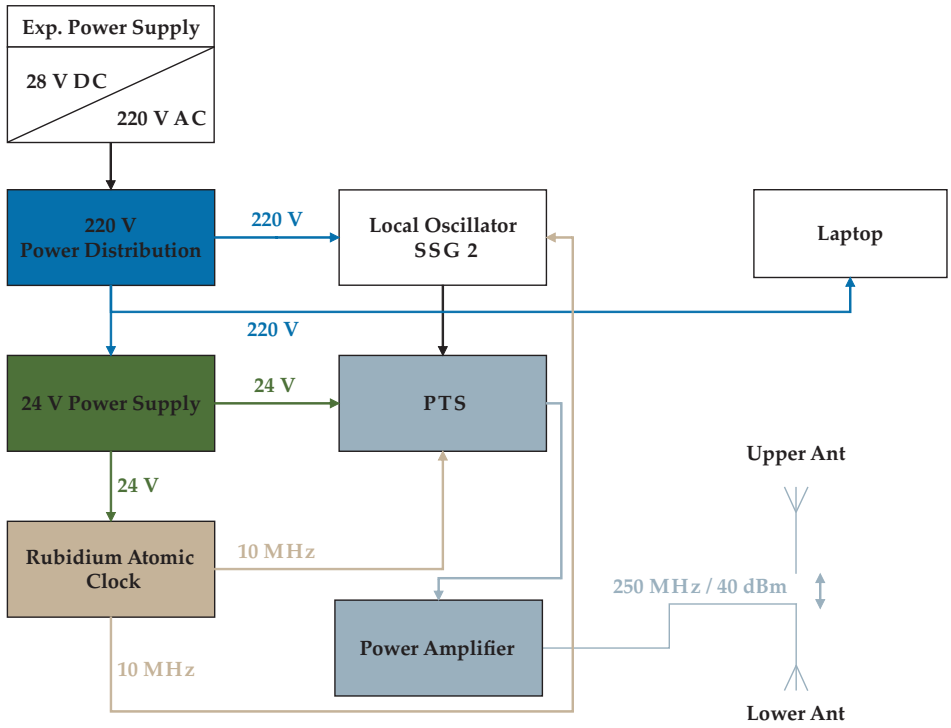

(a) *Block diagram of the electrical wiring in the TX aircraft.*

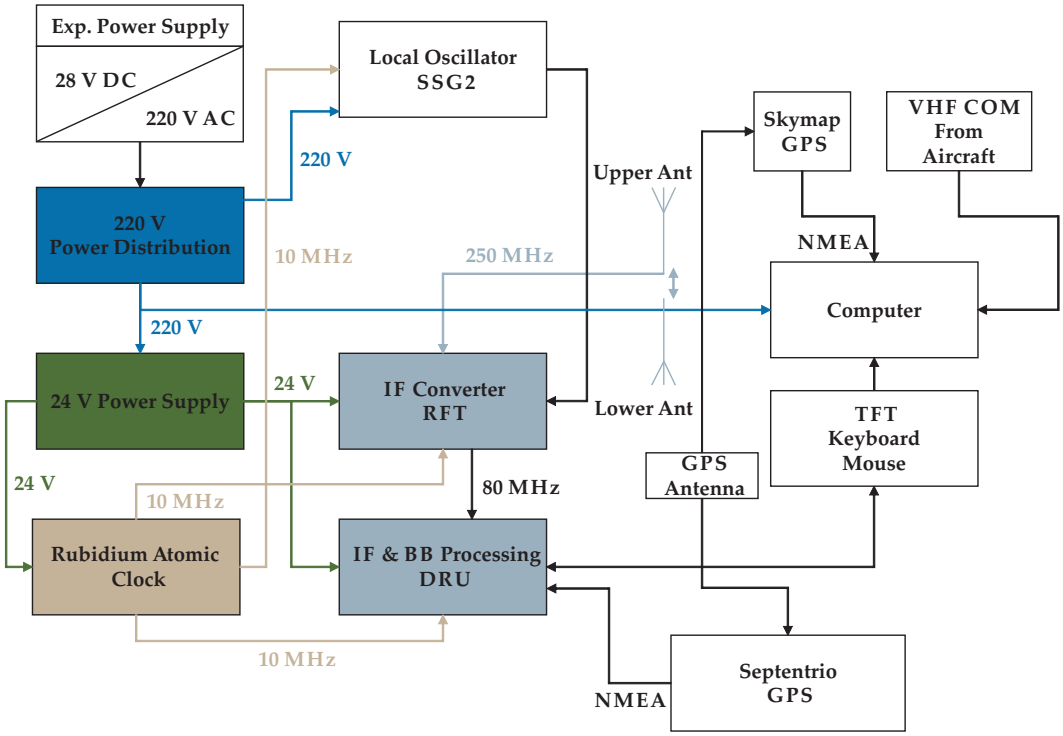

(b) *Block diagram of the electrical wiring in the RX aircraft.*

Figure 3.6. *Measurement devices and their electrical wiring for both TX and RX aircraft.*

box are installed in rack 2, see Fig. 3.5b. Block diagrams of the electrical wiring in the TX and RX aircraft are shown in Fig. 3.6a and Fig. 3.6b, respectively.

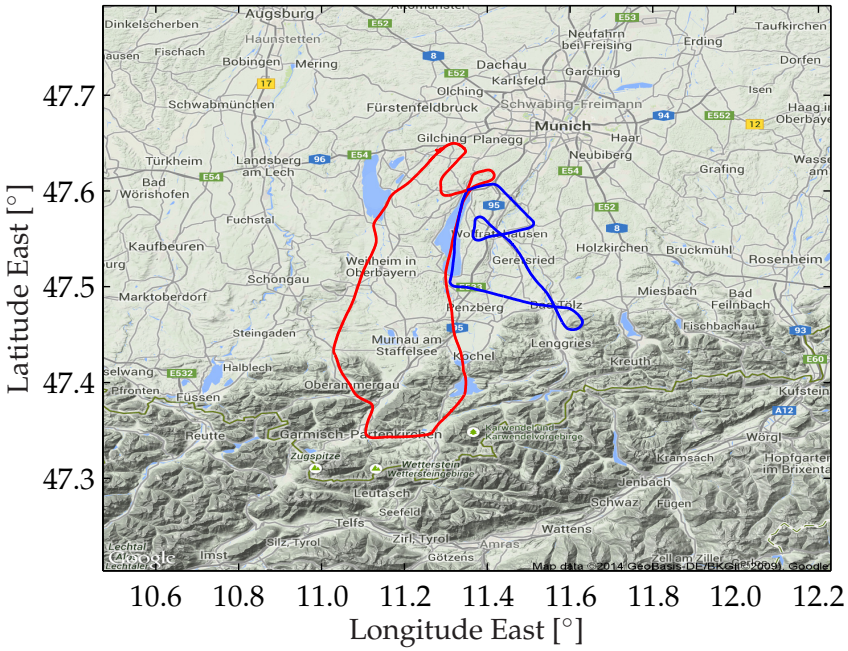

Figure 3.7. *The two different flight routes in Southern Germany. Image by Google, Map Data ©2014 GeoBasis-DE/BKG (©2009).*

3.3.3 Routes

The start and finish of the routes is the airfield Oberpfaffenhofen (EDMO), next to the DLR premises. The DLR's research aircraft use this airfield regularly for take-off and landing. The airfield features one runway with a length of 2286 m. Depending on the wind direction the runway is designated 04 (040°) or 22 (220°). Since westerly winds are predominant, runway 22 is used for all measurements.

Two different routes, shown in Fig. 3.7, are selected in such a way that they incorporate the flight over different terrains. The reflection and scattering properties of the terrain are of interest for us, since we expect the received power to be different for different terrain types. Therefore, we choose the area between Munich and the Alps as measurement environment with the right mixture of terrains, specifically: water, grassland, forest, urban areas, and mountainous valleys.

The first route is shown as the left loop in Fig. 3.7. The route consists of the start at Oberpfaffenhofen airfield, followed by a crossing of the Ammersee in a southerly direction towards Garmisch-Partenkirchen. There, the aircraft fly through alpine valleys at a very low altitude and exit northbound via Walchensee and Kochelsee. The flight continues due north to finally cross the Lake Starnberg before landing.

In order to measure scattering from urban areas, a flight across Munich would have been desirable. Due to the huge air traffic of Munich airport, it is not possible to

Table 3.4. *Electrical parameters of the aeronautical antennas according to the data sheet*

Parameter	**Value**
Frequency, f_c	225 MHz to 407 MHz
Gain, G	4 dBi
VSWR	$\leq 2.5:1$
Impedance, Z	50 Ω
Power, P_t	100 W CW
Polarization	Vertical
Radiation	Omni-Directional in Azimuth Plane
Antenna RF Connector	N Female

get permission to fly at a low altitude above Munich. Instead we fly south of Munich over Bad Tölz and Wolfratshausen. A loop is flown above each city to remain over the urban area. In the second route (right loop in Fig. 3.7) we cross Lake Starnberg as well, which acted as the common leg between the two routes. After the lake crossing, the route is concluded with the landing at airfield Oberpfaffenhofen.

3.3.4 Antennas

For transmitting and receiving the measurement signal, we use four VHF airborne blade antennas (21-30-18) from Cooper Antennas [Coo]. The antennas are made of a high-strength composite blade with an aluminum alloy base block. The environmental performance is according to MIL-STD-810 [Mil]. The antennas cover the following electrical specifications shown in Table 3.4.

The antennas are quarter-wave dipoles and therefore have an omni-directional radiation pattern in the azimuth plane. Such a pattern enables an equal reception of the scattering, if the aircraft are in level flight. The antennas are placed on a round metal plate that fits in one of the openings in the aircraft's fuselages. The metal plate acts as ground plane for the antennas.

The four antennas are placed on top and at the bottom of the fuselages of both aircraft. During the measurement flights only one of the two antennas is transmitting at the TX or receiving at the RX, respectively. Therefore, a single input/single output (SISO) measurement is conducted. Since we intend to investigate the influence of the ground scattering, the configuration with both TX and RX antenna at the bottom is the most promising one and the results shown in this thesis are evaluated for downward facing antennas.

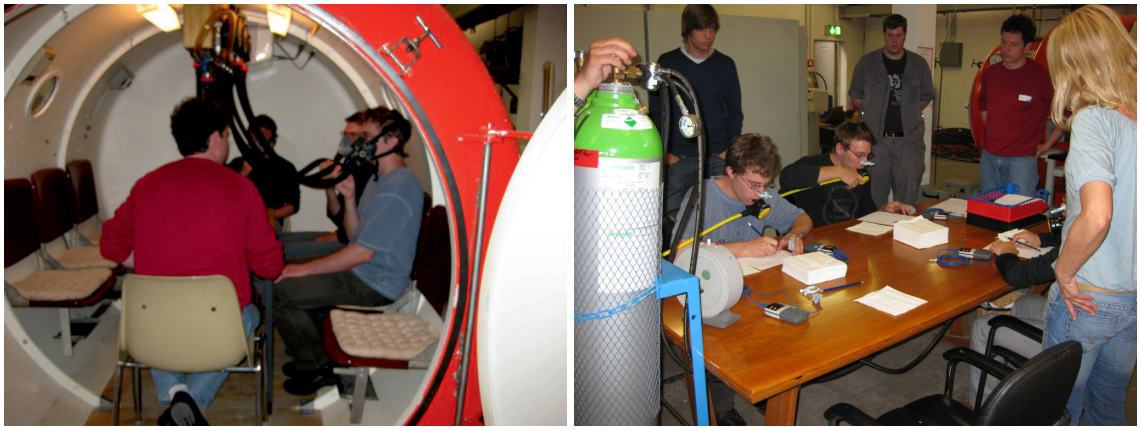

(a) *Participants sit in the hypobaric chamber and breath oxygen through the mask just before the hatch is closed.*

(b) *Participants perform calculations during the hypoxia test supervised by aviation physicians.*

Figure 3.8. *Physiological training at the aeromedical center in Cologne.*

3.3.5 Physiological Training

All measurement personnel, who work in the aircraft have to undergo the physiological training for participants of parabolic flights, since the aircraft do not possess a pressurized cabin and everyone in the aircraft is required to fly with oxygen masks above 10,000 ft. In total seven persons had to undergo this training in order get the permission to participate in the flights.

Apart from a theoretical introduction into altitude physiology (atmosphere physics, respiration, hypoxia, physiological consequences of decompression, etc.), this training includes a hypobaric chamber test, where the participants are brought to the equivalent pressure of about 30,000 ft, see Fig 3.8a. Furthermore, a hypoxia test, where the participants are deprived of oxygen and have to do calculations, see Fig. 3.8b, is carried out. The training was conducted at the aeromedical center (AeMC) in Cologne.

Chapter 4

Vehicle-to-Vehicle Channel

In this chapter, both the theory and the measurement data of the V2V channel are presented in detail. In the first part, a two-dimensional GSCM is developed to characterize the scatting that occurs in V2V channels. The results of the model are then compared to data that we collected during the measurement campaign described in Chapter 3. Parts of this chapter were published in [WSF14a], [WFZ14], and [WSF15].

The V2V channel represents a mathematical description of the propagation mechanisms between two moving vehicles. As mentioned before this channel differs insofar from the typical mobile radio channels that both the transmitter and receiver are mobile.

4.1 Components of the Channel

As mentioned in Chapter 2, the V2V channel can be divided into three different types of components: the direct component, the specular reflection components, and the scattered components.

4.1.1 Direct Component

The direct component is naturally the strongest contribution. In the V2V case, however, the direct path can be blocked by other vehicles or buildings depending on the scenario. It is therefore not guaranteed that it can always be received. When we look at the measurement data later on and specifically at the contributions from the scattering, the direct component is stronger than the scattered components in its vicinity. Thus, the contribution of the direct component overlaps the scattered components close to the direct component. However, the direct component is not part of

the investigation in this thesis. In most cases the direct component is only influenced by the free space path loss and can be simply added to the model, if needed.

4.1.2 Specular Reflection Components

In the vehicular case specular reflections can be caused by many objects. The main source of specular reflections stems from other vehicles due to their metallic constitution. Other sources might be guard rails or buildings next to the road and reflections from the road surface. The received power from the specular reflections can be strong and causes multipath fading. Since the SR components are influenced by the traffic density, this effect is dependent on time and location. Additionally, it has to be distinguished between stationary and moving reflectors. Publications that take moving reflectors into account can be found in [BP12,Zaj14,CP09]. Specular reflection components are not investigated in this thesis, since they have already been investigated, for example, in [KTC+09a]. The specular components can be added to the model similarly to the direct component.

4.1.3 Scattered Components

The scattered components and its modeling is the central part of this thesis. Scattering is caused, when the signal is scattered in different directions at rough surfaces of objects like trees. The received scattered components introduce not only a Doppler shift, but also a large Doppler spread. If the scatterers are close to the road, the large Doppler spread may cause a severe degradation of the performance of the communications system, since the received power is not negligible. The scatterers can be either stationary or moving, but in this thesis we focus on stationary scatterers with moving transmitter and receiver.

Thus, the scatterers are regarded in the model as a continuum of scatterers that are fixed in their locations and not as scattering points in a mathematical sense. The presented channel model explains how the received signal power is distributed in the Doppler domain for arbitrary delays. Furthermore, the model is non-stationary due to the geometric approach. This feature is necessary, when describing M2M channels.

The Doppler spectra for signals in M2M channels have already been investigated in numerous publications. In [WCL09] GSCMs are classified into regularly shaped GSCMs and irregularly shaped GSCMs. For the irregularly shaped GSCMs the scatterers are randomly distributed in space without any restrictions on the shape in order to better fit the measurements. The regularly shaped GSCMs, however, al-

low to use geometric shapes to mathematically describe the scattering, which leads to closed form solutions of the channel description, e.g., the Doppler pdf. There are only very few geometric shapes that allow for such a description. The regular shapes in two dimensional space, on which the scatterers are placed, are given by either a circle or an ellipse. Two circles are used to place local scatterers closely around transmitter and receiver. An ellipse is used, if scatterers with the same delay are considered. For the mentioned cases the geometric shapes correspond to either a narrowband or a wideband model.

If the scatterers are randomly distributed in space and the scattering for transmitter and receiver is assumed to be uncorrelated, the theoretic work done by Akki and Haber in [AH86] can be applied. We rewrite the presented DPS to get a pdf as

$$p(\nu) = \frac{1}{\pi^2 \sqrt{f_\mathrm{t} f_\mathrm{r}}} \mathrm{Q}_{-1/2}\left(\frac{(f_\mathrm{t}+f_\mathrm{r})^2+\nu^2}{2 f_\mathrm{t} f_\mathrm{r}}\right), \tag{4.1}$$

where f_t and f_r are the maximum Doppler frequencies induced by the movement of TX and RX, respectively. The Legendre function of the second kind $\mathrm{Q}_{-1/2}(x)$ is given by [AS65]

$$\mathrm{Q}_{-1/2}(x) = \mathrm{K}\left(\sqrt{\frac{1+\mathrm{x}}{2}}\right), \tag{4.2}$$

with $\mathrm{K}(k) = \int_0^{\pi/2} \frac{\mathrm{d}\zeta}{\sqrt{1-k^2\sin^2\zeta}}$ being the complete elliptic integral of the first kind. The mean Doppler and Doppler spread for the M2M are presented in [Akk94]. A simulation model based on a two-ring geometry is presented in [PSP05].

Equation (4.1) is well suited to describe double-bounce scattering, since it assumes f_t and f_r to be uncorrelated random variables. The Akki-Haber pdf is therefore obtained by convoluting two Jakes pdfs

$$p(\nu) = (p_\mathrm{t} * p_\mathrm{r})(\nu) = \int_{-\infty}^{\infty} p_\mathrm{t}(\nu - x) p_\mathrm{r}(x)\,\mathrm{d}x\,. \tag{4.3}$$

Equally, the pdf can be obtained by a Fourier transform of the product of the normalized auto-correlation functions, which results in

$$p(\nu) = \int_{-\infty}^{\infty} \mathrm{J}_0(2\pi f_\mathrm{t}\tau)\mathrm{J}_0(2\pi f_\mathrm{r}\tau)\exp(-\mathrm{j}2\pi\nu\tau)\,\mathrm{d}\tau\,, \tag{4.4}$$

where $\mathrm{J}_0(\cdot)$ is the zeroth-order Bessel function of the first kind. The integral can be solved by using (6.612) from [GR00]. Both (4.4) and (4.3) lead to the expression in (4.1).

The above mentioned Doppler pdf, however, cannot be used, if single-bounce scattering is assumed, since the assumption of independent TX and RX scattering angles is not valid anymore. The scattering occurs at only one object, which relates the angle of departure (AOD) and the AOA to each other. The ellipse is used as geometric shape to relate the angles of transmitter and receiver to each other. Additionally, we want to derive a *time-variant* pdf as proposed in [ODC09], which is not fulfilled for the Akki-Haber pdf.

Another advantage in using an ellipse for single-bounce scattering is that an ellipse naturally describes all the scatterers, which induce an equal delay from transmitter via scatterer to receiver. That property makes it possible to derive a wideband model of the channel. That means the Doppler pdf can be calculated for arbitrary delays. Since the relationship between the two angles is non-linear, closed form solutions for the delay-dependent Doppler frequency have been futile so far. With my model, however, it becomes possible to derive closed form solutions for the Doppler frequency that can be calculated for arbitrary delays τ. Since this procedure can be performed for all time instances t and therefore leads to different results, the channel model becomes non-stationary.

4.2 2D Model

In this section, the geometry and the stochastic distributions that are used to model scattering in the V2V channel are presented. The geometric and stochastic part are then combined to obtain a non-stationary, wideband model of the V2V channel. The geometry plays a crucial part in obtaining a non-stationary wideband model. But geometry is also very helpful in understanding the properties of the channel for a given scenario. By using geometric properties, the delay and Doppler frequency are related in a very natural way. In the stochastic part, the distribution of scatterers is presented in order to derive the Doppler frequency pdf. Since it is impossible to know, where all scatterers are located in a realistic scenario, a stochastic approach can cover a broader range of scenarios than a ray tracing approach.

4.2.1 Geometric Part

A two-dimensional Cartesian coordinate system is used for the mathematical description of the propagation scenario. Therefore, the scattered components are considered to arrive horizontally at the antenna. This means that the antenna height is negligible compared to the distances between the vehicles and the scatterers. The

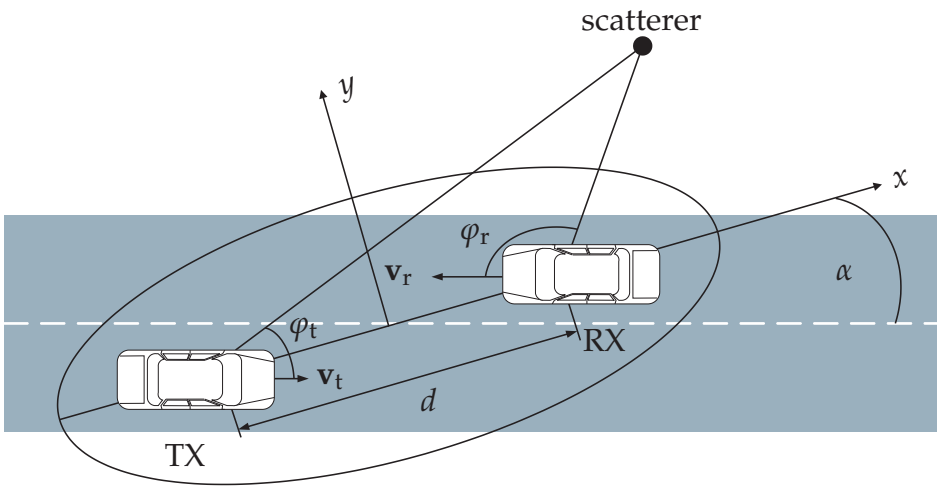

Figure 4.1. *The transmitter, receiver, and an arbitrary scatterer are placed in a Cartesian coordinate system. Both cars are in the foci of the delay ellipse.*

coordinate system is a *moving* coordinate system, which moves along the transmitter and receiver such that the origin of the coordinate system is placed exactly in the middle between transmitter and receiver, see Fig. 4.1. The x-axis points along the connecting line between transmitter and receiver.

Without loss of generality, we place both vehicles on the x-axis. In general, the choice of placing the vehicles in the coordinate system is arbitrary. The choice made in this thesis merely simplifies the model definition. Due to the movement of both vehicles their position is time-varying. In the chosen coordinate system the position $\mathbf{x}(t) = [x(t), y(t)]^{\mathrm{T}}$ of both cars can be described as

$$\mathbf{x}_{\mathrm{t}}(t) = \mathbf{x}_{\mathrm{t}0} + \int_0^t \mathbf{v}_{\mathrm{t}}(\tau)\,\mathrm{d}\tau\,, \quad \text{and} \quad \mathbf{x}_{\mathrm{r}}(t) = \mathbf{x}_{\mathrm{r}0} + \int_0^t \mathbf{v}_{\mathrm{r}}(\tau)\,\mathrm{d}\tau\,, \tag{4.5}$$

where $\mathbf{x}_{\mathrm{t}0} = [-d/2, 0]^{\mathrm{T}}$ and $\mathbf{x}_{\mathrm{r}0} = [d/2, 0]^{\mathrm{T}}$ are the initial positions of the transmitting and receiving vehicle, respectively, and $\mathbf{v}_{\mathrm{t}}(t) = [v_{\mathrm{t}}^x, v_{\mathrm{t}}^y]^{\mathrm{T}}$ and $\mathbf{v}_{\mathrm{r}}(t) = [v_{\mathrm{r}}^x, v_{\mathrm{r}}^y]^{\mathrm{T}}$ are the corresponding velocity vectors.

Consider the distance $d_{\mathrm{sc}}(\mathbf{x}, t)$ that a transmitted signal travels between the moving transmitter and receiver over a stationary scatterer located at coordinates $\mathbf{x}$. Following straightforward geometrical considerations $d_{\mathrm{sc}}(\mathbf{x}, t)$ can be expressed as

$$d_{\mathrm{sc}}(\mathbf{x}, t) = \|\mathbf{x} - \mathbf{x}_{\mathrm{t}}(t)\| + \|\mathbf{x} - \mathbf{x}_{\mathrm{r}}(t)\|\,, \tag{4.6}$$

where $d_{\mathrm{t}}(\mathbf{x}, t) = \|\mathbf{x} - \mathbf{x}_{\mathrm{t}}(t)\|$ is defined as the distance between transmitter and scatterer and $d_{\mathrm{r}}(\mathbf{x}, t) = \|\mathbf{x} - \mathbf{x}_{\mathrm{r}}(t)\|$ as the distance between receiver and scatterer, respectively. The delay τ of the signal can be determined by $\tau_{\mathrm{sc}}(\mathbf{x}, t) = d_{\mathrm{sc}}(\mathbf{x}, t)/c$, where c is the speed of light.

The other important parameter of the received signal is the Doppler frequency ν. The Doppler frequency describes the change in frequency due to the movement of transmitter, receiver and/or scatterer. For only one moving vehicle, e.g., TX or RX, the Doppler frequency is described according to [Par00] by

$$\nu = \cos(\varphi) \frac{\|\mathbf{v}\|}{c} f_c \,, \tag{4.7}$$

where $\mathbf{v}$ is the velocity vector of the moving vehicle and φ the angle between the vehicle and the scatterer. If the scatterers are distributed uniformly in space around the receiver, the Doppler pdf is given by (2.23).

If two objects are moving, as it happens in the V2V scenario, the equation becomes more involved. For a moving transmitter, a moving receiver and a stationary scatterer, one obtains the following expression [CKZ+10]

$$\nu(\varphi_t(t), \varphi_r(t)) = \|\mathbf{v}_t\| \cos(\varphi_t(t)) + \|\mathbf{v}_r\| \cos(\varphi_r(t)) \,, \tag{4.8}$$

where $\varphi_t(t)$ is the angle between the vector connecting the transmitter and scatterer and the velocity vector of the transmitter. $\varphi_r(t)$ is the angle between the vector connecting the receiver and scatterer and the velocity vector of the receiver, see Fig. 4.1.

Although, at first glance, (4.8) is relatively simple, its practical use for the analytic derivation of $\nu(\varphi_t(t), \varphi_r(t))$ is rather limited, as the position of a scatterer is rarely known in practice. Moreover, we do not know the number of scatterers in a general propagation environment. The unknown and random spatial distribution of scatterers, as well as their high number, are two major factors that motivated us to use stochastic methods to compute the Doppler pdf. The Jakes Doppler pdf [Jak94] is a classical result that exemplifies such an analysis. Unfortunately, in the case of two moving vehicles, a similar stochastic analysis of (4.8) becomes prohibitively complex due to the $\cos(\varphi_t(t))$ and $\cos(\varphi_r(t))$ terms. The stochastic approach would presume a certain law, i.e., a pdf behind a spatial distribution of scatterers. This will inevitably incur a stochastic distribution of the $\varphi_t(t)$ and $\varphi_r(t)$ functions in (4.8), whose joint distribution under a non-linear transformation by a cosine function becomes prohibitively complex to analyze analytically. Instead, a slight modification in the way expression (4.8) is computed can significantly simplify the analytic computation of the Doppler profiles, as outlined in the following.

Therefore, we use a different, but equally applicable formula to calculate the Doppler frequency. As mentioned before the Doppler frequency can be seen as the instantaneous change in frequency due to the movement of TX and RX, which is caused by a time-varying delay of the propagation path. In [Bel73] it is shown that

the Doppler frequency is proportional to the negative rate of change of the delay, which means

$$\nu(\mathbf{x},t) = -\frac{\partial}{\partial t}\tau_{\mathrm{sc}}(\mathbf{x},t) f_{\mathrm{c}} = -\frac{\partial}{\partial t} d_{\mathrm{sc}}(\mathbf{x},t)\frac{f_{\mathrm{c}}}{c}\,. \tag{4.9}$$

By using (4.6) we can compute the Doppler frequency in dependence on the scatterers' location $\mathbf{x}$. The equation becomes

$$\begin{aligned}\frac{\partial}{\partial t} d_{\mathrm{sc}}(\mathbf{x},t) &= -\mathbf{v}_{\mathrm{t}}(t)^{\mathrm{T}}\frac{(\mathbf{x}-\mathbf{x}_{\mathrm{t}}(t))}{\|\mathbf{x}-\mathbf{x}_{\mathrm{t}}(t)\|} - \mathbf{v}_{\mathrm{r}}(t)^{\mathrm{T}}\frac{(\mathbf{x}-\mathbf{x}_{\mathrm{r}}(t))}{\|\mathbf{x}-\mathbf{x}_{\mathrm{r}}(t)\|} \\ &= -\begin{bmatrix}\mathbf{v}_{\mathrm{t}}(t)^{\mathrm{T}}\mathbf{v}_{\mathrm{r}}(t)^{\mathrm{T}}\end{bmatrix}\begin{bmatrix}\mathbf{e}_{\mathrm{t}}\\ \mathbf{e}_{\mathrm{r}}\end{bmatrix}.\end{aligned} \tag{4.10}$$

where we have defined $\mathbf{e}_{\mathrm{t}} = \frac{(\mathbf{x}-\mathbf{x}_{\mathrm{t}}(t))}{\|\mathbf{x}-\mathbf{x}_{\mathrm{t}}(t)\|}$ and $\mathbf{e}_{\mathrm{r}} = \frac{(\mathbf{x}-\mathbf{x}_{\mathrm{r}}(t))}{\|\mathbf{x}-\mathbf{x}_{\mathrm{r}}(t)\|}$. Note that the vectors $\mathbf{e}_{\mathrm{t}}$ and $\mathbf{e}_{\mathrm{r}}$ are unity vectors. They point from transmitter to an arbitrary scatterer at $\mathbf{x}$ and from receiver to the scatterer, respectively. For the calculations we assume that the distance d_{sc} does not change while the signal is traveling from transmitter to receiver, i.e., $\|\mathbf{v}\| \ll c$.

Alternatively, we can consider the spatial change of the distances $d_{\mathrm{t}}(\mathbf{x},t)$ and $d_{\mathrm{r}}(\mathbf{x},t)$ to obtain the Doppler frequency. Therefore, we need to compute the gradient of the distances, which result in

$$\nabla d_{\mathrm{t}}(\mathbf{x},t) = \mathbf{e}_{\mathrm{t}} \qquad \text{and} \qquad \nabla d_{\mathrm{r}}(\mathbf{x},t) = \mathbf{e}_{\mathrm{r}}\,. \tag{4.11}$$

Equation (4.11) is then combined with (4.10) to obtain

$$-\frac{\partial}{\partial t} d_{\mathrm{sc}}(\mathbf{x},t) = \begin{bmatrix}\mathbf{v}_{\mathrm{t}}(t)^{\mathrm{T}} & \mathbf{v}_{\mathrm{r}}(t)^{\mathrm{T}}\end{bmatrix}\begin{bmatrix}\nabla d_{\mathrm{t}}(\mathbf{x},t)\\ \nabla d_{\mathrm{r}}(\mathbf{x},t)\end{bmatrix} = \begin{bmatrix}\mathbf{v}_{\mathrm{t}}(t)^{\mathrm{T}} & \mathbf{v}_{\mathrm{r}}(t)^{\mathrm{T}}\end{bmatrix}\begin{bmatrix}\mathbf{e}_{\mathrm{t}}\\ \mathbf{e}_{\mathrm{r}}\end{bmatrix}. \tag{4.12}$$

Thus, both the temporal and the spatial derivative have to be similar to the continuity equation. Depending on which equation you use, it allows for a slightly different interpretation of the Doppler frequency. Using the spatial derivative, the Doppler frequency is computed as

$$\nu(\mathbf{x},t) = \left(\mathbf{v}_{\mathrm{t}}(t)^{\mathrm{T}}\nabla d_{\mathrm{t}}(\mathbf{x},t) + \mathbf{v}_{\mathrm{r}}(t)^{\mathrm{T}}\nabla d_{\mathrm{r}}(\mathbf{x},t)\right)\frac{f_{\mathrm{c}}}{c}\,, \tag{4.13}$$

which can be interpreted as instantaneous Doppler frequency caused by the scatterers mentioned in [Boa92]. The temporal derivative is hereby replaced by the scalar product of spatial derivative and velocity vectors of the transmitter and receiver, respectively. This particular representation allows for a straightforward calculation of the Doppler frequency for an arbitrary scatterer at location $\mathbf{x}$ in Cartesian coordinates.

Consider $\nu(\mathbf{x}, t)$ at a certain observation time $t = t^*$. Our goal is to use (4.13) to compute Doppler frequencies for all possible scatterer positions that induce the same delay $\tau_{\mathrm{sc}}(\mathbf{x}, t^*) = \tau$; in other words, we consider all scatterers that induce the same propagation path length

$$d_{\mathrm{sc}}(\mathbf{x}, t^*) = d_{\mathrm{t}}(\mathbf{x}, t^*) + d_{\mathrm{r}}(\mathbf{x}, t^*) = \tau c\,. \tag{4.14}$$

Since all scatterers that induce the same delay lie on an ellipse, we set $d_{\mathrm{sc}}(\mathbf{x}, t^*) = 2a_\tau$ with $a_\tau \in [(\|\mathbf{x}_{\mathrm{t}}(t^*) - \mathbf{x}_{\mathrm{r}}(t^*)\|)/2, \infty)$. The transmitter and receiver are in the foci of the ellipse [PB82]. The parameters of the ellipse are determined by [BSMM07]

$$a_\tau = \frac{\tau c}{2}\,, \quad b_\tau = \sqrt{\frac{\tau^2 c^2}{4} - \frac{\left(\|\mathbf{x}_{\mathrm{t}}(t^*) - \mathbf{x}_{\mathrm{r}}(t^*)\|\right)^2}{4}}\,, \tag{4.15}$$

where a_τ is the semi-major axis and b_τ the semi-minor axis of the ellipse. Both ellipse parameters are time-variant, because the distance between transmitter and receiver is time-variant. Since the coordinate system moves along the transmitter and receiver, the center of the ellipse remains in the origin of the coordinate system. An arbitrary position on the ellipse can be calculated by the parametric equation as

$$\mathbf{x}(t^*; \phi|\tau)^1 = \begin{bmatrix} a_\tau \cos\phi \\ b_\tau \sin\phi \end{bmatrix}\,, \tag{4.16}$$

where $\phi \in [0, 2\pi)$. For a given delay a_τ and b_τ are fixed. Note that ϕ does *not* correspond to the polar angle of the scatterer position and the x-axis. In astronomy the parameter ϕ is called eccentric anomaly. If the polar angle φ is needed, it can be calculated as

$$\tan\varphi = \frac{a_\tau}{b_\tau}\tan\phi\,. \tag{4.17}$$

The Doppler frequency for an arbitrary, but fixed delay is given by inserting (4.16) into (4.13). It results in

$$\begin{aligned} &\nu(t^*; \mathbf{x}(\phi|\tau)) = \nu(t^*; \phi|\tau) = \\ &= \frac{(a_\tau\cos\phi + d/2)}{\sqrt{(a_\tau\cos\phi + d/2)^2 + (b_\tau\sin\phi)^2}}\frac{v_{\mathrm{t}}^x}{c}f_{\mathrm{c}} + \frac{(a_\tau\cos\phi - d/2)}{\sqrt{(a_\tau\cos\phi - d/2)^2 + (b_\tau\sin\phi)^2}}\frac{v_{\mathrm{r}}^x}{c}f_{\mathrm{c}} \\ &+ \frac{b_\tau\sin\phi}{\sqrt{(a_\tau\cos\phi + d/2)^2 + (b_\tau\sin\phi)^2}}\frac{v_{\mathrm{t}}^y}{c}f_{\mathrm{c}} + \frac{b_\tau\sin\phi}{\sqrt{(a_\tau\cos\phi - d/2)^2 + (b_\tau\sin\phi)^2}}\frac{v_{\mathrm{r}}^y}{c}f_{\mathrm{c}}\,. \end{aligned} \tag{4.18}$$

The Doppler frequency depends only on the parameter ϕ for a fixed time t^* and given delay τ. Because we reduced the number of parameters, it becomes feasible to derive closed form solutions for the Doppler frequency pdf for moving transmitter and receiver.

[1] The position vector $\mathbf{x}$ is evaluated for ϕ under the condition of τ, i.e., for a certain $\tau = \tau_0$ similar to a conditional pdf $p(\cdot|\cdot)$.

4.2.2 Stochastic Part

In this section, we explain the stochastic part of the model. In the subsequent analysis, the pdfs of the Doppler frequency for arbitrary delays are derived.

The derivation of the delay-dependent Doppler pdf $p(t;\nu|\tau)$ can be done, if we assume a certain distribution $p(t;\phi|\tau)$ of the scatterers on the ellipse. For simplicity reasons we derive the pdfs for a fixed time $t = t^*$. Therefore, we omit the parameter t in the following. To derive $p(\phi|\tau)$ we need to make additional assumptions on the spatial distribution of scatterers on the ellipse. One particular choice that is computationally attractive is a uniform distribution of scatterers. Such an assumption is not unreasonable in practice and it has also been widely used, e.g., in derivation of the Jakes Doppler spectrum [Jak94]. However, this does not imply that the distribution $p(\phi|\tau)$ is uniform on an ellipse, as shown in the following.

Nørklit has shown in [NA98], how the distribution on the ellipse is calculated. Below we summarize the key steps of this procedure. First, the differential arc length $\mathrm{d}l$ of an ellipse with semi-major axis a_τ and semi-minor axis b_τ is derived. The differential arc length depends on an differential increase of ϕ in the following way

$$\mathrm{d}l = a_\tau \sqrt{1 - \epsilon_\tau^2 \cos^2\phi}\,\mathrm{d}\phi\,, \tag{4.19}$$

where $\epsilon_\tau = \sqrt{a_\tau^2 - b_\tau^2}/a_\tau$ is the eccentricity of the ellipse. Under the assumption that the scatterers are uniformly distributed on the ellipse, we claim that the arc length l is uniformly distributed in a sense that the density of scatterers on the ellipse per differential length $\mathrm{d}l$ is the same. Therefore, the pdf $p(l|\tau)$ must be uniform, i.e., $p(l|\tau) = L_\tau^{-1}$ with L_τ being the circumference of the ellipse. L_τ is calculated by

$$L_\tau = a_\tau \int_0^{2\pi} \sqrt{1 - \epsilon_\tau^2 \cos^2\phi}\,\mathrm{d}\phi = 4a_\tau \int_0^{\pi/2} \sqrt{1 - \epsilon_\tau^2 \cos^2\phi}\,\mathrm{d}\phi = 4a_\tau \mathrm{E}(\epsilon_\tau)\,, \tag{4.20}$$

where we define $\mathrm{E}(\epsilon_\tau) = \int_0^{\pi/2} \sqrt{1 - \epsilon_\tau^2 \cos^2\zeta}\,\mathrm{d}\zeta$ as the complete elliptic integral of the second kind [AS65].

As the pdf $p(l|\tau)$ is known, we can derive $p(\phi|\tau)$ by a probability transformation. According to [PP02] we get

$$p(\phi|\tau) = \frac{p(l|\tau)}{\left|\frac{\mathrm{d}\phi}{\mathrm{d}l}\right|}\,, \tag{4.21}$$

where the pdf $p(l|\tau)$ gets divided by the Jacobian determinant. The substitution of the variable and subsequent division by the Jacobian determinant ensures that the

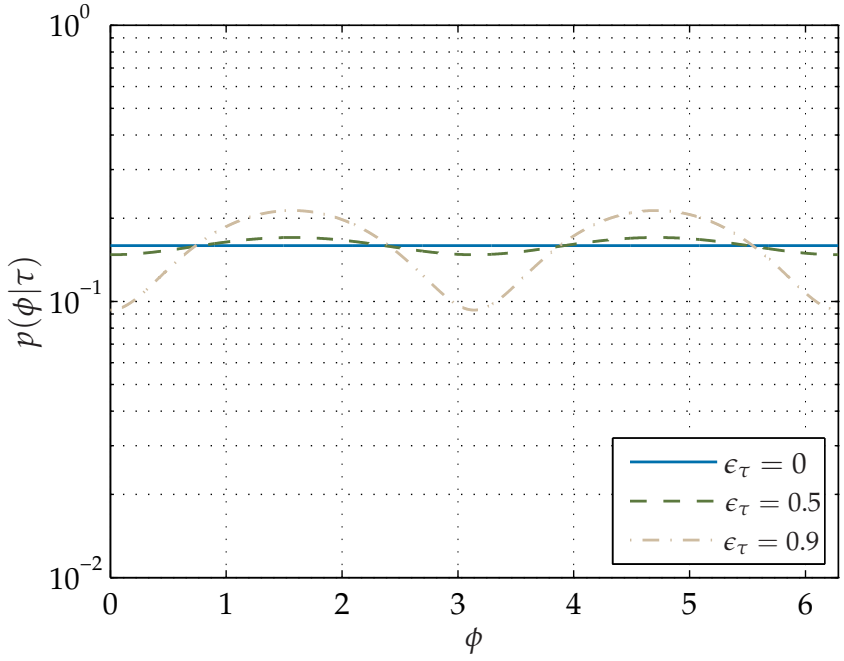

Figure 4.2. *$p(\phi|\tau)$ shown for different values of the eccentricity ϵ_τ.*

value of the integral over the pdf remains the same. By applying (4.21) with (4.19) and (4.20), the pdf $p(\phi|\tau)$ becomes

$$p(\phi|\tau) = \frac{\sqrt{1-\epsilon_\tau^2\cos^2\phi}}{4\int_0^{\pi/2}\sqrt{1-\epsilon_\tau^2\cos^2\zeta}\,\mathrm{d}\zeta} = \frac{\sqrt{1-\epsilon_\tau^2\cos^2\phi}}{4\mathrm{E}(\epsilon_\tau)}, \tag{4.22}$$

where $\phi \in [0, 2\pi)$. The shape of $p(\phi|\tau)$ is only dependent on the eccentricity ϵ_τ of the ellipse, which in turn is a function of the delay τ. The pdf $p(\phi|\tau)$ is evaluated for three different values of ϵ_τ in Fig. 4.2. The larger the delay, the closer the distribution $p(\phi|\tau)$ is to a uniform distribution. With $p(\phi|\tau)$ having been calculated, the pdf for the Doppler frequency $p(\nu|\tau)$ is derived by using another probability transformation similar to the one in (4.21). However, the calculation is more difficult, since the relation $\mathcal{F} : \phi \mapsto \nu(\phi|\tau)$ is a many-to-one mapping. This mapping means that multiple values of ϕ can result in the same Doppler frequency. Thus, the mapping is ambiguous. Hence, there exists no unambiguous inverse relation. For the derivation of $p(\nu|\tau)$ the ambiguity needs to be taken into account. Therefore, it is necessary to sum over all ϕ' that result in the same Doppler frequency. The pdf becomes

$$p(\nu|\tau) = \sum_{\phi' \in \left\{\mathcal{F}^{-1}(\nu)\right\}} \frac{p(\phi'|\tau)}{\left|\frac{\mathrm{d}\nu}{\mathrm{d}\phi'}\right|}, \tag{4.23}$$

where $\mathcal{F}^{-1}$ is the inverse relation $\nu(\phi|\tau) \mapsto \phi$. The inverse relation results in a countable and finite set $\left\{\mathcal{F}^{-1}(\nu)\right\}$. The proof of this assertion involves enumeration

Algorithm 1 Computation of $p\left(t^*;\nu^{[m]}|\tau^{[n]}\right)$

1: **for** $\tau^{[n]} \in [\tau^{\min}, \tau^{\max}]$ **do**
2: Compute the parameters a_τ,b_τ and ϵ_τ of the ellipse corresponding to the delay $\tau^{[n]}$
3: Use (4.22) to compute $p(\phi|\tau^{[n]})$ for the corresponding scenario
4: **for** $\nu^{[m]} \in [\nu^{\min}, \nu^{\max}]$ **do**
5: Compute $p\left(t^*;\nu^{[m]}|\tau^{[n]}\right)$ by numerically solving (4.23) for each $\nu^{[m]}$.
6: **end for**
7: **end for**

of the intersection points of the delay ellipse with the curves of constant Doppler followed by invoking Bézout's Theorem [Abh90].

Since $\mathcal{F}^{-1}$ cannot be expressed in closed form, we calculate it numerically. For each Doppler frequency ν^* we solve $\nu^* - \nu(\phi|\tau) = 0$ for ϕ by looking for solutions in the interval $[0, 2\pi)$. In general, the number of solutions to $\nu^* - \nu(\phi;\tau) = 0$ can be different for different Doppler frequencies ν^*.

By inserting (4.19) and (4.22) into (4.23), the delay-dependent Doppler frequency pdf $p(\nu|\tau)$ is calculated. The result describes the distribution of the Doppler frequency at a fixed time t^* for an arbitrary delay τ and for uniformly distributed scatterers. It follows from (4.23) that arbitrary scatterer distributions can be inserted. A suitable delay distribution $p(\tau)$ allows for the calculation of the joint delay Doppler pdf $p(\tau,\nu) = p(\tau)p(\nu|\tau)$. Since the equations are valid for arbitrary time instances t, the *time-variant* joint delay Doppler pdf becomes $p(t;\tau,\nu)$. This particular pdf describes the distribution of delay τ and Doppler frequency ν for arbitrary times t. Thus, the distribution becomes time-variant. The time-variant, delay-dependent Doppler frequency pdfs are calculated by using Algorithm 1.

The computational rules considered above allow for computing the joint distribution of delay and Doppler frequency. Yet the computed pdf does not necessarily provide information about the power distribution of the scattered signals without further assumptions. In the popular WSSUS case, it can easily be shown that the scattering function of the channel is proportional to the joint pdf of delay and Doppler frequency [Hoe92]. Similarly, for quasi-wide-sense stationary uncorrelated scattering (QWSSUS) channels, this proportionality will hold for a limited time period and frequency range.

When the WSSUS assumption is violated, the situation, however, is more complicated. Due to the correlations between the amplitudes of scattered signals, as well as

their non-stationary behavior in time, the areas of high probability in $p(t;\tau,\nu)$ might not necessarily coincide with the areas of higher received power for the same parts of delay-Doppler plane. The generalized local scattering function (GLSF) [Mat05] that measures the average strength of scatterers for a specific delay and Doppler, i.e., the analogon of the scattering function for non-WSSUS channels, also does not explicitly consider the joint pdf of delay and Doppler frequency; the relationship between them is yet to be studied.

A possible way to explore this relationship is to consider a class of non-WSSUS channels that satisfy the DU property [Mat05]. We believe that for such channels the proportionality between the joint pdf $p(t;\tau,\nu)$ and the GLSF can be demonstrated. Our reasoning behind this belief is the following: In [Mat05] it was shown that the DU channels can be locally approximated by the QWSSUS model. The latter model would imply the exact proportionality of the pdf $p(t;\tau,\nu)$ and power received from the corresponding parts of the delay-Doppler plane. However, this analysis is still an open research problem.

4.3 Theoretical Results

The delay-dependent Doppler frequency pdf $p(\nu|\tau)$ can be related to other known Doppler pdfs such as the Jakes pdf. A geometric view is provided on how both pdfs are derived and we present a proof that in the limiting case of $\tau \to \infty$ the delay-dependent Doppler pdf converges to the Jakes pdf. For all simulations and measurements in this chapter a carrier frequency of $f_c = 5.2\,\text{GHz}$ is used. Note that all scenarios are evaluated at a certain time t^*, where the geometric set-up is as stated in the scenario description. The notation is simplified to $\mathbf{v}(t^*) = \mathbf{v}$. The delay-dependent Doppler pdf $p(t^*;\nu|\tau)$ and the joint delay Doppler pdf $p(t^*;\tau,\nu)$ are shown in the logarithmic domain, i.e., $10\log_{10}\left(p(t^*;\nu|\tau)\right)$ and $10\log_{10}\left(p(t^*;\nu|\tau)\right)$. For the delay-dependent Doppler pdf $\int_{-\infty}^{\infty} p(t^*;\nu|\tau) = 1$, whereas the joint delay Doppler pdf consists of contiguous slices of delay-dependent pdfs evaluated for different τ. Therefore, in a strict sense, they are not correctly scaled, but make the figures consistent.

The following assumptions are made in the two theoretical scenarios below:

- Scenario I: Two vehicles drive behind each other on the same lane, with the same speed in the same direction. The transmitter is at position $\mathbf{x}_{t0} = [-50, 0]^T\text{m}$ with velocity vector $\mathbf{v}_t = [90, 0]^T\text{km/h}$. The receiver is at position $\mathbf{x}_{r0} = [50, 0]^T\text{m}$ with velocity vector $\mathbf{v}_r = [90, 0]^T\text{km/h}$. The scatterers are uniformly distributed over the whole ground plane, see Fig. 4.3.

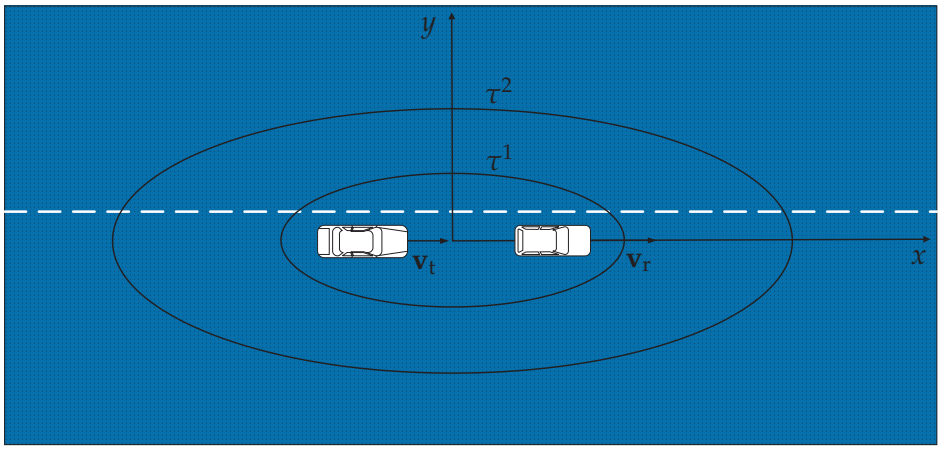

Figure 4.3. *Geometry for an infinite scatter distribution with vehicles driving in the same direction on a two lane road.*

- Scenario II: Two vehicles drive towards each other on the same lane, with the same speed. The transmitter is at position $\mathbf{x}_{t0} = [-50, 0]^T$m with velocity vector $\mathbf{v}_t = [90, 0]^T$km/h. The receiver is at position $\mathbf{x}_{r0} = [50, 0]^T$m with velocity vector $\mathbf{v}_r = [-90, 0]^T$km/h. The scatterers are uniformly distributed over the whole ground plane.

Those two scenarios are used to explain, how the geometry affects the shape of the Doppler pdf. In the following the scenarios are modified to reflect realistic environments, which are used for a comparison with measurement data.

Let us compare the geometric setup that leads to the Jakes pdf and the V2V Doppler pdf. For the Jakes pdf it is assumed that the scattered components arrive equally from all directions. According to [Zaj12] the scattered components that are placed everywhere on the ground can be replaced by so called "effective" scatterers that are distributed on a circle. The resulting Doppler frequencies caused by scattering from the ground and the ring of effective scattterers can be seen in Fig. 4.4a. Constant Doppler frequencies are represented as lines radiating out from the moving receiver as origin. If the Doppler frequency is evaluated on the circle, we obtain the Jakes pdf. The Jakes pdf does not depend on the size of the circle.

Scenario I: The Doppler frequency distribution in Fig. 4.4b looks similar to the Doppler frequency in Fig. 4.4a. However, in between the two moving vehicles the Doppler frequencies become different. The Doppler frequencies close to 0 Hz occupy a larger area, whereas for a moving receiver only the line orthogonal to the movement constitutes the 0 Hz line. Naturally, the maximum Doppler frequency is twice as high, since there are two vehicles moving in the same direction. The Doppler frequency in the V2V scenario is evaluated for a constant delay τ, which is

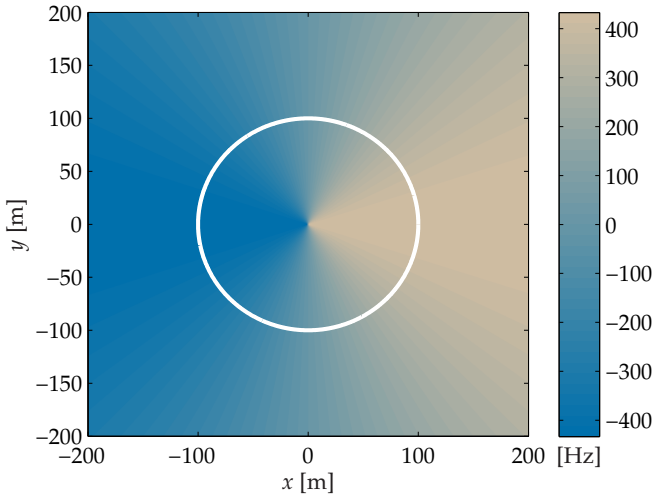

(a) *Doppler frequencies caused by a single vehicle at* $\mathbf{x}_{r0} = [0,0]^T\text{m}$ *with velocity vector* $\mathbf{v}_r = [90,0]^T\text{km/h}$ *(Jakes case). The circle indicates the locations of effective scatterers.*

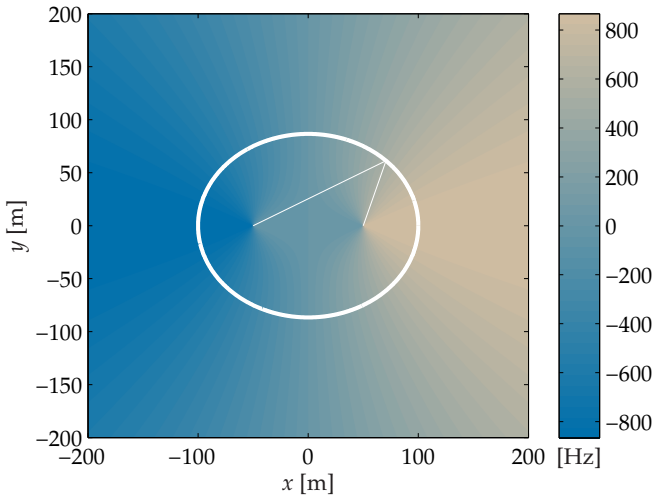

(b) *Doppler frequency caused by two vehicles at positions* $\mathbf{x}_{t0} = -\mathbf{x}_{r0} = [-50,0]^T\text{m}$ *with velocity vectors* $\mathbf{v}_t = \mathbf{v}_r = [90,0]^T\text{km/h}$. *The ellipse indicates scatterers inducing the same delay at the receiver.*

Figure 4.4. *Doppler frequencies caused by scattering from the ground.*

shown as ellipse in the figure. As mentioned before, the Doppler frequency can be interpreted as sum of the change of distance from transmitter to scatterer and the change from receiver to scatterer. The distances to an arbitrary scatterer are shown as white lines. This is very similar to the bistatic Radar scenario in [Ong03].

In order to compare the V2V Doppler pdf with the Jakes pdf, the joint delay Doppler pdf in Fig. 4.5a and the Doppler pdfs in Fig. 4.5b are shown. The first delay

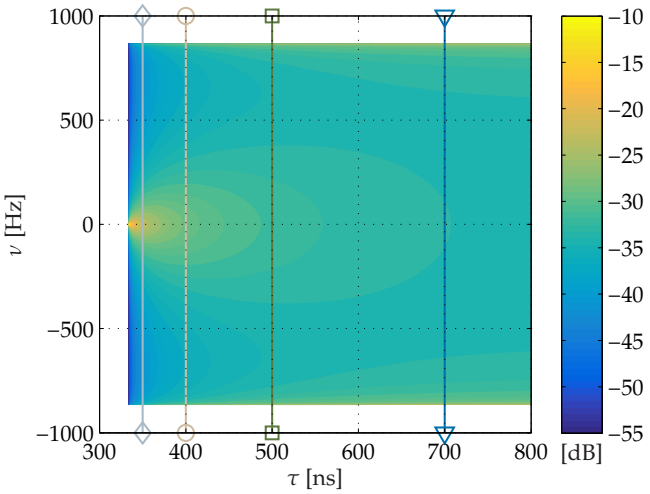

(a) *Joint delay Doppler pdf in logarithmic domain:* $10\log_{10}\left(p(t^*;\tau,\nu)\right)$. *Vertical lines indicate cuts through the pdf to obtain the delay-dependent Doppler pdfs shown in (b).*

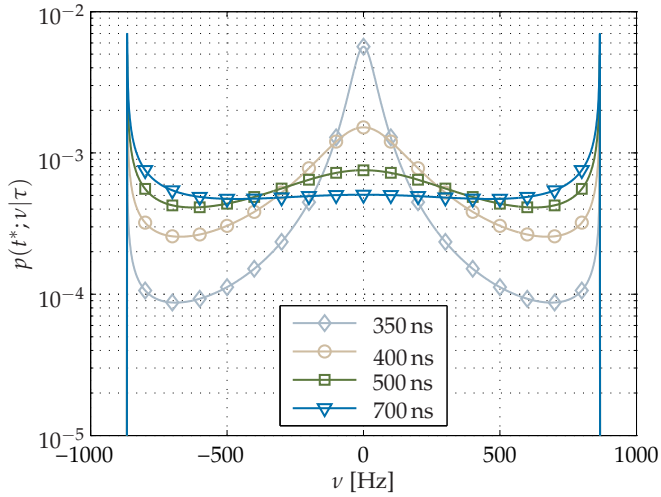

(b) *Doppler pdfs* $p(t^*;\nu|\tau)$ *for the different delays indicated in (a).*

Figure 4.5. *Scenario I: Vehicles at positions* $\mathbf{x}_{t0} = -\mathbf{x}_{r0} = [-50, 0]^T\text{m}$ *with velocity vectors* $\mathbf{v}_t = \mathbf{v}_r = [90, 0]^T\text{km/h}$.

value for the joint delay Doppler pdf occurs at the LOS delay of $\tau = 333\,\text{ns}$. With scattered components on the whole ground plane, the width of the Doppler pdf remains constant over all delays. For increasing delay the shape of the Doppler pdf changes. This change is shown in Fig. 4.5b. For a delay of $\tau = 350\,\text{ns}$ the pdf has a distinctive W shape. The different shape is a direct result of the Doppler frequency distribution on the ground shown in Fig. 4.4b, since the area of Doppler frequencies close to 0 Hz is larger than in the Jakes case. This circumstance means Doppler

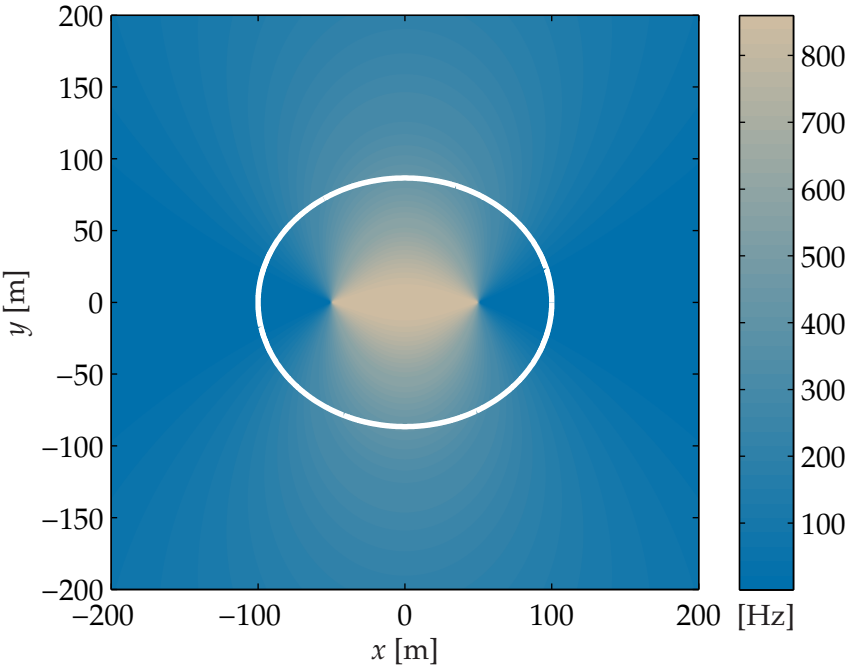

Figure 4.6. *Doppler frequency caused by two vehicles at positions* $\mathbf{x}_{t0} = -\mathbf{x}_{r0} = [-50, 0]^T$m *with velocity vectors* $\mathbf{v}_t = -\mathbf{v}_r = [90, 0]^T$km/h. *The ellipse indicates scatterers inducing the same delay at the receiver.*

frequencies close to 0 Hz are more probable. If the delay is increased, the Doppler frequency distribution on the ellipse becomes more similar to that on a circle, i.e., the Jakes pdf. In the case of $\tau = 700$ ns, the Doppler pdf already looks like the Jakes pdf. For $\tau \to \infty$, the Doppler distribution $p(\nu|\tau)$ is asymptotically converging towards the Jakes pdf. A proof for this assertion is found in Appendix D.

Since the Doppler frequency is only described by one parameter instead of two, the result is different from the Akki-Haber pdf in [AH86]. For single-bounce scattering, however, the assumption that angle of departure and angle of arrival are correlated is reasonable. For the case, where double-bounce scattering occurs, the Akki-Haber pdf should be applied, since the two scattering objects causing the Doppler frequencies are uncorrelated. Note that there exists no delay-dependent, double-bounce pdf so far.

Scenario II: The two cars drive in opposite directions. The Doppler frequency caused by scattering on the ground can be found in Fig. 4.6. The distribution of the Doppler frequency is completely different compared to the distribution shown in Fig. 4.4a. The high Doppler frequencies are all caused by scatterers located in the area between the two vehicles. The lines of constant Doppler for a Doppler frequency of, e.g., $\nu = 400$ Hz form a figure of eight. The minimum Doppler frequency

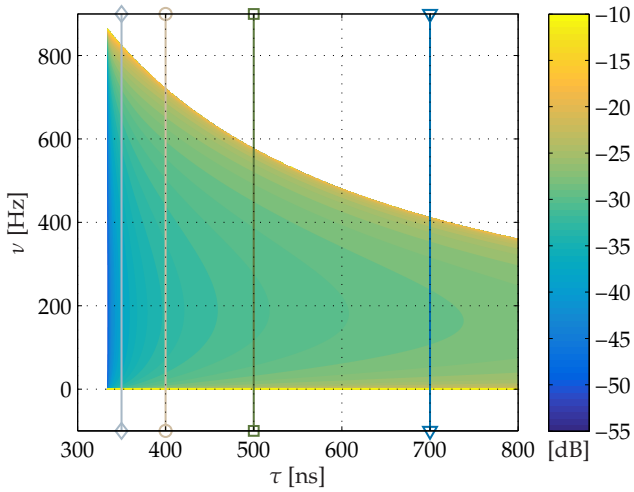

(a) *Joint delay Doppler pdf in logarithmic domain:* $10\log_{10}\left(p(t^*;\tau,\nu)\right)$. *Vertical lines indicate cuts through the pdf to obtain the delay-dependent Doppler pdfs shown in (b).*

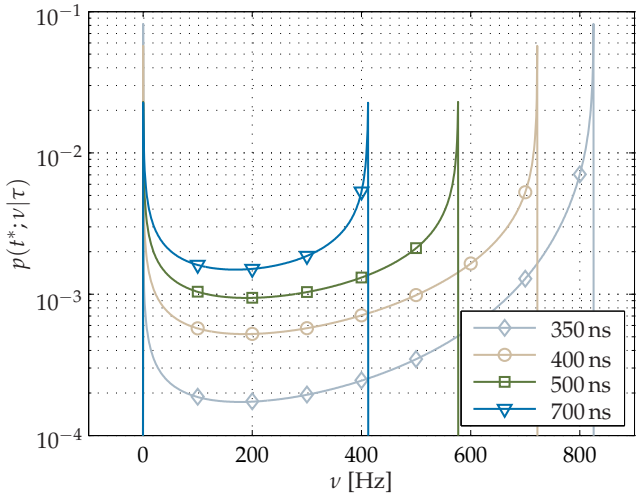

(b) *Doppler pdfs* $p(t^*;\nu|\tau)$ *for the different delays indicated in (a).*

Figure 4.7. *Scenario II: Vehicles at positions* $\mathbf{x}_{t0} = -\mathbf{x}_{r0} = [-50, 0]^T\text{m}$ *with velocity vectors* $\mathbf{v}_t = -\mathbf{v}_r = [90, 0]^T\text{km/h}$.

is $\nu = 0\,\text{Hz}$, which originates from scatterers located to the left of the transmitter and the right of the receiver. Compared to Scenario I, no negative Doppler frequencies occur. An ellipse to indicate scatterers that induce the same delay at the receiver is shown in Fig. 4.6.

The joint delay Doppler pdf and the Doppler pdfs for Scenario II are shown in Fig. 4.7a and Fig. 4.7b. As already seen in Fig. 4.6 the Doppler frequencies are only positive. The largest width of the Doppler pdf occurs for the delay of $\tau = 333.3\,\text{ns}$,

i.e., directly at the LOS. The maximum Doppler frequency decreases with increasing delay. The highest probability of occurrence arises for the maximum and minimum Doppler frequencies. As the maximum Doppler frequency decreases for increasing delay, the probability of the medium Doppler frequencies increases in order to keep the integral over the pdf constant.

The shape of the Doppler pdfs in Fig. 4.7b is very different from the shape in Scenario I. The pdfs look like asymmetric versions of the Jakes pdf. The W shape cannot be identified anymore. However, the decrease in width is clearly visible. For small delays like $\tau = 350\,\text{ns}$ the asymmetry is clearly obvious. The maximum and minimum Doppler frequencies possess the highest probability of occurrence. For large delays like $\tau = 700\,\text{ns}$, the Doppler pdf exhibits only half the width of pdf at $\tau = 350\,\text{ns}$. The pdf, however, becomes more symmetric for $\tau \to \infty$.

In these two theoretical scenarios, it already becomes obvious that the joint delay Doppler pdf and the delay-dependent Doppler pdfs depend on the orientation of the velocity vectors of the cars. If two vehicles drive on the street, the orientation of the velocity vector with respect to the semi-major axis can quickly change. This orientation change directly affects the composition of $p(t;\tau,\nu)$. If cars drive behind each other with constant velocity as cars do on highways, the scenario almost becomes stationary and the channel does not change much. If two cars, however, drive in opposite directions, the channel is highly time-variant. The joint pdf $p(t;\tau,\nu)$ changes within a very short amount of time and requires the proposed non-stationary model.

The channel model naturally extends the existing Doppler pdfs to the time-variant case. The Doppler pdfs are readily determined for an arbitrary time t. The proof in Appendix D is also valid for cars driving in opposite directions, if the speed is different.

The results of the theoretical derivations in this thesis are subsequently validated by measurement data. A purely theoretical model would have to be discarded, if it doesn't agree with the real-world propagation channel. In the following section, the results obtained from the theoretical expressions are compared with the measurement data obtained in the campaign described in Chapter 3.

4.4 Validation

In this section, the measured estimated spreading functions are compared with scaled and averaged pdfs that are calculated by the V2V model in order to validate our theoretical claims. The scaling is explained later in this section. Since the theoret-

ical modeling took place in the delay Doppler domain, the measured transfer functions are transformed into the delay Doppler domain as well. Therefore, we firstly Fourier transform the transfer function into the CIR and then take $N_\mathrm{b} = 1024$ measured snapshots of the CIR and apply a Fourier transform again. The application of the Fourier transform means that the signal is averaged over $\Delta t = N_\mathrm{b} T_\mathrm{g} = 1.05\,\mathrm{s}$. In contrast to that, the evaluated pdf gives an instantaneous stochastic dependency between delay and Doppler. To be able to compare measured estimated spreading functions with the theoretically derived pdfs, we therefore consider a linear combination of the instantaneous delay Doppler pdfs over the same time interval Δt used for computing the estimated spreading function $\hat{s}[t^*; m, k]$. The resulting temporal mixture is computed as

$$\bar{p}(t^*; \tau, \nu) = \sum_{i=1}^{N_\mathrm{b}} w_i p(t_i; \tau, \nu)\,, \tag{4.24}$$

with N_b being the number of pdfs and w_i being the combination weights chosen so that $\sum_i w_i = 1$. The number N_b of the pdfs thus corresponds to the number of snapshots that are used to calculate the estimated spreading function. A good agreement between the scaled and averaged pdf and the power of the normalized estimated spreading function is achieved by distributing the weights equally such that $w_i = 1/N_\mathrm{b}\ \forall i$, i.e., the pdf is simply averaged over time. Additionally, $\bar{p}(t^*; \tau, \nu)$ is scaled and the distribution of the delay $p(\tau)$ is determined by an exponential path loss model with an estimated path loss coefficient for the scattering, which is determined with a simple least squares algorithm.

The geometric scenario that is used in the previous sections has to be adapted to the measurements. For the measurement scenario, the assumption that scattering occurs all over the ground is unrealistic. Therefore, two additional assumptions on the scattering are made: The penetration depth next to the road is finite and the smooth surface of the road does not cause scattering. The geometric setup is shown in Fig. 4.8. This setup is similar to the one in [AP11, CSB13, KTC+09b], where the scattering occurs in two rectangles next to the street.

Since the scattering does not occur on the whole delay ellipses anymore, the equations for the delay-dependent Doppler pdfs have to be adapted as well, especially the calculation of (4.22). In the following, it is shown how (4.22) has to be changed to account for the intervals of zero support.

Fig. 4.8 shows that only certain segments of the ellipse lie inside the scattering belt for a given delay. In order to obtain the correct Doppler pdf only these segments have to be accounted for. Four ellipse segments that lie inside the scattering belts can occur at most.

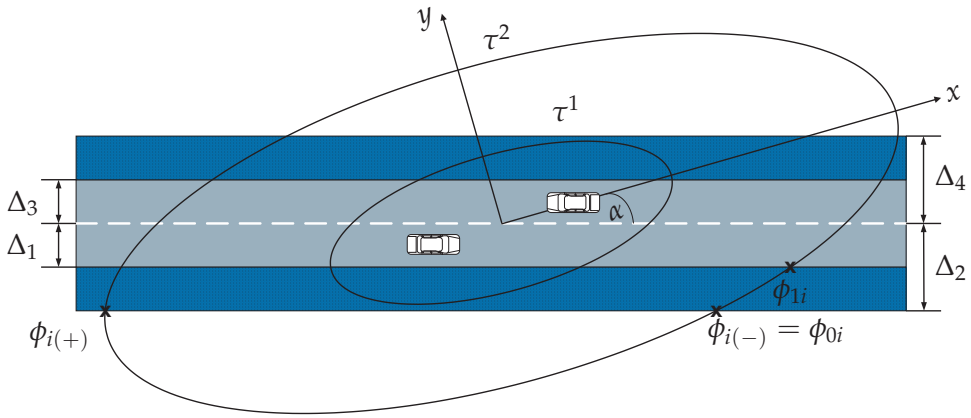

Figure 4.8. *Geometry for a finite scatterer distribution with vehicles driving in different directions on a two lane road.*

Each ellipse segment is characterized by two intersection points: ϕ_{0i} and ϕ_{1i}. They correspond to the start and the end of the ith segment, $i = \{1, \ldots, 4\}$. The intersection points are the intersections of the ellipse with the straight border lines of the scattering belts. The intersection points are calculated as follows: Consider a straight line as border line of the scattering belt. The equation for the border lines is given by

$$y = -x \tan \alpha \pm \frac{\Delta_i}{\cos \alpha}, \tag{4.25}$$

where the subscript i denotes one of 4 lines identifying the borders of the scattering belts. The "+" sign is used for Δ_1 and Δ_2, whereas the "−" sign is used for Δ_3 and Δ_4. To obtain the intersection points the parametric ellipse from (4.16) has to be inserted into (4.25). We get

$$b_\tau \sin \phi = -a_\tau \tan(\alpha) \cos(\phi) \pm \frac{\Delta_i}{\cos \alpha}. \tag{4.26}$$

Let us define

$$g_\tau = -a_\tau \tan \alpha, \quad \text{and} \quad k_i = \pm \frac{\Delta_i}{\cos \alpha}, \tag{4.27}$$

where g_τ is the slope of the line describing the scattering belt and k_i is the corresponding intercept. Solving (4.26) for the parameter ϕ results in two intersection points given by

$$\phi_{i(+),(-)} = 2 \arctan \left(\frac{b_\tau^2 \pm \sqrt{b_\tau^2 - k_i^2 + g_\tau^2}}{(k_i - g_\tau)} \right). \tag{4.28}$$

The two solutions $\phi_{i(+)}$, $\phi_{i(-)}$ provide us either the starting point ϕ_{0i}, or the end point ϕ_{1i} of the ellipse segment, depending on the geometry and the chosen bor-

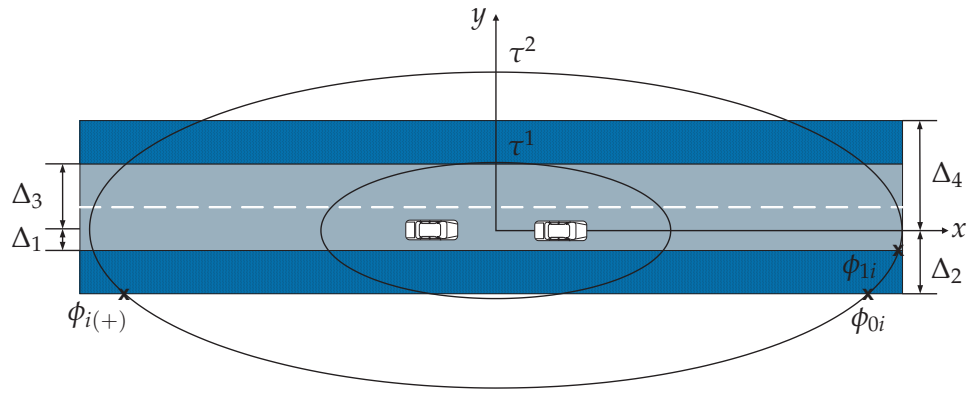

Figure 4.9. *Geometry for a finite scatterer distribution with vehicles driving in the same direction on a two lane road.*

der line of the scattering belt. Once starting and end point ϕ_{0i} and ϕ_{1i} have been determined for all 4 segments, the pdf is computed as follows:

$$p(\phi|\tau) = \begin{cases} \frac{\sqrt{1-\epsilon_\tau^2 \cos^2 \phi}}{\sum_{i=1}^{4} \int_{\phi_{0i}}^{\phi_{1i}} \sqrt{1-\epsilon_\tau^2 \cos^2 \zeta}\, \mathrm{d}\zeta} & \phi \in \cup_{i=1}^{4} [\phi_{0i}, \phi_{1i}] \\ 0 & \text{elsewhere}\,. \end{cases} \tag{4.29}$$

It is possible to have fewer than 4 ellipse segments depending on the size of the ellipse, see Fig. 4.9 for τ^1. In this case the summation in (4.29) has to be adjusted to include only those segments that intersect with the scattering belts. With (4.29) it is possible to determine the delay-dependent Doppler pdf $p(t;\nu|\tau)$ for scatterers that are spatially contained in a rectangular area.

In order to compare the theoretical results with the measurement results, three different scenarios numbered from III to V are used. The actual values for distance and speed are extracted from the on-board GPS receivers that were used during the measurement campaign. The geometric setup of the road and scattering belts is extracted from a map. The carrier frequency remains at $f_\mathrm{c} = 5.2\,\mathrm{GHz}$ and the power of the estimated spreading function is normalized by the square root of the transmit power P_t, so that the path loss including the antenna gains is shown, i.e., $20\log_{10}\left(|\hat{s}[t^*, m, k]|/\sqrt{P_\mathrm{t}}\right)$. The remaining parameters for the three scenarios are summarized below [WFZ14]:

- Scenario III: Two vehicles drive behind each other on the same lane in the same direction and with the same speed. The transmitter is at position $\mathbf{x}_{\mathrm{t}0} = [-20, 0]^\mathrm{T}\mathrm{m}$ with velocity vector $\mathbf{v}_\mathrm{t} = [30, 0]^\mathrm{T}\mathrm{km/h}$. The receiver is at position $\mathbf{x}_{\mathrm{r}0} = [20, 0]^\mathrm{T}\mathrm{m}$ with velocity vector $\mathbf{v}_\mathrm{r} = [30, 0]^\mathrm{T}\mathrm{km/h}$. The parameters for the scattering belts are $\Delta_1 = 1.875\,\mathrm{m}$, $\Delta_2 = 9.375\,\mathrm{m}$, $\Delta_3 = 5.625\,\mathrm{m}$ and $\Delta_4 = 13.125\,\mathrm{m}$, where Δ_1 is the distance from the middle of the right lane to the beginning of the right

scattering belt, Δ_2 is the distance from the middle of the right lane to the end of the right scattering belt, Δ_3 is the distance from the middle of the right lane to the beginning of the left scattering belt, and Δ_4 is the distance from the middle of the right lane to the end of the left scattering belt, see Fig. 4.9.

- Scenario IV: Two vehicles approach each other on different lanes and with similar speed. The transmitter is at position $\mathbf{x}_{t0} = [-102, 0]^T$m with velocity vector $\mathbf{v}_t = [31, -0.6]^T$km/h. The receiver is at position $\mathbf{x}_{r0} = [102, 0]^T$m with velocity vector $\mathbf{v}_r = [-30, 0.6]^T$km/h. The LOS distance varies in the interval $d \in [189, 204]$ m. The parameters for the scattering belts are $\Delta_1 = 3.75$ m, $\Delta_2 = 11.25$ m, $\Delta_3 = 3.75$ m, and $\Delta_4 = 11.25$ m, where Δ_1 is the distance from the middle of the road to the beginning of the right scattering belt, Δ_2 is the distance from the middle of the road to the end of the right scattering belt, Δ_3 is the distance from the middle of the road to the beginning of the left scattering belt, and Δ_4 is the distance from the middle of the road to the end of the left scattering belt, see Fig. 4.8.

- Scenario V: Two vehicles drive away from each other on different lanes and with similar speed. The transmitter is at position $\mathbf{x}_{t0} = [93, 0]^T$m with velocity vector $\mathbf{v}_t = [30, 0.6]^T$km/h. The receiver is at position $\mathbf{x}_{r0} = [-93, 0]^T$m with velocity vector $\mathbf{v}_r = [-28, -0.5]^T$km/h. The parameters for the scattering belts are $\Delta_1 = 3.75$ m, $\Delta_2 = 11.25$ m, $\Delta_3 = 3.75$ m, and $\Delta_4 = 11.25$ m and the definitions of the Δ_i are the same as in Scenario IV.

As stated before, the joint delay Doppler pdf is averaged over $\Delta t = 1.05$ s, which explains the interval for the LOS distance in Scenario IV an V. Since the cars drive behind each other with a constant distance in Scenario III, the LOS distance does not change and the averaging has no effect on the pdf, so that we get $\bar{p}(t^*; \tau, \nu) \approx p(t^*; \tau, \nu)$.

Scenario III: The normalized estimated spreading function and the scaled and averaged joint delay Doppler pdf are shown in Fig. 4.10a and Fig. 4.10b, respectively. In comparison to Scenario I only a fraction of the scattering power is visible in the delay Doppler domain. Less scattering is visible due to fact that the scattering occurs only in small scattering belts to the left and right of the road. Since the spatial dimensions are related to the delay and Doppler frequency in a non-linear manner, the scattering belts lead to curved surfaces in the delay and Doppler domain. It is quasi cut out from the pdf in Scenario I. Because both cars drive with the same velocity, the LOS occurs at $\nu = 0$ Hz with a delay of $\tau = 133$ ns. The scattering occurs directly after the LOS, since the tree trunks that scatter the signal are close to the road. In Fig. 4.10a it can be seen that the power of the LOS gets spread to other de-

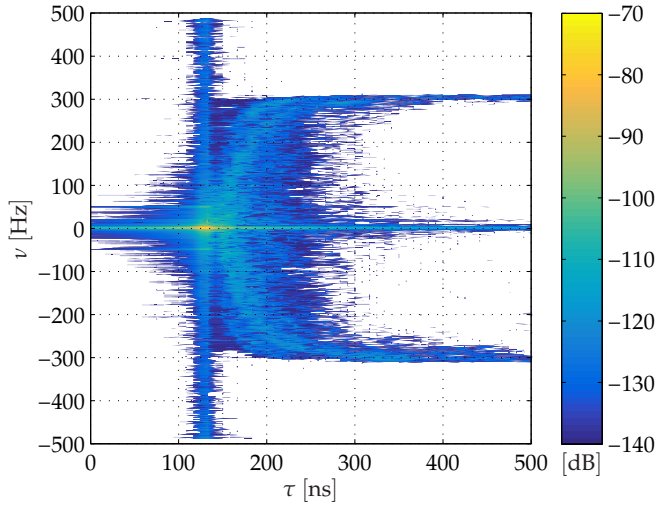

(a) *Normalized estimated spreading function in logarithmic domain:* $20\log_{10}\left(|\hat{s}[t^*;m,k]|/\sqrt{P_\mathrm{t}}\right)$.

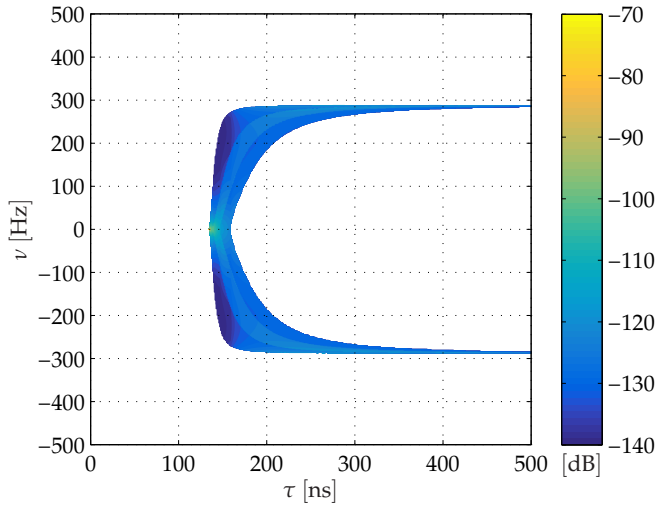

(b) *Scaled and averaged joint delay Doppler pdf in logarithmic domain:* $10\log_{10}\left(\bar{p}(t^*;\tau,\nu)\right)$.

Figure 4.10. *Scenario III: Vehicles at positions* $\mathbf{x}_{\mathrm{t}0} = -\mathbf{x}_{\mathrm{r}0} = [-20,0]^{\mathrm{T}}\mathrm{m}$ *with velocity vectors* $\mathbf{v}_\mathrm{t} = \mathbf{v}_\mathrm{r} = [30,0]^{\mathrm{T}}\mathrm{km/h}$.

lays and Doppler frequencies due to the band-limitation and Fourier transform. The scattering in the theoretical results in Fig. 4.10b shows a curved line for the power of the scatterers close to the LOS.

For small delays the delay ellipse intersects with the scattering belt, which corresponds to the one contiguous ellipse segment on the right side of the road and then continues with one contiguous segment on the left side of the road. The contiguous ellipse segments mean for the delay-dependent Doppler spectrum that only one

contiguous block of spectrum exists, which can clearly be seen both in the estimated spreading function and in the joint delay Doppler pdf. As the delay ellipse grows it splits up in four segments and results in a split of the delay-dependent Doppler frequency into two strips at $\tau = 159\,\text{ns}$. Since the delay ellipse is almost symmetric to the scattering belts, the Doppler frequencies caused by the left and right side of the road overlap. This effect can be noticed both in the estimated spreading function and in the pdf by the slightly different color in the middle of the strips, which means higher power or higher probability, respectively.

For increasing delay the Doppler frequency asymptotically reaches $\nu \to (\|\mathbf{v}_\text{t}\| + \|\mathbf{v}_\text{r}\|) f_\text{c}/c$. This means the signal "sees" the scattering belts as two points in front and behind the cars for long delays, which corresponds to the geometric setup. As long as the cars drive behind each other with constant velocity, the channel does not change. This clearly shows once more that two cars driving behind each other can be adequately described by WSSUS models. However, the delay-dependent Doppler pdfs are very different from the Jakes or Gaussian pdf. The geometry has a huge influence on the shape of the Doppler pdfs.

Scenario IV: The normalized estimated spreading function and the scaled and averaged joint delay Doppler pdf are shown in Fig. 4.11a and Fig. 4.11b, respectively. It is remarkable that the joint delay Doppler pdf completely differs from Scenario III. This difference is due to the different distribution of the Doppler frequency on the ground shown in Fig. 4.6. Since the cars drive in opposite directions, there are almost no negative Doppler frequencies. The highest Doppler frequencies occur close to the LOS, since the distance close to the LOS changes fastest. Furthermore, the averaging effect is visible in both the estimated spreading function and the joint delay Doppler pdf. The LOS should only consist of a single point, however, the LOS is spread in delay direction. The distance between the cars changes for $\Delta t = 1.05\,\text{s}$ by 15 m which corresponds to $\Delta\tau = 50\,\text{ns}$.

As in Scenario III, the largest Doppler spread occurs for scatterers close to the LOS. However, the Doppler frequencies are only positive. Since the ellipse and the scattering belts are in a completely symmetric setup, only one contiguous strip of Doppler frequencies is created. The width of the delay-dependent pdf decreases for increasing delay and finally splits up into two non-contiguous strips. The theoretical model can explain this split very well. Since the geometric setup is symmetric, the split is due to the slightly different velocities of transmitter and receiver. The shape of the scattering in the delay Doppler domain is very similar for both the pdf and the estimated spreading function. Therefore, Scenario IV supports the validity of the proposed model as well.

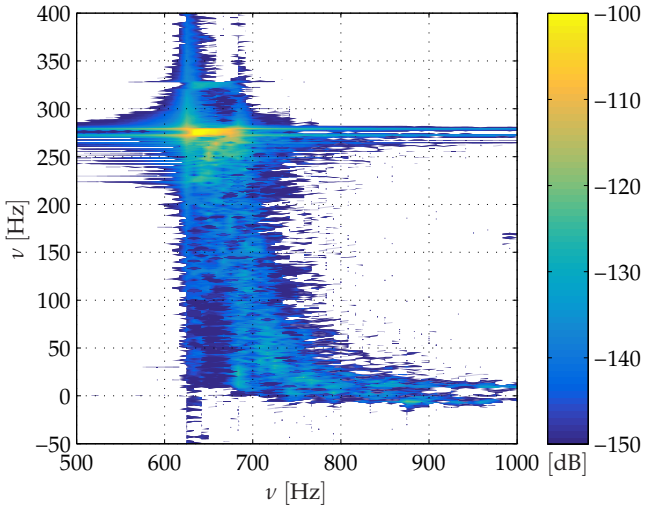

(a) *Normalized estimated spreading function in logarithmic domain:* $20\log_{10}\left(|\hat{s}[t^*;m,k]|/\sqrt{P_\mathrm{t}}\right)$.

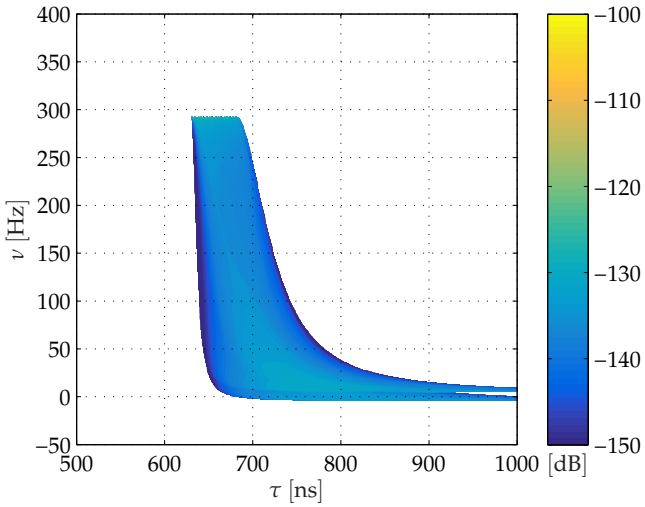

(b) *Scaled and averaged joint delay Doppler pdf in logarithmic domain:* $10\log_{10}\left(\bar{p}(t^*;\tau,\nu)\right)$.

Figure 4.11. *Scenario IV: vehicles at positions* $\mathbf{x}_{\mathrm{t}0} = -\mathbf{x}_{\mathrm{r}0} = [-102,0]^{\mathrm{T}}\mathrm{m}$ *with velocity vectors* $\mathbf{v}_\mathrm{t} = [31,-0.6]^{\mathrm{T}}\mathrm{km/h}$ *and* $\mathbf{v}_\mathrm{r} = [-30,0.6]^{\mathrm{T}}\mathrm{km/h}$.

Scenario V: The normalized estimated spreading function and the scaled and averaged joint delay Doppler pdf are shown in Fig. 4.12a and Fig. 4.12b, respectively. In the figures the scattering power in the delay Doppler domain is presented for cars driving away from each other. The scattering power is almost a mirror image of Scenario IV, since the velocity vectors change their sign and the magnitudes are approximately the same. The distance of the vehicles is similar as in Scenario IV. Due to the opposite orientation, the Doppler frequencies become negative. Thus,

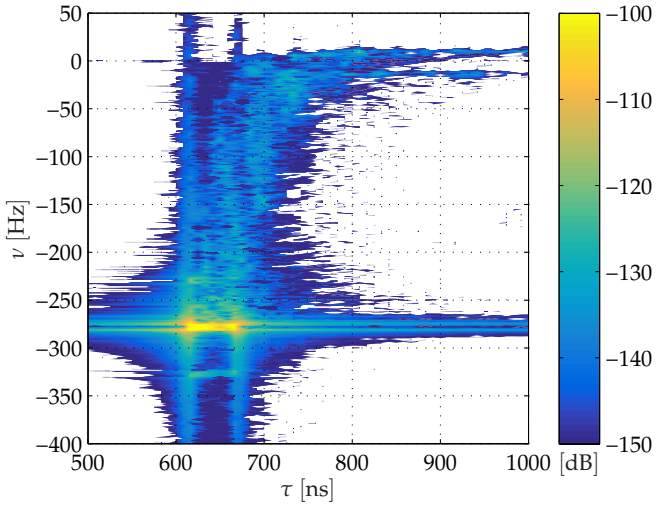

(a) *Normalized estimated spreading function in logarithmic domain:* $20\log_{10}\left(|\hat{s}[t^*;m,k]|/\sqrt{P_\mathrm{t}}\right)$.

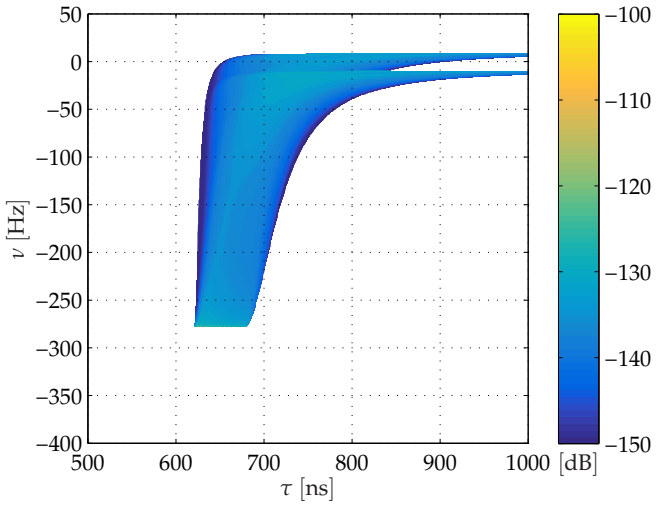

(b) *Scaled and averaged joint delay Doppler pdf in logarithmic domain:* $10\log_{10}\left(\bar{p}(t^*;\tau,\nu)\right)$.

Figure 4.12. *Scenario V: Vehicles at positions* $\mathbf{x}_{\mathrm{t}0} = -\mathbf{x}_{\mathrm{r}0} = [93,0]^{\mathrm{T}}\mathrm{m}$ *with velocity vectors* $\mathbf{v}_\mathrm{t} = [30,0.6]^{\mathrm{T}}\mathrm{km/h}$ *and* $\mathbf{v}_\mathrm{r} = [-28,-0.5]^{\mathrm{T}}\mathrm{km/h}$.

the scattering in the channel changes from positive to negative Doppler frequencies in a very short amount of time, when the vehicles pass each other. For these types of scenarios the channel is clearly non-stationary and such scenarios must not be described by a WSSUS channel models.

The estimated spreading function in Fig. 4.12a and the joint delay Doppler pdf in Fig. 4.12b show one large strip of scattering power for small delays and then the strip splits up into two strips at about $\tau = 850\,\mathrm{ns}$. The split up is more clearly

visible in this particular scenario compared to Scenario IV, since the difference in velocity of both cars is slightly larger. The fact that there are only negative frequencies is directly related to the orientation of the velocity vectors of both transmitter and receiver. In this case the velocity vectors of transmitter and receiver cancel mostly out in the calculation of the Doppler frequency for far away scatterers. Only for the scatterers in between the two vehicles, where the delay is small, the Doppler becomes negative. Similar results as shown in Scenario IV and V are found in [PWK+08, ZWGL12].

4.5 Ellipsoidal Coordinates

All calculations have been conducted in a Cartesian coordinate system. A coordinate system is used to place objects in space and obtain relations in form of algebraic equations. The most commonly used system is the Cartesian coordinate system. It is an orthonormal coordinate system, with the peculiarity that the basis vectors do not depend on position. Therefore, only the components of a vector change and not its basis, when considered at different locations. Thus, differential operators are easy to apply in Cartesian coordinates.

However, as shown in the previous chapters, the expressions in Cartesian coordinates become cumbersome and numeric algorithms have to be used to calculate the parameter ϕ for a certain Doppler frequency. The numeric calculations in turn take more time than symbolic solutions for polynomial equations.

In order to make the calculations easier and faster, other coordinate systems which are adapted to the geometry of the problem can be used. One example is the spherical coordinate system that is used for calculations of the electric field around a point charge or the Schwarzschild solutions for the Einstein field equations. For the M2M channel there is also a preferred coordinate system. Since the delay-dependent Doppler frequency is of interest, one particular coordinate system clearly simplifies the description: The coordinate system is called prolate spheroidal coordinate system (PSCS) and belongs to the family of orthonormal coordinate systems. That means that the basis vectors are of unit length and perpendicular to each other at every location in space. The orientation of the basis vectors can change however. The coordinate surfaces are described by ellipsoids, two-sheeted hyperboloids and half-planes, see Fig. 4.13. The ellipsoidal coordinate surface make it particularly suitable for the description of M2M channels, since the delay is represented by ellipsoids. This means that the delay τ is represented by a single coordinate in the PSCS. Thus, the symmetry of the delay is exploited with this kind of coordinate system.

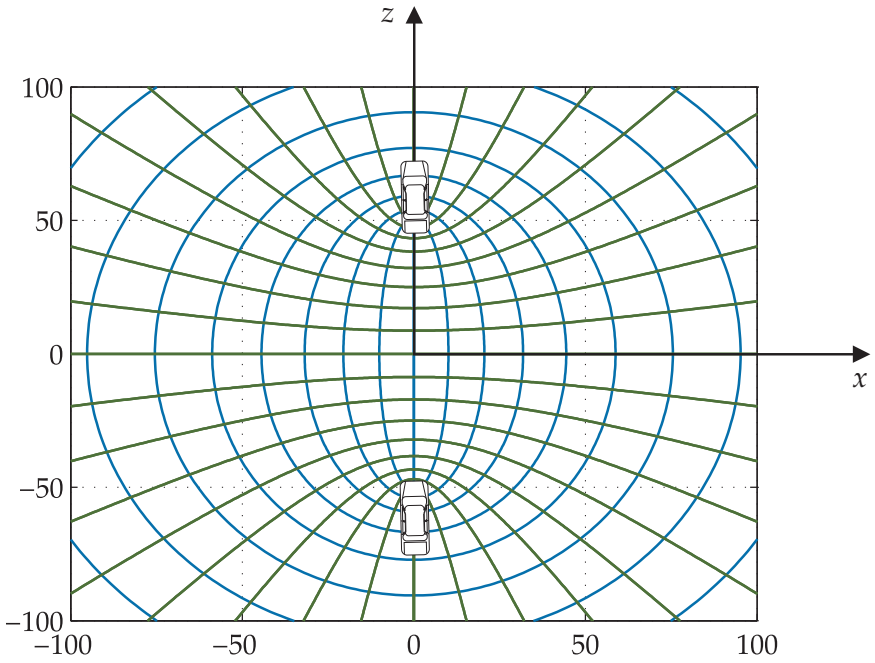

Figure 4.13. *Lines of constant coordinates ξ (blue) and η (green) with the transmitter and receiver in the foci of the ellipses and hyperbolas.*

In the following, we introduce the reader to the coordinate transformation from the Cartesian coordinate system to the PSCS and rewrite the equations of delay, Doppler and pdfs. Furthermore, the delay-dependent characteristic function is introduced in order to calculate the mean Doppler and Doppler spread for the delay-dependent Doppler pdfs as shown in [WSF15].

4.5.1 Coordinate Transformation

The general conversion between the Cartesian coordinate system (x, y, z) and the prolate spheroidal coordinates (ξ, η, ϑ) is explained including the conversion of the differential operator ∇. The conversion is done in 3D coordinates to be able to use the derivations also for the A2A channel later. The conversion of the coordinates is achieved by using the following transformation [BSMM07]:

$$\begin{aligned} x &= L_\mathrm{f}\sqrt{(\xi^2-1)(1-\eta^2)}\cos\vartheta \\ y &= L_\mathrm{f}\sqrt{(\xi^2-1)(1-\eta^2)}\sin\vartheta \\ z &= \qquad\qquad L_\mathrm{f}\xi\eta\,, \end{aligned} \tag{4.30}$$

where L_f is the focus distance, and $\xi \in [1, \infty)$, $\eta \in [-1, 1]$, and $\vartheta \in [0, 2\pi)$ are the new coordinates in the PSCS. Note that the z-axis is aligned with the vehicles and

not the x-axis as before. This alignment is due to the coordinate transformation rules in the literature provided in (4.30).

4.5.2 Delay and Doppler in the PSCS

Using (4.30), the summands of (4.6) can be computed as $d_{\mathrm{t}}(\xi,\eta) = (\xi+\eta)\,L_{\mathrm{f}}$ and $d_{\mathrm{r}}(\xi,\eta) = (\xi-\eta)\,L_{\mathrm{f}}$ respectively. Thus, the total distance $d_{\mathrm{sc}}(\mathbf{x},t)$ in (4.6) can be expressed as $d_{\mathrm{sc}}(\xi,\eta) = 2\xi L_{\mathrm{f}}$, i.e, it is given by the ξ-coordinate and the focus distance L_{f}. The corresponding propagation delay can then be expressed as $\tau = 2\xi L_{\mathrm{f}}/c$. The parameter η describes the hyperboloid, which means that the difference of the two path lengths between transmitter and scatterer and between scatterer and receiver is constant. This path difference, however, cannot be directly linked to the description of delay or Doppler frequency. To compute the Doppler frequency, (4.13) needs to be evaluated in the PSCS. This evaluation requires transforming the gradient operators into the new coordinate system.

In the PSCS, the gradient of a scalar function Ψ can be computed as [BSMM07]

$$\nabla\Psi = \frac{1}{h_\xi}\frac{\partial\Psi}{\partial\xi}\mathbf{e}_\xi + \frac{1}{h_\eta}\frac{\partial\Psi}{\partial\xi}\mathbf{e}_\eta + \frac{1}{h_\vartheta}\frac{\partial\Psi}{\partial\vartheta}\mathbf{e}_\vartheta\,, \tag{4.31}$$

where $\mathbf{e}_\xi$, $\mathbf{e}_\eta$, and $\mathbf{e}_\vartheta$ are the unit basis vectors of the PSCS, and h_ξ, h_η, and h_ϑ are the corresponding scale factors. The scale factors are needed to be able to measure distances and angles in a curvilinear coordinate system. They are defined as the square root of the diagonal of the metric tensor. For the PSCS the scale factors are given by

$$h_\xi = L_{\mathrm{f}}\sqrt{\frac{(\xi^2-\eta^2)}{(\xi^2-1)}}\,,\; h_\eta = L_{\mathrm{f}}\sqrt{\frac{(\xi^2-\eta^2)}{(1-\eta^2)}}\,,\; h_\vartheta = L_{\mathrm{f}}\sqrt{(\xi^2-1)(1-\eta^2)}\,. \tag{4.32}$$

The basis vectors $\mathbf{e}_\xi$, $\mathbf{e}_\eta$, and $\mathbf{e}_\vartheta$ of the PSCS are obtained by transforming the Cartesian basis vectors $\mathbf{e}_x$, $\mathbf{e}_y$, and $\mathbf{e}_z$. In contrast to the Cartesian basis vectors, which are not dependent on the location in the coordinate system, the basis vectors change their direction at different locations in a curvilinear coordinate system. This change needs to be taken into account for any calculation in the new coordinate system. The basis vectors in the PSCS are obtained by

$$\mathbf{e}_\beta = \frac{\partial x}{\partial\beta}\frac{\mathbf{e}_x}{h_\beta} + \frac{\partial y}{\partial\beta}\frac{\mathbf{e}_y}{h_\beta} + \frac{\partial z}{\partial\beta}\frac{\mathbf{e}_z}{h_\beta}\,, \tag{4.33}$$

where $\beta \in \{\xi,\eta,\vartheta\}$. The scale factors h_β normalize the basis vectors to unit length.

In order to evaluate the Doppler frequency, the dot product between the gradient (4.31) of the distance (4.6) and the velocity vectors $\mathbf{v}_{\mathrm{t}}$ and $\mathbf{v}_{\mathrm{r}}$ of the transmitter and

the receiver needs to be calculated. Since the velocities of transmitter and receiver are described by a constant vector field in Cartesian coordinates, the transformation will only affect the basis vectors. To clarify this, we exemplarily convert the velocity vector field $\mathbf{v}(\mathbf{x})$, which is constant and only has a z-component, see Fig. 4.13. This corresponds to the scenario presented in Section 4.5.3. We readily obtain

$$\mathbf{v} = v^z \mathbf{e}_z = v^z \left(\eta \sqrt{\frac{\xi^2 - 1}{\xi^2 - \eta^2}} \mathbf{e}_\xi + \xi \sqrt{\frac{1 - \eta^2}{\xi^2 - \eta^2}} \mathbf{e}_\eta \right) . \tag{4.34}$$

Finally, the Doppler frequency in the PSCS is given by

$$\begin{aligned} \nu(\eta, \xi, \vartheta) = & \frac{\xi^2 - 1}{\xi^2 - \eta^2} \frac{f_c}{c} \left(\frac{\xi \left(1 - \eta^2\right)}{\sqrt{\left(\xi^2 - 1\right)\left(1 - \eta^2\right)}} \left(v_t^x \cos\vartheta + v_t^y \sin\vartheta \right) + \eta v_t^z \right) \\ & - \frac{1 - \eta^2}{\xi^2 - \eta^2} \frac{f_c}{c} \left(\frac{\eta \left(\xi^2 - 1\right)}{\sqrt{\left(\xi^2 - 1\right)\left(1 - \eta^2\right)}} \left(v_t^x \cos\vartheta + v_t^y \sin\vartheta \right) - \xi v_t^z \right) \\ & + \frac{\xi^2 - 1}{\xi^2 - \eta^2} \frac{f_c}{c} \left(\frac{\xi \left(1 - \eta^2\right)}{\sqrt{\left(\xi^2 - 1\right)\left(1 - \eta^2\right)}} \left(v_r^x \cos\vartheta + v_r^y \sin\vartheta \right) + \eta v_r^z \right) \\ & + \frac{1 - \eta^2}{\xi^2 - \eta^2} \frac{f_c}{c} \left(\frac{\eta \left(\xi^2 - 1\right)}{\sqrt{\left(\xi^2 - 1\right)\left(1 - \eta^2\right)}} \left(v_r^x \cos\vartheta + v_r^y \sin\vartheta \right) - \xi v_r^z \right) , \end{aligned} \tag{4.35}$$

where v_t^x, v_t^y v_t^z, v_r^x, v_r^y, and v_r^z are the velocity components in Cartesian coordinates of transmitter and receiver, respectively.

Let us restrict ourselves to a 2D scenario and assume no vertical velocity component, i.e., $\vartheta \in \{0, \pi\}$, which are the two half-planes and $v_t^y = v_r^y = 0$. This restriction corresponds to two cars driving on a road with arbitrary velocity vectors. Hereby, (4.35) simplifies, and ν becomes a rational polynomial function of ξ and η. In Cartesian coordinates an equivalent expression is significantly more involved, see Appendix B.2. The delay-dependent Doppler frequency is given by $\nu(\eta|\xi)$, since $\tau \propto \xi$. With such a relation the delay-dependent Doppler pdf $p(\nu|\xi)$ can be computed.

Therefore, the parameter ξ is fixed, i.e., a certain delay ellipse is selected. Then consider the parametric angle $\phi \in [0, \pi)$ of the ellipse segment laying in the half-plane $\vartheta = 0$. Such an ellipse segment is parametrized by $\mathbf{x}(\phi) = [a_\xi \cos\phi, b_\xi \sin\phi]^{\mathrm{T}}$. Assuming an equal distribution of scatterers on the ellipse, the conditional pdf $p(\phi|\xi)$ can be computed as [NA98] and [WSF14a]

$$p(\phi|\xi) = \frac{1}{2\mathrm{E}(\epsilon_\xi)} \sqrt{1 - \epsilon_\xi^2 \cos^2\phi} , \tag{4.36}$$

where $\mathrm{E}(\epsilon_\xi)$ is the complete elliptic integral of the second kind, ϵ_ξ is the delay-dependent eccentricity of the ellipse. Using the fact that $\phi = \arccos(\eta)$ and applying the rules of probability density transformations [PP02] we compute

$$p(\eta|\xi) = \left|\frac{\partial\phi}{\partial\eta}\right| p(\phi|\xi)\Big|_{\phi'=\arccos(\eta)} = \frac{\sqrt{1-\left(\epsilon_\xi\eta\right)^2}}{2\mathrm{E}(\epsilon_\xi)\sqrt{1-\eta^2}}\,, \tag{4.37}$$

where the fact that $\frac{\partial\phi}{\partial\eta} = (1-\eta^2)^{-\frac{1}{2}}$ is used.

For a fixed ξ we compute the conditional Doppler pdf $p(\nu|\xi)$ using (4.35). Following the same steps as in [WSF14a], we can determine the Doppler pdf by transforming the pdf (4.37)

$$p(\nu|\xi) = \sum_{\eta'\in\left\{\mathcal{F}^{-1}(\nu)\right\}} \left|\frac{\partial\eta'}{\partial\nu}\right| p(\eta'|\xi)\,, \tag{4.38}$$

where $\mathcal{F}^{-1}(\nu)$ is the inverse relation of $\nu(\eta,\xi,\phi)$. Note that there can be multiple values η for one Doppler frequency ν, which is taken into account by the sum in (4.38). Furthermore, in order to calculate the Doppler pdf, the ellipse segments in both half-planes, i.e., $\vartheta = \{0,\pi\}$ have to be taken into account. The joint delay Doppler pdf is calculated from (4.38) as $p(\tau,\nu) = p(\tau)p(\nu|\tau)$, where the relation $\tau = 2\xi L_\mathrm{f}/c$ is used and we assume suitable delay density function $p(\tau)$.

In general, the computation of (4.38) might be quite complex as it requires inverting (4.35). However, in the discussed cases these computations simplify. If the velocity vectors of the vehicles only have components in the x-z-plane and the cars move in the x-z-plane, the trigonometric terms in (4.35) disappear, and the Doppler frequency becomes a rational function of the delay. In one half-plane the parameter ϑ is constant, which we assume in the following. As compared to the equivalent scenario considered in Cartesian coordinates, the numerical analysis of the resulting expression in the PSCS is simpler. The simpler expressions will translate into a large gain in computational time.

4.5.3 Characteristic Function

The characteristic function represents another stochastic description method for the V2V channel, if the pdf is available. The characteristic function is calculated by an inverse Fourier transform of $p(\nu|\xi)$. In Cartesian coordinates the transform could not be calculated analytically. Furthermore, even writing down the expression to transform would be cumbersome. However, with the help of the PSCS this task becomes relatively compact. For the characteristic function given in the PSCS, the characteristic function becomes

$$\Phi(u|\xi) = \int_{-\infty}^{\infty} p(\nu|\xi)\exp\left(\mathrm{j}2\pi\nu u\right)\mathrm{d}\nu = \int_{-1}^{1} p(\eta|\xi)\exp\left(\mathrm{j}2\pi\nu(\eta|\xi)u\right)\mathrm{d}\eta\,, \tag{4.39}$$

using ν from (4.35). The characteristic function is used to generate the moments of the distribution. For non-stationary channels the moments become dependent on the delay τ and time t. The mean Doppler frequency and Doppler spread can readily be calculated as [Pät02]

$$\mu(\xi) = \frac{\dot{\Phi}(0|\xi)}{\mathrm{j}2\pi}, \quad \sigma(\xi) = \frac{\sqrt{\left(\dot{\Phi}(0|\xi)\right)^2 - \ddot{\Phi}(0|\xi)}}{2\pi} \tag{4.40}$$

Typical Doppler spreads of V2V channels can be found in [BZT+14] or [CHBS08].

We use Scenario I and II to calculate the characteristic function $\Phi(u|\xi)$. In those two scenarios the two cars drive either in the same or in opposite directions with the same speed.

In Scenario I the velocity vectors are equal, i.e., $v = v_\mathrm{t}^z = v_\mathrm{r}^z$ and thus the integral simplifies considerably. By inserting the corresponding parameters, (4.39) becomes

$$\Phi(u|\xi) = \int_{-1}^{1} \frac{\sqrt{1-\left(\epsilon_\xi \eta\right)^2}}{2\mathrm{E}(\epsilon_\xi^2)\sqrt{1-\eta^2}} \cos\left(\frac{4\pi(\xi^2-1)\eta v f_\mathrm{c} u}{(\xi^2-\eta^2)c}\right) \mathrm{d}\eta\,, \tag{4.41}$$

where we made use of the fact that the delay-dependent Doppler pdf is symmetric and bounded. Thus, the characteristic function is real, symmetric and infinite. For $\xi \to \infty$, the characteristic function $\Phi(u|\xi)$ in (4.41) asymptotically converges to the zeroth-order Bessel function of the first kind $\mathrm{J}_0(4\pi f_{\mathrm{d,max}} u)$, whose auto-correlation function corresponds to the Jakes spectrum. This result confirms once again that our model is a generalization of the WSSUS models.

Another example of the characteristic function is obtained for Scenario II. By inserting $v = v_\mathrm{t}^z = -v_\mathrm{r}^z$, we obtain

$$\Phi(u|\xi) = \int_{-1}^{1} \frac{\sqrt{1-\left(\epsilon_\xi \eta\right)^2}}{2\mathrm{E}(\epsilon_\xi^2)\sqrt{1-\eta^2}} \exp\left(\mathrm{j}\frac{4\pi(1-\eta^2)\xi v f_\mathrm{c} u}{(\xi^2-\eta^2)c}\right) \mathrm{d}\eta\,, \tag{4.42}$$

with the Doppler pdf being asymmetric. Specifically, it consists only of positive frequencies. Therefore, the characteristic function becomes complex Hermitian.

4.5.4 Theoretical Results

The results for Scenario I and II in the PSCS are explained in the following. The delay range is selected to be $\tau \in [2L_\mathrm{f}/c, 800\,\mathrm{ns}]$, with $L_\mathrm{f} = 50\,\mathrm{m}$. As mentioned before the carrier frequency $f_\mathrm{c} = 5.2\,\mathrm{GHz}$ is used.

Compared to the numerical computations in the Cartesian coordinate system, the calculations of the analytic solutions for the joint delay Doppler pdfs are more

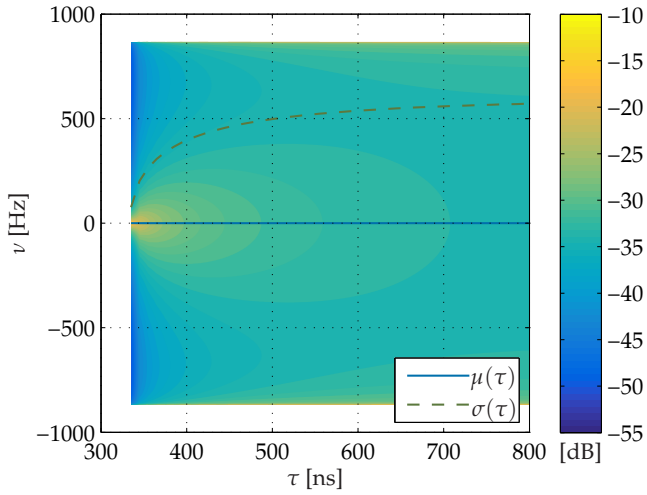

(a) *Joint delay Doppler pdf in logarithmic domain:* $10\log_{10}\left(p(t^*;\tau,\nu)\right)$ *with mean Doppler* $\mu(\tau)$ *and Doppler spread* $\sigma(\tau)$.

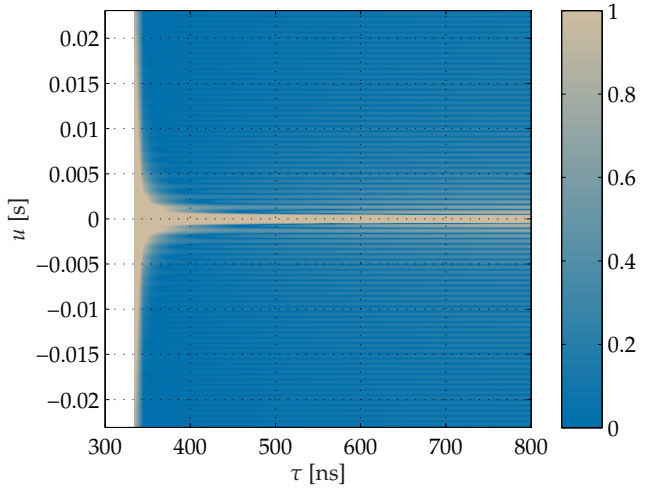

(b) *Magnitude of the characteristic function:* $|\Phi(t^*;\tau,u)|$.

Figure 4.14. *Scenario I: Vehicles at positions* $\mathbf{x}_{\mathrm{t}0} = -\mathbf{x}_{\mathrm{r}0} = [-50, 0]^{\mathrm{T}}\mathrm{m}$ *with velocity vectors* $\mathbf{v}_{\mathrm{t}} = \mathbf{v}_{\mathrm{r}} = [90, 0]^{\mathrm{T}}\mathrm{km/h}$.

than sixty times faster on a standard PC. Furthermore, the expressions of the pdfs are more compact. As mentioned before, one drawback of the new coordinate system is the dependency of the basis vectors on the current location in the coordinate system. If the velocity vectors are not aligned with the major axis of the ellipsoid, the expressions to compute the pdfs become consequently more involved.

Scenario I: Fig. 4.14a displays the joint delay Doppler pdf. The pdf is the same as in Fig. 4.5a, but we additionally show the mean Doppler and Doppler spread. The mean Doppler stays at $\mu(\tau) = 0\,\mathrm{Hz}$, since the delay-dependent Doppler spectra

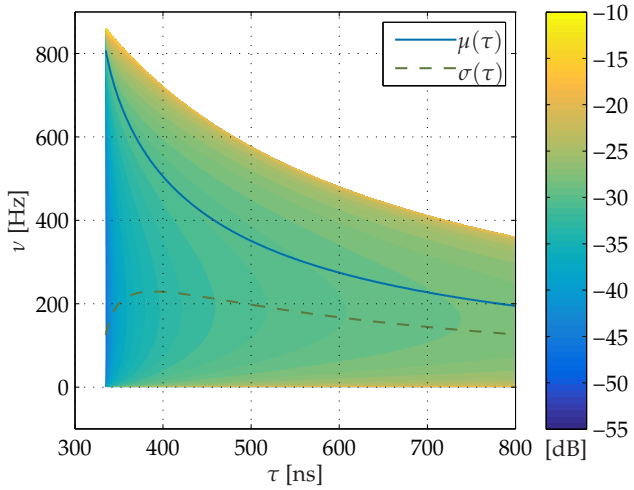

(a) *Joint delay Doppler pdf in logarithmic domain:* $10\log_{10}\left(p(t^*;\tau,\nu)\right)$ *with mean Doppler* $\mu(\tau)$ *and Doppler spread* $\sigma(\tau)$.

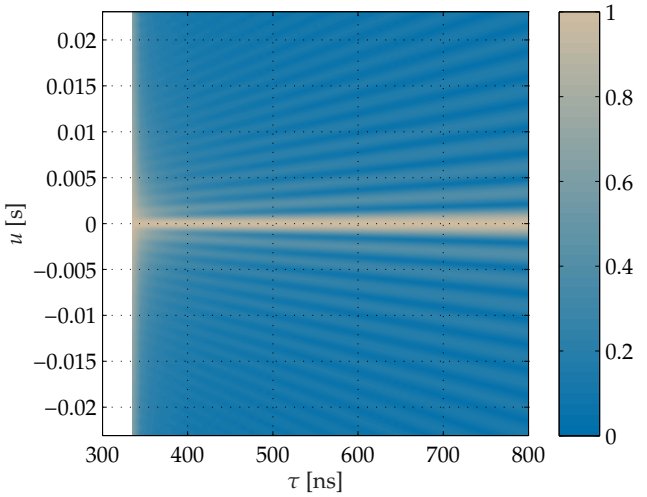

(b) *Magnitude of the characteristic function:* $|\Phi(t^*;\tau,u)|$.

Figure 4.15. *Scenario II: Vehicles at positions* $\mathbf{x}_{t0} = -\mathbf{x}_{r0} = [-50, 0]^T$m *with velocity vectors* $\mathbf{v}_t = -\mathbf{v}_r = [90, 0]^T$km/h.

are symmetric. The Doppler spread $\sigma(\tau)$ increases for increasing delay τ, i.e., the channel becomes more time-variant.

The magnitude of the characteristic function $\Phi(t^*;\tau,u)$ is shown in Fig. 4.14b. Since the delay-dependent Doppler spectra are all symmetric, the characteristic function is a real and symmetric function. For increasing delay the main lobe gets narrower and the side lobe larger. This behavior corresponds to the increasing Doppler spread in Fig. 4.14a. For $\tau \to \infty$, the characteristic function converges

to $\Phi(t^*; u|\tau) \rightarrow \mathrm{J}_0(4 f_{\mathrm{d,max}} u)$, which corresponds to the characteristic function of the Jakes pdf.

Scenario II: Fig. 4.15a shows the joint delay Doppler pdf. The pdf is exactly the same as in Fig. 4.7a. Furthermore, the mean Doppler and Doppler spread are included. For delays close to the LOS the mean Doppler is highest and then decreases, whereas the Doppler spread increases until $\tau = 390\,\mathrm{ns}$ and the decreases. The delay dependence of the two moments is therefore clearly visible. This information can be crucial for the equalization procedure in the receiver.

Note that for asymmetric pdfs the corresponding characteristic function is complex. Thus, in contrast to the scenario where two cars drive behind each other, the resulting characteristic function is complex, see (4.42). However, it can still be treated as a measure of channel coherence. For small delays the width of the main lobe of the characteristic function decreases slightly, which corresponds to a higher Doppler spread and thus higher channel variations. For larger delays the Doppler spread decreases reflecting a higher channel coherence.

The different channel coherence depending on the delay is very interesting, when it comes to the equalization of the channel. It means that the channel taps statistics change at different rate and therefore need to be updated at different times. The taps close to the LOS have to be updated more often than the ones with a large delay. With an unequal coefficient update, the equalization of the channel in the receiver can be conducted more efficiently.

It has been shown that the use of an adequate coordinate system provides polynomial solutions to calculate the joint pdf. Furthermore, it is possible to calculate the characteristic function of the V2V channel. The polynomial solution of the pdf in the PSCS reduces the necessary computation time significantly. The use of this particular coordinate system is advantageous, since one coordinate is directly proportional to the delay and allows an efficient simulation of M2M channels. Since M2M channels are naturally highly time-variant and therefore many realizations of the channel need to be calculated, the PSCS is better suited for that task. Furthermore, the mean Doppler, Doppler spread can be determined by the characteristic function. Mean Doppler and Doppler spread characterize the dependency of the time-variance on the delay. Such a dependence signifies that the coefficients of a channel simulator can be unequally updated depending on the Doppler statistics of the respective tap.

4.6 Algebraic Geometry

As in the previous section, we present another way of calculating the delay-dependent Doppler frequency pdfs without using trigonometric functions. There is a branch of mathematics that studies the shape of geometric objects by means of algebraic equations. The branch is called algebraic geometry [Abh90]. There geometric relations are expressed by fractional polynomials instead of trigonometric functions. A fractional polynomial is much easier to handle for calculus operations like integration and differentiation.

We want to introduce the reader to algebraic geometry with some easy examples. Let us begin with a circle. The trigonometric parametric description of a unit circle is given by

$$\mathbf{x}(\phi) = \begin{bmatrix} \cos\phi \\ \sin\phi \end{bmatrix} . \tag{4.43}$$

If we substitute the parameter ϕ with the substitution $s = \tan(\phi/2)$, we get a polynomial expression in the form of

$$\mathbf{x}(s) = \begin{bmatrix} \frac{1-s^2}{1+s^2} \\ \frac{2s}{1+s^2} \end{bmatrix} , \tag{4.44}$$

where $s \in (-\infty, \infty)$. This particular substitution can be explained in a geometric way. Fix the point $P = [-1, 0]^{\mathrm{T}}$ on the circle. Consider lines that pass through P and intersect the circle in a second point. The slope s of all these lines is given by $y = s(x+1)$. If this equation is put into the implicit equation of the circle $x^2 + y^2 = 1$, we get

$$x^2 + s^2(x+1)^2 = 1 . \tag{4.45}$$

If this equation is solved for x and the stationary solution of $P = [-1, 0]^{\mathrm{T}}$ is discarded, the result presented in (4.44) is obtained. Equation (4.44) does not possess any trigonometric functions anymore, which allows for an easier mathematical treatment. However the point $P = [-1, 0]$ is only reached asymptotically, which is a disadvantage compared to the trigonometric description.

The theory of fractional polynomials can be applied to describe the delay ellipses from the previous sections. In the ellipse equation we substitute the ellipse parameter ϕ in (4.16) by $s = \tan(\phi/2)$ and obtain

$$\mathbf{x}(t^*; s|\tau) = \begin{bmatrix} a_\tau \frac{1-s^2}{1+s^2} \\ b_\tau \frac{2s}{1+s^2} \end{bmatrix} , \tag{4.46}$$

which is a rational expression of the ellipse. $\mathbf{x}(t^*; s|\tau)$ is inserted into the Doppler frequency in (4.13) to obtain the delay-dependent Doppler frequency. The result is shown in Appendix B.3. The Doppler frequency consists only of rational polynomial expressions, which are better suited for the application of the differential operator. The variable substitution is followed by a multiplication with the Jacobian element $|\mathrm{d}\nu/\mathrm{d}s|$, which is needed to equalize the contortion introduced by the new variable s.

If we substitute the Doppler frequency with the new variable s, the pdfs have to be adapted. The delay-dependent distribution of the scatterers on the ellipse $p(\phi|\tau)$ has to be replaced by $p(s|\tau)$ with the same variable substitution of $s = \tan(\phi/2)$. The new distribution becomes

$$p(s|\tau) = \frac{\sqrt{1-\epsilon_\tau^2\left(\frac{1-s^2}{1+s^2}\right)^2}}{4\mathrm{E}(\epsilon_\tau)}\frac{2}{1+s^2} = \frac{\sqrt{1-\epsilon_\tau^2\left(\frac{1-s^2}{1+s^2}\right)^2}}{2\mathrm{E}(\epsilon_\tau)(s^2+1)}, \tag{4.47}$$

where $\mathrm{d}\phi = 2/(1+s^2)\,\mathrm{d}s$ originates from the differentiation due to the variable substitution. The complete elliptic integral of the second kind can therefore be written as

$$\int_{-\infty}^{\infty} \frac{\sqrt{1-\epsilon_\tau^2\left(\frac{1-s^2}{1+s^2}\right)^2}}{2(s^2+1)}\,\mathrm{d}s = \mathrm{E}(\epsilon_\tau)\,, \tag{4.48}$$

which is very different from the usual representation. The result of the indefinite integral is shown in Appendix B.4.

The Doppler frequency pdf is then calculated by

$$p(\nu|\tau) = \sum_{s'\in\left\{\mathcal{F}^{-1}(\nu)\right\}} \frac{p(s'|\tau)}{\left|\frac{\mathrm{d}\nu}{\mathrm{d}s'}\right|}, \tag{4.49}$$

where s' is the solution of all s that results in the same Doppler frequency ν. The solutions s' can be calculated much faster, since the function now consists only of fractional polynomials instead of trigonometric functions. The calculation of the delay-dependent Doppler pdf can thus be performed very efficiently.

Chapter 5

Air-to-Air Channel

In this chapter, the second example of an M2M channel is described. The A2A channel is in many aspects similar to the V2V channel. Therefore, we use the model from the previous chapter. The main difference between the V2V and A2A geometry is the velocity and the altitude of the aircraft. Since the aircraft fly above ground, the aircraft heights relative to the ground have to be included into the model. The elevated antenna position makes it necessary to extend the model from a two-dimensional to a three-dimensional model. The three-dimensional part concerns the geometry of the model. Additionally, the stochastic models are extended to cope with directional scattering. Parts of this chapter were published in [WSF14b].

5.1 Components of the Channel

The components of the channel are according to [Bel73] the following three: the direct component, the SR components and the scattered components. Thus, the components are the same as in the V2V channel.

5.1.1 Direct Component

The direct component is always present when communications takes place between two airborne aircraft, as long as there are no obstacles between them. The few instances, where the direct component is shadowed might be for take-off and landing or in case of over the horizon communications. The direct path is the strongest component of the channel and experiences a Doppler shift according to the relative movement of the two aircraft. The direct component is not part of the investigation of this thesis. In most cases the direct component is only influenced by the free space path loss and can be simply added to the channel model, if needed.

5.1.2 Specular Reflection Components

The SR components originate from reflections on the ground. In contrast to (2.5), in most cases only a single component is assumed for the specular reflection [Bel73]. The received power can be quite variable depending on the altitude of the aircraft and the composition of the ground. As presented in [WGDS10], the composition of the ground has a major influence on the strength of the signal. Water acts hereby as very good reflective surface and the power of the reflected component may come close to power of the direct component. The received power of the SR component depends on the dielectric constant, the conductivity and the roughness of the ground. Typical values for the dielectric constant and conductivity can be found in Table I in [Jak94]. Values for the surface roughness are provided in [Bel73]. The direct component and the SR component are only Doppler shifted with no considerable Doppler spread. The SR component is not investigated in the thesis, since it has already been investigated, for example, in [WGDS10]. The specular component can be added to the model similarly to the direct component.

5.1.3 Scattered Components

The scattered components of the channel are caused by scattering of the signal from the ground and the scattered signals cause a large Doppler spread of the received signal. Like the specular reflection component, the received power of the scattered components depends on the altitude of the aircraft and the electrical properties of the ground.

We investigate the time-variant behavior of the scattering and its effects on the received signal. In the remainder of the chapter, we model the scattering according to the previously presented GSCM. The power of the received scattered signals is not as strong as in the V2V scenario, since the distances between the transmitter and receiver are much larger. A three-dimensional geometry has to be used to incorporate the ground scattering into the channel model. By extending the two-dimensional V2V model, an evolution of the 2D model to a more complex 3D model is achieved.

5.2 From a 2D to a 3D Model

In this section, we present, how to evolve a two-dimensional V2V model into a three-dimensional A2A model. We recall the results from Chapter 4 and show the

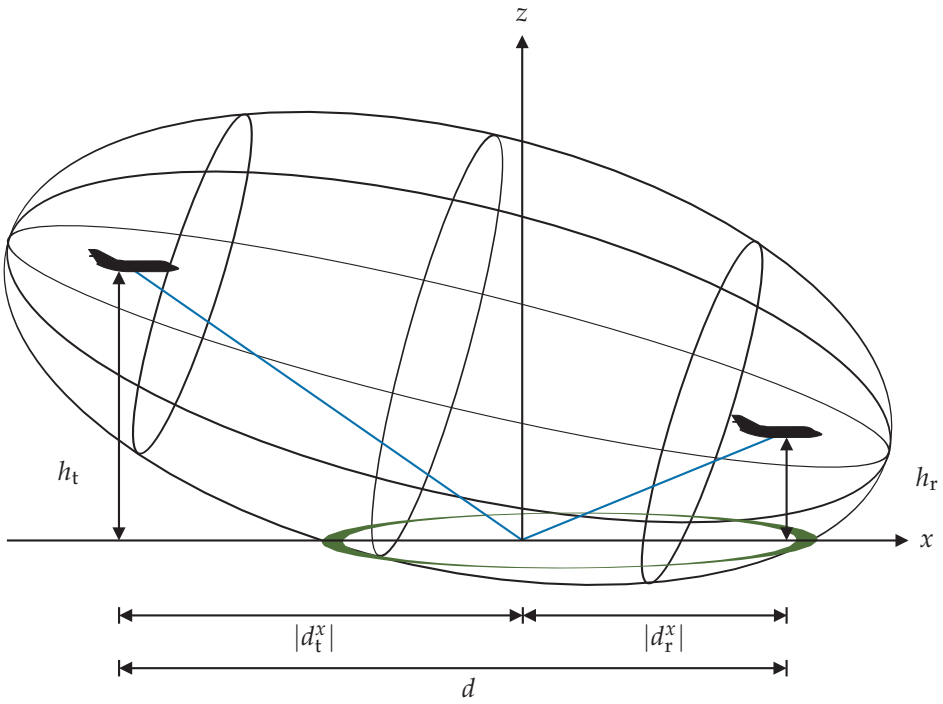

Figure 5.1. *Aircraft positions in the Cartesian coordinate system. An ellipsoid represents the surface of equal delay, which intersects with the ground forming an ellipse.*

subsequent steps that are needed to describe the scattering for the A2A scenario. As in the V2V scenario the model is divided into a geometric and a stochastic part.

5.2.1 Geometric Part

The geometric setup for an A2A scenario is shown in Fig. 5.1. As mentioned before the main difference between the A2A and the V2V scenarios are the aircraft altitudes and the velocities of transmitter and receiver. In order to keep the mathematical description as simple as possible, the origin of the coordinate system is chosen to be at the position, where the specular reflection component hits the ground[1]. As in the V2V scenario the coordinate system moves along the SR component. The aircraft are located in the x-z-plane and the scatterers are distributed in the x-y-plane. The time-variant positions $\mathbf{x}_t(t)$ and $\mathbf{x}_r(t)$ of both aircraft are given as

$$\mathbf{x}_t(t) = \mathbf{x}_{t0} + \int_0^t \mathbf{v}_t(\tau)\,\mathrm{d}\tau \quad \text{and} \quad \mathbf{x}_r(t) = \mathbf{x}_{r0} + \int_0^t \mathbf{v}_r(\tau)\,\mathrm{d}\tau\,, \tag{5.1}$$

where $\mathbf{x}_{t0} = [d_t^x, 0, h_t]^T$ and $\mathbf{x}_{r0} = [d_r^x, 0, h_r]^T$ describe the positions of the transmitter and receiver respectively and $\mathbf{v}_t(t) = \left[v_t^x, v_t^y, v_t^z\right]^T$ and $\mathbf{v}_r(t) = \left[v_r^x, v_r^y, v_r^z\right]^T$ are

[1] referred to as specular reflection point

the corresponding velocity vectors. The x-components of the transmitter and the receiver vector can be expressed as [WSF14b]

$$d_{\mathrm{t}}^{x} = \frac{-h_{\mathrm{t}}}{h_{\mathrm{t}} + h_{\mathrm{r}}} d \quad \text{and} \quad d_{\mathrm{r}}^{x} = \frac{h_{\mathrm{r}}}{h_{\mathrm{t}} + h_{\mathrm{r}}} d\,, \tag{5.2}$$

where d is the horizontal distance between the aircraft, and h_{t} and h_{r} the altitudes of the transmitting and receiving aircraft, respectively, cf. Fig. 5.1.

The equation to calculate the distance from transmitter to receiver via an arbitrary scatterer remains the same as in the vehicular scenario in (4.6) and results in

$$d_{\mathrm{sc}}(\mathbf{x}, t) = \|\mathbf{x} - \mathbf{x}_{\mathrm{t}}(t)\| + \|\mathbf{x} - \mathbf{x}_{\mathrm{r}}(t)\|\,. \tag{5.3}$$

In the 3D scenario the scatterers can be placed anywhere in the three-dimensional space. However, we will restrict the locations of the scatterers to the ground. The Doppler frequency ν for the A2A scenario is like in the V2V scenario given by

$$\nu(\mathbf{x}, t) = \left(\mathbf{v}_{\mathrm{t}}(t)^{\mathrm{T}} \nabla d_{\mathrm{t}}(\mathbf{x}, t) + \mathbf{v}_{\mathrm{r}}(t)^{\mathrm{T}} \nabla d_{\mathrm{r}}(\mathbf{x}, t)\right) \frac{f_{\mathrm{c}}}{c}\,. \tag{5.4}$$

The expanded form is shown in Appendix B.1. In the 3D case, the advantages of the proposed representation compared to a description with trigonometric functions are even bigger as is the 2D case. The equation remains invariant compared to the two-dimensional case, whereas in trigonometric notation, the azimuth and elevation would have to be taken into account. The scalar product in the new notation automatically includes both azimuth and elevation.

In order to determine the delay-dependent Doppler pdf $p(\nu|\tau)$, the locations of all scatterers that induce the same delay τ at the receiver have to be found. For the general three-dimensional case, these scatterers reside on an ellipsoid, with the transmitter and the receiver in its foci. The parameters for the delay ellipsoid at an arbitrary observation time t^* are given by

$$a_{\mathrm{oid}} = \frac{\tau c}{2}\,, \quad b_{\mathrm{oid}} = \sqrt{\frac{\tau^2 c^2}{4} - \frac{\left(\|\mathbf{x}_{\mathrm{t}}(t^*) - \mathbf{x}_{\mathrm{r}}(t^*)\|\right)^2}{4}}\,, \tag{5.5}$$

where a_{oid}, b_{oid}, and c_{oid} are the semi-principal axes of the ellipsoid. Since the speed of light is isotropic a prolate ellipsoid with $c_{\mathrm{oid}} = b_{\mathrm{oid}}$ is obtained. The larger of the semi-principal axes is given by $a_{\mathrm{oid}} \in [(\|\mathbf{x}_{\mathrm{t}}(t^*) - \mathbf{x}_{\mathrm{r}}(t^*)\|)/2, \infty)$ and is directly proportional to the delay τ. An ellipsoid that has its axes aligned with the coordinate axes and its center at the origin of the coordinate system can be described by the following quadratic surface equation

$$\mathbf{x}^{\mathrm{T}} \begin{pmatrix} (1/a_{\mathrm{oid}})^2 & 0 & 0 \\ 0 & (1/b_{\mathrm{oid}})^2 & 0 \\ 0 & 0 & (1/b_{\mathrm{oid}})^2 \end{pmatrix} \mathbf{x} = 1\,. \tag{5.6}$$

The surface of an ellipsoid is called a second order algebraic surface. However, due to the choice of coordinate system, the ellipsoid is not centered at the origin, but shifted and possibly rotated. For the chosen coordinate system the shift occurs in the x-z-plane, whereas the rotation occurs around the y-axis. Both mathematical operations are carried out consecutively and thus we obtain the new coordinates $\mathbf{x}'$

$$\mathbf{x}' = (\mathbf{x} - \mathbf{x}_\mathrm{s})^\mathrm{T} \begin{pmatrix} \cos\alpha & 0 & \sin\alpha \\ 0 & 1 & 0 \\ -\sin\alpha & 0 & \cos\alpha \end{pmatrix} . \tag{5.7}$$

The rotation angle α is measured clockwise between the long semi-principal axis of the ellipsoid and the x-axis. The offset from the origin is given by $\mathbf{x}_\mathrm{s}$. The rotation angle α is determined by

$$\alpha = \arccos\left(\frac{(\mathbf{x}_\mathrm{r}(t^*) - \mathbf{x}_\mathrm{t}(t^*))^\mathrm{T}}{\|\mathbf{x}_\mathrm{r}(t^*) - \mathbf{x}_\mathrm{t}(t^*)\|} \mathbf{e}_\mathrm{x} \right) , \tag{5.8}$$

where $\mathbf{e}_x$ is the unit vector in x-direction. The offset with respect to the origin of the coordinate system is calculated by

$$\mathbf{x}_\mathrm{s} = \frac{\mathbf{x}_\mathrm{t}(t^*) + \mathbf{x}_\mathrm{r}(t^*)}{2} . \tag{5.9}$$

If the aircraft positions are given, the parameters of the ellipsoid are fixed. Since the scattering occurs on the ground, the intersection of the ellipsoid with the ground needs to be determined. In order to keep the equations mathematically tractable, a flat ground is assumed. The geometric shape that results due to the intersection with the ground is either an ellipse, a circle or a single point. In order to obtain the equation for the resulting geometric shape, the ellipsoid equation in (5.6) has to be rewritten in its more general quadratic surface form

$$\mathbf{x}'^\mathrm{T} \begin{pmatrix} a & l & g \\ l & b & m \\ g & m & k \end{pmatrix} \mathbf{x}' + 2 \begin{pmatrix} p & q & r \end{pmatrix} \mathbf{x}' + s = 0 \tag{5.10}$$

with a, b, k, l, m, g, p, q, r, and s being the coefficients of the quadratic surface equation. Depending on the coefficients, different geometric shapes are obtained. In this case, the coefficients describe a rotated and shifted ellipsoid. As stated before, the scattering only occurs on ground. Therefore, (5.10) is simplified considerably. All coefficients that are related to the z-component are set to zero. Furthermore, since

the aircraft are placed in the x-z-plane, all linear terms related to the y-component can be set to zero. Equation (5.10) therefore reduces to

$$\mathbf{x}'^{\mathrm{T}} \begin{pmatrix} a & 0 & 0 \\ 0 & b & 0 \\ 0 & 0 & 0 \end{pmatrix} \mathbf{x}' + 2 \begin{pmatrix} p & 0 & 0 \end{pmatrix} \mathbf{x}' + s = 0 \,. \tag{5.11}$$

The ellipsoid equation becomes an ellipse equation with the semi-major axis aligned with the x-axis. The remaining linear term might shift the ellipse in x-direction. The parameters of the ellipse are given by

$$a_\tau = \sqrt{\left(\frac{p}{a}\right)^2 - \frac{s}{a}}, \quad b_\tau = \sqrt{\frac{p^2}{ab} - \frac{s}{b}}, \quad x_\mathrm{c} = -\frac{p}{a}, \quad y_\mathrm{c} = 0 \,. \tag{5.12}$$

The parameters of the ellipse are inserted into the Doppler frequency equation to obtain the delay-dependent Doppler frequency. In contrast to the V2V scenario, the delay ellipse is offset from the origin. The following equation describes the parametrized ellipse as

$$\mathbf{x}(t^*; \phi|\tau) = \begin{pmatrix} a_\tau \cos\phi \\ b_\tau \sin\phi \end{pmatrix} + \begin{pmatrix} x_\mathrm{c} \\ y_\mathrm{c} \end{pmatrix} . \tag{5.13}$$

The general version of Doppler frequency ν for an arbitrary, but constant delay in the three-dimensional case is shown in Appendix B.2. After having determined the delay-dependent Doppler frequency, the geometric part is concluded. The geometric part is followed the stochastic part as in Chapter 4.

5.2.2 Stochastic Part

The derivation of the delay-dependent Doppler pdf principally remains the same for the A2A scenario similar to the V2V scenario. Therefore, (4.19)–(4.23) can be used for the A2A scenario. The pdf of the delay-dependent ellipse parameter ϕ is given by

$$p(\phi|\tau) = \frac{\sqrt{1 - \epsilon_\tau^2 \cos^2\phi}}{4\mathrm{E}(\epsilon_\tau)} , \tag{5.14}$$

where $\phi \in [0, 2\pi)$. This equation, however, is only valid, if the scatterers are uniformly distributed on the ground.

Since aircraft fly over different terrains, the scattering properties of these terrains might differ. If the aircraft, for example, fly along the coast, the received power due to scattering from the sea are stronger than the received power due to scattering

from the land. Because of the difference in received power, it makes sense to introduce a directional pdf from the field of circular statistics. A very often used circular pdf in channel modeling is the von Mises distribution [Zaj12]. The von Mises distribution is also called circular uniform distribution. The pdf from a circular normal distribution is extended in this thesis to an elliptical normal distribution. The von Mises distribution is given by

$$p(x|\mu,\kappa) = \frac{\exp\left(\kappa\cos\left(x-\mu\right)\right)}{2\pi \mathrm{I}_0(\kappa)}\,, \tag{5.15}$$

with κ being the concentration parameter and μ the centrality parameter of the distribution.

After a substitution of variables, we obtain for the elliptical normal pdf

$$p(\phi|\tau;\kappa,\mu^*) = \frac{\sqrt{1-\epsilon_\tau^2\cos^2\phi}}{4\mathrm{E}(\epsilon_\tau)} \frac{\exp\left(\kappa\cos\left(\frac{\pi}{2\mathrm{E}(\epsilon_\tau)}\left(\int_0^\phi \sqrt{1-\epsilon_\tau^2\cos^2\zeta}\,\mathrm{d}\zeta - \mu^*\right)\right)\right)}{\mathrm{I}_0(\kappa)}\,, \tag{5.16}$$

with $\mu^* = \int_0^{\bar{\phi}} \sqrt{1-\epsilon_\tau^2\cos^2\zeta}\,\mathrm{d}\zeta$ providing the direction, where the strongest scattering comes from and $\bar{\phi}$ being the mean scattering direction. As mentioned in the V2V chapter, the parameter ϕ is related to the polar angle φ, which can be measured in a Cartesian coordinate system or with a compass, by

$$\tan\varphi = \sqrt{1-\epsilon_\tau^2}\tan\phi\,. \tag{5.17}$$

This relationship becomes important due to the von Mises distribution, where an angle is needed. The mean angle $\bar{\varphi}$ can be extracted from measurement data and fed into the model. The directionality parameter κ has to be extracted from measurement data as well. After the parameters have been determined, directional delay-dependent Doppler pdfs can be calculated, since the terrain properties are directly affecting the pdfs.

The delay-dependent Doppler pdf is given similar to Chapter 4 by

$$p(\nu|\tau) = \sum_{\phi'\in\left\{\mathcal{F}^{-1}(\nu)\right\}} \frac{p(\phi'|\tau)}{\left|\frac{\mathrm{d}\nu}{\mathrm{d}\phi'}\right|}\,. \tag{5.18}$$

The derivative of the Doppler frequency is shown in Appendix C. For the distribution of the scatterers there are two options with (5.14) and (5.16). Depending on $p(\phi|\tau)$ the delay-dependent Doppler frequency pdf $p(\nu|\tau)$ changes its shape. The main scattering direction influences the delay-dependent Doppler pdf. Once the delay-dependent Doppler pdf is calculated the joint delay Doppler pdf is obtained by $p(\tau,\nu) = p(\tau)p(\nu|\tau)$. For arbitrary times t it becomes the time-variant pdf $p(t;\tau,\nu)$.

5.3 Theoretical Results

In this section, we present the evaluation of the joint delay Doppler pdf and show the impact of the flight geometry onto the channel model. We present four scenarios, with three of the four scenarios also being used as measurement scenarios during the measurement campaign. The head-on scenario, however, was too dangerous to fly. But as the channel model is confirmed by the other three scenarios, we are confident that it is the same for the head-on scenario. The positions and velocities correspond to values used in the A2A measurement campaign described in Chapter 3, [WGDS10], and [WS11], so that the theoretical results can be compared to the measurements. The carrier frequency for all simulations and measurements in this chapter is $f_c = 250\,\text{MHz}$. Note that all scenarios are evaluated at a certain time t^*, where the geometric set-up is as stated in the scenario description. The notation is simplified to $\mathbf{v}(t^*) = \mathbf{v}$. The delay-dependent Doppler pdf $p(t^*;\nu|\tau)$ and the joint delay Doppler pdf $p(t^*;\tau,\nu)$ are shown in the logarithmic domain, i.e., $10\log_{10}\left(p(t^*;\nu|\tau)\right)$ and $10\log_{10}\left(p(t^*;\nu|\tau)\right)$. For the delay-dependent Doppler pdf $\int_{-\infty}^{\infty} p(t^*;\nu|\tau) = 1$, whereas the joint delay Doppler pdf consists of contiguous blocks of delay-dependent pdfs evaluated for different τ. Therefore, in a strict sense, they are not correctly scaled, but make the figures consistent. The details for the scenarios are given below:

- Scenario VI: Two aircraft fly behind each other at the same altitude and with the same speed in the same direction. The transmitter is at position $\mathbf{x}_{t0} = [-1175, 0, 600]^T\text{m}$ with velocity vector $\mathbf{v}_t = [250, 0, 0]^T\text{km/h}$. The receiver is at position $\mathbf{x}_{r0} = [1175, 0, 600]^T\text{m}$ with velocity vector $\mathbf{v}_r = [250, 0, 0]^T\text{km/h}$. The scatterers are uniformly distributed on the ground.

- Scenario VII: Two aircraft fly behind each other at different altitudes, but with the same speed in the same direction. The transmitter is at position $\mathbf{x}_{t0} = [-1790, 0, 1600]^T\text{m}$ with velocity vector $\mathbf{v}_t = [250, 0, 0]^T\text{km/h}$. The receiver is at position $\mathbf{x}_{r0} = [640, 0, 600]^T\text{m}$ with velocity vector $\mathbf{v}_r = [250, 0, 0]^T\text{km/h}$. The scatterers are uniformly distributed on the ground.

- Scenario VIII: Two aircraft fly towards each other at the same altitude and with the same speed in opposite directions. The transmitter is at position $\mathbf{x}_{t0} = [-1175, 0, 600]^T\text{m}$ with velocity vector $\mathbf{v}_t = [250, 0, 0]^T\text{km/h}$. The receiver is at position $\mathbf{x}_{r0} = [1175, 0, 600]^T\text{m}$ with velocity vector $\mathbf{v}_r = [-250, 0, 0]^T\text{km/h}$. The scatterers are uniformly distributed on the ground.

- Scenario IX: Two aircraft fly behind each other at the same altitude and with the same speed in the same direction. The transmitter is at position $\mathbf{x}_{t0} = [-1175, 0, 600]^T$m with velocity vector $\mathbf{v}_t = [250, 0, 0]^T$km/h. The receiver is at position $\mathbf{x}_{r0} = [1175, 0, 600]^T$m with velocity vector $\mathbf{v}_r = [250, 0, 0]^T$km/h. The scatterers are distributed on the ground according to the von Mises distribution as in (5.15) with the concentration parameter $\kappa = 0.5$ and mean angle $\bar{\varphi} = \pi/4$.

Scenario VI: Fig. 5.2 shows the joint delay Doppler pdf and delay-dependent Doppler pdf. Compared to the V2V scenarios, the rounded shape of the joint delay Doppler pdf in Fig. 5.2a is characteristic. The SR component is at $\tau = 8.8\,\mu$s with $\nu = 0$ Hz and from there the Doppler frequency of the scattered components quickly widens for increasing delays. For large delays the Doppler frequency asymptotically reaches the limit of $\nu = \pm\left(\|\mathbf{v}_t\| + \|\mathbf{v}_r\|\right) f_c/c = \pm 117$ Hz. The reason for the different behavior compared to the V2V scenario can be found in the geometry. Since both aircraft are airborne, the delay ellipsoid needs to be large enough to intersect with the ground. With growing delay the ellipsoid first intersects the ground at one point, which is the SR point. As the delay ellipsoid increases, the intersection with the ground plane becomes an ellipse, but does not include all Doppler frequencies yet. As the ellipse grows, more Doppler frequencies are incorporated and the delay-dependent Doppler pdf widens. This effect can be seen in Fig. 5.2b, which shows the Doppler pdf for delays of $\tau = 9\,\mu$s to $\tau = 16\,\mu$s. The pdf at $\tau = 9\,\mu$s is roughly 30 Hz wide and shows the distinctive W shape, which is typical for scattering close to the SR component. The pdf for $\tau = 10\,\mu$s is already 100 Hz in width and the W shape is still visible. For $\tau = 16\,\mu$s the spectrum width is larger than 200 Hz and the W shape is not visible anymore. The spectrum looks more like the Jakes spectrum, which is asymptotically reached for $\tau \to \infty$.

Scenario VII: Fig. 5.3 shows the joint delay Doppler pdf and the delay-dependent pdf. The effect of the different altitudes is clearly visible. The joint delay Doppler pdf in Fig. 5.3a does not posses symmetry around the delay axis anymore. The difference in altitude affects the maximum and minimum Doppler frequency. The positive and negative Doppler frequencies are affected differently by the asymmetry in altitude. For increasing delay, the positive Doppler frequencies increase faster than the negative ones. Furthermore, the SR component occurs later, since one aircraft is at a higher altitude and the delay ellipsoid needs to be larger to intersect the ground. Since the ellipsoid is tilted when it intersects the ground, the ellipse is not centered at the origin of the coordinate system for delays larger than the SR component. For an arbitrary, but fixed delay, the probability of occurrence for a negative frequency is slightly higher than for the same positive frequency. This ef-

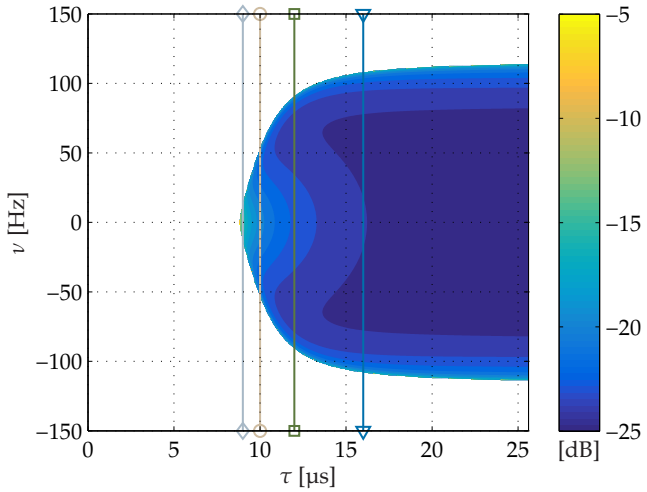

(a) *Joint delay Doppler pdf in logarithmic domain:* $10\log_{10}\left(p(t^*;\tau,\nu)\right)$. *Vertical lines indicate cuts through the pdf to obtain the Doppler pdfs shown in (b).*

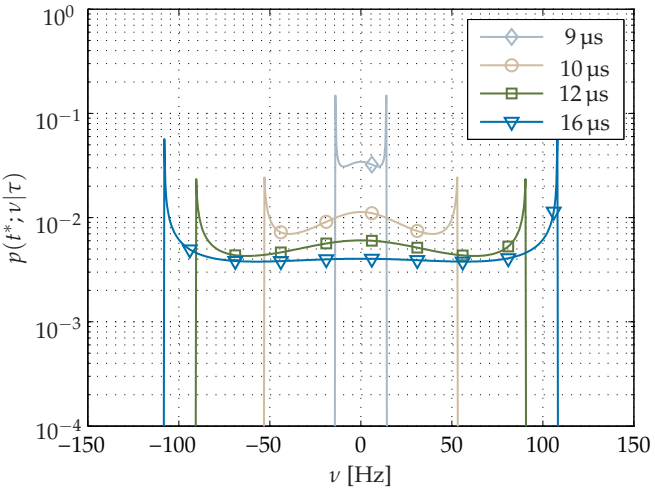

(b) *Doppler pdfs* $p(t^*;\nu|\tau)$ *for the different delays indicated in (a).*

Figure 5.2. *Scenario VI: Aircraft at positions* $\mathbf{x}_{t0} = [-1175, 0, 600]^T\text{m}$ *and* $\mathbf{x}_{r0} = [1175, 0, 600]^T\text{m}$ *with velocity vectors* $\mathbf{v}_t = \mathbf{v}_r = [250, 0, 0]^T\text{km/h}$.

fect occurs more prominently in Fig. 5.3b, which shows the Doppler pdf for delays from $\tau = 11\,\mu\text{s}$ to $\tau = 18\,\mu\text{s}$. The pdf at $\tau = 11\,\mu\text{s}$ possesses asymmetric limits. Furthermore, the pdf shows a different behavior compared to Scenario VI. The W shape vanishes and instead the pdf looks like an asymmetric Jakes pdf, where the negative Doppler frequencies are more probable. For a delay of $\tau = 10\,\mu\text{s}$ the width already increases to 100 Hz with the negative frequencies still more probable. For $\tau = 18\,\mu\text{s}$ the shape of the pdf becomes more symmetric. The width of the pdf is

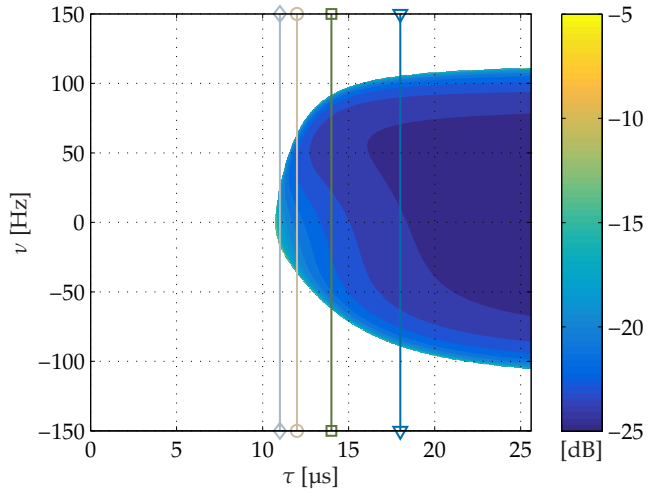

(a) *Joint delay Doppler pdf in logarithmic domain:* $10\log_{10}\left(p(t^*;\tau,\nu)\right)$. *Vertical lines indicate cuts through the pdf to obtain the Doppler pdfs shown in (b).*

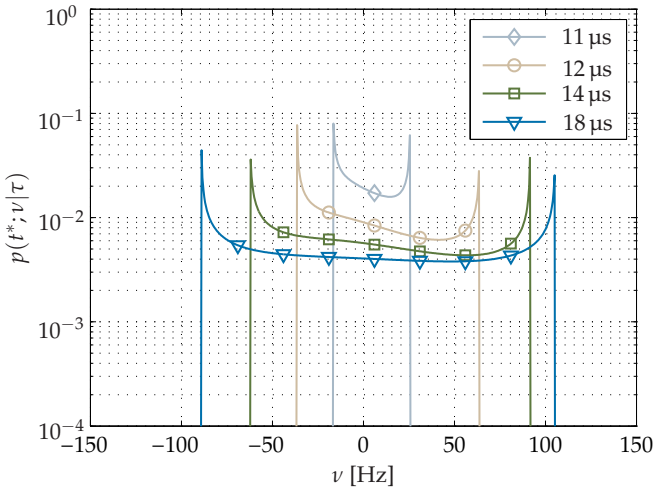

(b) *Doppler pdfs* $p(t^*;\nu|\tau)$ *for the different delays indicated in (a).*

Figure 5.3. *Scenario VII: Aircraft at positions* $\mathbf{x}_{t0} = [-1790, 0, 1600]^T\text{m}$ *and* $\mathbf{x}_{r0} = [640, 0, 600]^T\text{m}$ *with velocity vectors* $\mathbf{v}_t = \mathbf{v}_r = [250, 0, 0]^T\text{km/h}$.

approximately 200 Hz with the minimum and maximum frequencies being slightly asymmetric as well. It can be shown for different altitudes as well that the pdf converges towards the Jakes spectrum for $\tau \to \infty$.

Scenario VIII: Fig. 5.4 shows the joint delay Doppler pdf and the delay-dependent Doppler pdf. The joint delay Doppler pdf in Fig. 5.4a shows a completely different behavior than the pdfs in Scenario VI or VII. The SR component possesses the highest Doppler frequency and the lowest delay at $\nu = 117\,\text{Hz}$ and $\tau = 8.8\,\mu\text{s}$. The

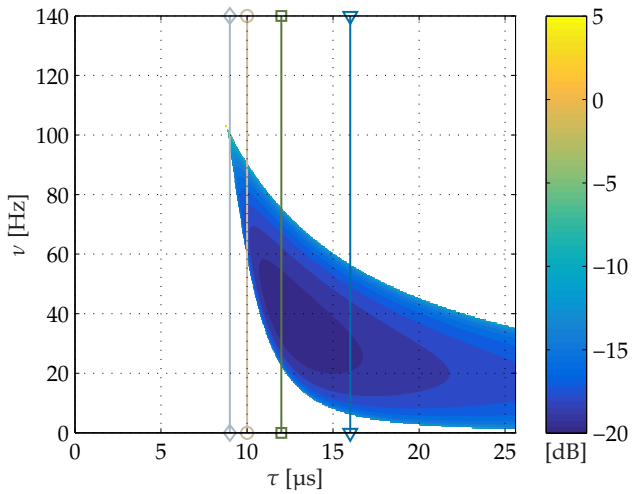

(a) *Joint delay Doppler pdf in logarithmic domain:* $10\log_{10}\left(p(t^*;\tau,\nu)\right)$. *Vertical lines indicate cuts through the pdf to obtain the Doppler pdfs shown in (b).*

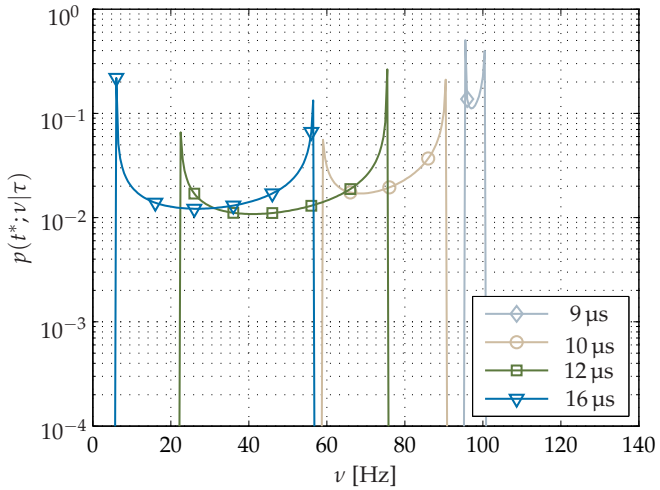

(b) *Doppler pdfs* $p(t^*;\nu|\tau)$ *for the different delays indicated in (a).*

Figure 5.4. *Scenario VIII: Aircraft at positions* $\mathbf{x}_{t0} = [-1175, 0, 600]^T\text{m}$ *and* $\mathbf{x}_{r0} = [1175, 0, 600]^T\text{m}$ *with velocity vectors* $\mathbf{v}_t = -\mathbf{v}_r = [250, 0, 0]^T\text{km/h}$.

Doppler pdf caused by the scattered components widens for increasing delay. Additionally, the spectrum gets shifted towards lower frequencies. Hereby, the maximum frequency decays slower than the minimum frequency. Therefore, the increase in width occurs very fast for $\tau \in [8.8, 12]\mu\text{s}$ and then the width remains almost constant. The Doppler frequency remains positive for all possible delays, which separates this particular scenario from the previous two. The reason for the positiveness is the completely different Doppler frequency distribution on the ground.

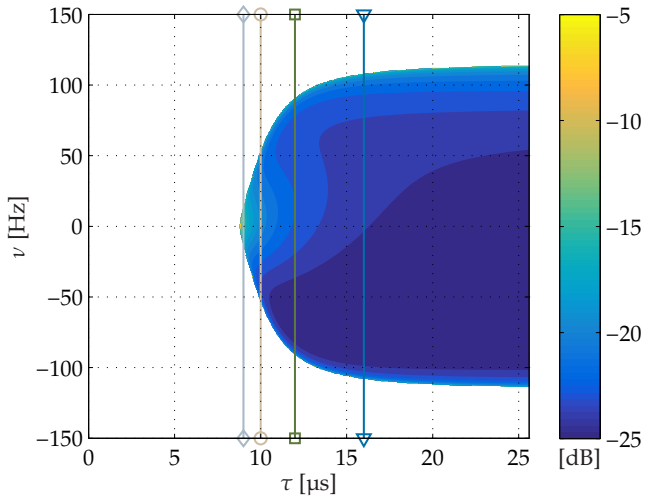

(a) *Joint delay Doppler pdf in logarithmic domain:* $10\log_{10}\left(p(t^*;\tau,\nu)\right)$. *Vertical lines indicate cuts through the pdf to obtain the Doppler pdfs shown in (b).*

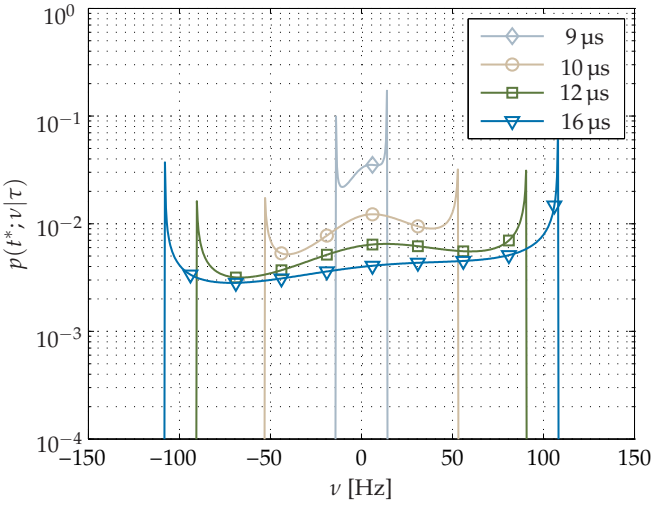

(b) *Doppler pdfs* $p(t^*;\nu|\tau)$ *for the different delays indicated in (a).*

Figure 5.5. *Scenario IX: Aircraft at positions* $\mathbf{x}_{t0} = [-1175, 0, 600]^T\text{m}$ *and* $\mathbf{x}_{r0} = [1175, 0, 600]^T\text{m}$ *with velocity vectors* $\mathbf{v}_t = \mathbf{v}_r = [250, 0, 0]^T\text{km/h}$.

This Doppler frequency distribution consists only of positive Doppler frequencies, which is a similar result to the V2V scenario in Fig. 4.6.

The delay-dependent pdf is shown in Fig. 5.4b. There the widening of the pdf and the shift towards lower frequencies becomes obvious. The pdf at $\tau = 9\,\mu\text{s}$ is only about 5 Hz wide, whereas the one at $\tau = 10\,\mu\text{s}$ is already 30 Hz wide; the ones for $\tau = 12\,\mu\text{s}$ and $\tau = 16\,\mu\text{s}$ have a width of more than 50 Hz. The shift from high

to low frequencies for increasing delay is also noticeable. The pdfs for $\tau = 9\,\mu s$, $\tau = 10\,\mu s$ and $\tau = 16\,\mu s$ do not overlap. The shape of the pdfs looks very similar to the Jakes pdf, but a slightly asymmetric like in Scenario VII. The effect of asymmetry is stronger for shorter delay and becomes less for larger delays.

Scenario IX: Fig. 5.5 shows the joint delay Doppler pdf and the delay-dependent pdf. The outer shape in Fig. 5.5a looks the same as the joint delay Doppler pdf in Scenario VI. However, the inner distribution looks different. The Doppler frequencies are not symmetrically distributed with respect to the delay axis. There are more contributions from the positive frequencies, i.e., more scattering occurs in front of the aircraft. The stronger contributions are taken into account by using the von Mises distribution, where the mean angle was assumed to be $\bar{\varphi} = \pi/4$ and the concentration parameter $\kappa = 0.5$. Such parameters mean that the strongest scattering comes from the left front. The directional effect is strongest for small delays and gets weaker, if the delay is large. The impact of different scattering properties becomes obvious, if the aircraft fly over water and ground at the same time, for example, if they fly along the coast. The contribution from the scattering from the water is lower, since water scatters the signal worse than solid ground for a calm sea. This effect is also shown in the subsequent validation with measurement data.

The delay-dependent Doppler pdfs are shown in Fig. 5.5b. Different pdfs compared to Scenario VI can be observed. For $\tau = 9\,\mu s$ positive Doppler frequencies are more probable and therefore the W shape is distorted. This distortion occurs for the other delays of $\tau = 10\,\mu s$, $\tau = 12\,\mu s$, and $\tau = 16\,\mu s$ as well, but the distortion becomes smaller for larger delays. The properties of the ground therefore have a direct influence on the Doppler pdf of the channel. Good conducting surfaces increase the probability of the Doppler frequency and have to be taken into account when modeling non-stationary channels. When flying over different terrains the scattering properties have to included in the model to reflect the changes in the propagation environment. A directional scatterer distribution is therefore the right choice.

5.4 Validation

As in the V2V scenario the measured Doppler spectra are compared with scaled and averaged pdfs that are calculated by the A2A model in order to validate our theoretical claims. Furthermore, the measured Doppler spectrum for a certain delay indicated by a cut through the estimated, normalized spreading function is compared with the scaled and averaged Doppler pdf. The estimated spreading function $\hat{s}[t^*; m, k]$ is calculated by taking $N_\mathrm{b} = 1024$ CIRs and apply a Fourier transform.

The application of the Fourier transform means that the signal is averaged over $\Delta t = N_\mathrm{b} T_\mathrm{g} = 1.05\,\mathrm{s}$. In contrast, the theoretically derived pdf provides an instantaneous stochastic dependency between delay and Doppler. To be able to compare measured estimated spreading function with the theoretically derived pdfs, we consider a linear combination of the instantaneous delay Doppler pdfs over the same time interval Δt used for computing the spreading function $\hat{s}[t^*; m, k]$. The resulting temporal mixture is computed as shown in (4.24). The weights are distributed equally such that $w_i = 1/N_\mathrm{b}\,\forall i$. Since the geometry does not change in the A2A scenarios, the averaged pdf corresponds approximately to the instantaneous pdf $\bar{p}(t^*; \tau, \nu) \approx p(t^*; \tau, \nu)$. Additionally, $\bar{p}(t^*; \tau, \nu)$ is scaled and the distribution of the delay $p(\tau)$ is determined by an exponential path loss model with an estimated path loss coefficient for the scattering, which is determined with a simple least squares algorithm.

In order to compare the theoretical results with the measurement results, similar geometric scenarios numbered from X to XII are used. The distances and altitudes are slightly different compared to the theoretical scenarios presented before, but the geometry remains the same, which is important for the comparison. Since the head-on scenario was to dangerous to fly, the theoretical results cannot be validated. The other theoretical results, however, are validated and we are confident that the results from the head-on scenario are adequately described by the theoretical model. The actual values for distance and speed are extracted from the on-board GPS devices that were used during the measurement campaign. The carrier frequency is located at $f_\mathrm{c} = 250\,\mathrm{MHz}$ and the power of the estimated spreading function is normalized by the square root of the transmit power P_t, so that the path loss including the antenna gains is shown, i.e., $20\log_{10}\left(|\hat{s}[t^*, m, k]|/\sqrt{P_\mathrm{t}}\right)$. The remaining parameters for the three scenarios are summarized below:

- Scenario X: Two aircraft fly behind each other at the same altitude and with similar speed in the same direction. The transmitter is at position $\mathbf{x}_{\mathrm{t}0} = [-1243, 0, 597]^\mathrm{T}\mathrm{m}$ with velocity vector $\mathbf{v}_\mathrm{t} = [287, 0, 0]^\mathrm{T}\mathrm{km/h}$. The receiver is at position $\mathbf{x}_{\mathrm{r}0} = [1199, 0, 576]^\mathrm{T}\mathrm{m}$ with velocity vector $\mathbf{v}_\mathrm{r} = [254, 0, 0]^\mathrm{T}\mathrm{km/h}$. The scatterers are uniformly distributed on the ground.

- Scenario XI: Two aircraft fly behind each other at different altitudes with similar speed in the same direction. The transmitter is at position $\mathbf{x}_{\mathrm{t}0} = [-2876, 0, 1748]^\mathrm{T}\mathrm{m}$ with velocity vector $\mathbf{v}_\mathrm{t} = [267, 0, 0]^\mathrm{T}\mathrm{km/h}$. The receiver is at $\mathbf{x}_\mathrm{r} = [1007, 0, 612]^\mathrm{T}\mathrm{m}$ with velocity vector $\mathbf{v}_\mathrm{r} = [256, 0, 0]^\mathrm{T}\mathrm{km/h}$. The scatterers are uniformly distributed on the ground.

- Scenario XII: Two aircraft fly behind each other at the same altitude and with similar speed in the same direction. The transmitter is at position $\mathbf{x}_{t0} = [-949, 0, 595]^T$m with velocity vector $\mathbf{v}_t = [163, -178, 0]^T$km/h. The receiver is at position $\mathbf{x}_{r0} = [961, 0, 602]^T$m with velocity vector $\mathbf{v}_r = [182, 199, 0]^T$km/h. The scatterers are distributed on the ground according to the von Mises distribution as in (5.15) with the concentration parameter $\kappa = 1.5$ and centrality angle $\bar{\varphi} = -\pi/4$.

Scenario X: Fig. 5.6 shows the power of the normalized estimated spreading function and the Doppler power spectrum for a flight above forest. The shape of the normalized estimated spreading function in Fig. 5.6a matches the theoretical joint pdf shown in Fig. 5.2a. Additionally, the LOS can be seen at $\tau = 8.1\,\mu$s. Since we set a noise threshold, the scattering is only visible until a normalized received power of $P_r = -160\,$dB until about $\tau = 13\,\mu$s. The Doppler frequency spreads out from $\nu = 0\,$Hz at $\tau = 9\,\mu$s to $\nu = \pm\left(\|\mathbf{v}_t\| + \|\mathbf{v}_r\|\right) f_c/c = \pm 125\,$Hz as is predicted by the theoretical model. Furthermore, the normalized estimated spreading function shows a slightly skewed symmetry around the delay axis due to a slight difference in altitude and velocity of the aircraft, which is easily reproduced with the theoretical model.

Fig 5.6b shows the Doppler power spectrum for a delay of $\tau = 11\,\mu$s. Since the parameters are slightly different compared to Scenario VI, we calculated the scaled and averaged Doppler pdf, which is shown as the superimposed line, for the exact parameters of Scenario X. As predicted by the theoretical model, the measured Doppler spectrum shows the typical W shape close to the SR component. For such a spectrum the Doppler frequencies close to 0 Hz possess more power than for the Jakes spectrum. For the selected delay the scattering power is about 15 dB above the noise level.

Scenario XI: Fig. 5.7 shows the power of the normalized estimated spreading function and the Doppler power spectrum over forest and grass. Due to the different altitudes of the aircraft the shape of the normalized estimated spreading function in the delay Doppler domain becomes asymmetric in Fig. 5.7a beginning at the SR component at $\tau = 15.1\,\mu$s. This asymmetry corresponds to the joint delay Doppler pdf presented in Fig. 5.3a. The distance between the aircraft in this measurement scenario is about 1600 m larger than in Scenario VII. The large distance and the altitude of the transmitter $h_t = 1748\,$m make the scattering hard to discern, especially for negative Doppler frequencies.

Fig 5.7b shows the Doppler power spectrum for a delay of $\tau = 15.65\,\mu$s. The scaled and averaged Doppler pdf is again superimposed on the Doppler spectrum

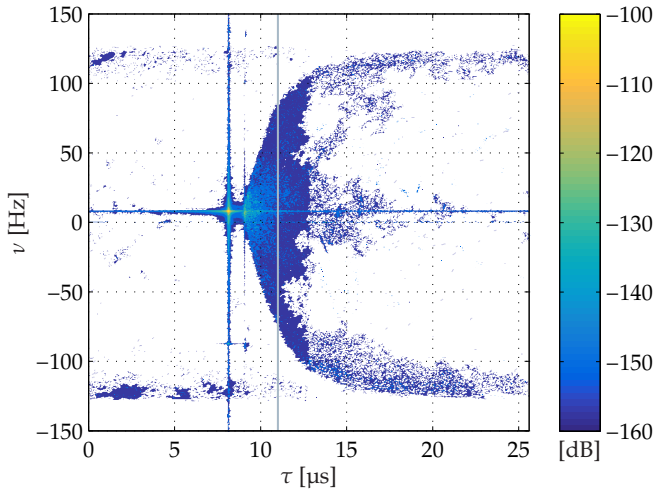

(a) *Normalized estimated spreading function in logarithmic domain:* $20\log_{10}\left(|\hat{s}[t^*;m,k]|/\sqrt{P_\mathrm{t}}\right)$. *Vertical line indicates cut through* $\hat{s}[t^*;m,k]$ *to obtain the Doppler power spectrum shown in (b).*

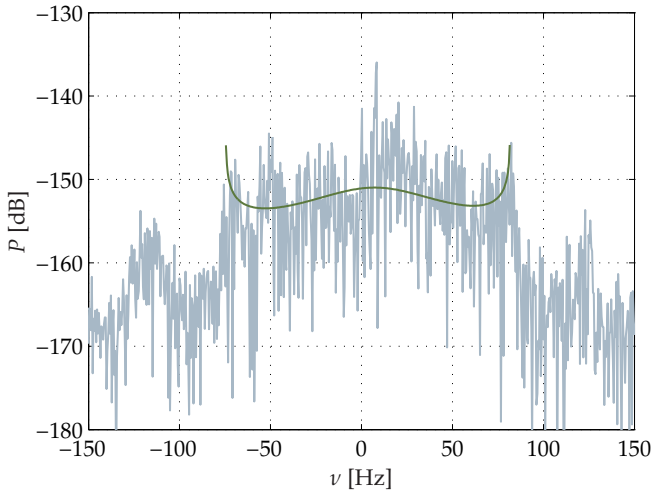

(b) *Doppler power spectrum and scaled, averaged Doppler pdf in logarithmic domain:* $10\log_{10}\left(P_\nu(t^*;\nu|\tau)\right)$ *and* $10\log_{10}\left(\bar{p}(t^*;\nu|\tau)\right)$ *for a delay of* $\tau = 11\,\mu\mathrm{s}$.

Figure 5.6. *Scenario X: Aircraft positions of* $\mathbf{x}_{\mathrm{t}0} = [-1243, 0, 597]^{\mathrm{T}}\mathrm{m}$ *and* $\mathbf{x}_{\mathrm{r}0} = [1199, 0, 576]^{\mathrm{T}}\mathrm{m}$ *and velocity vectors of* $\mathbf{v}_\mathrm{t} = [287, 0, 0]^{\mathrm{T}}\mathrm{km/h}$ *and* $\mathbf{v}_\mathrm{r} = [254, 0, 0]^{\mathrm{T}}\mathrm{km/h}$.

and both curves match very well. The width for positive Doppler frequencies is a little bit overestimated in the theoretical model. One explanation might be that the ground in front of the aircraft didn't scatter back the signal. Furthermore, the altitude of the transmitter causes the scattering to be weak. However, the asymmetric

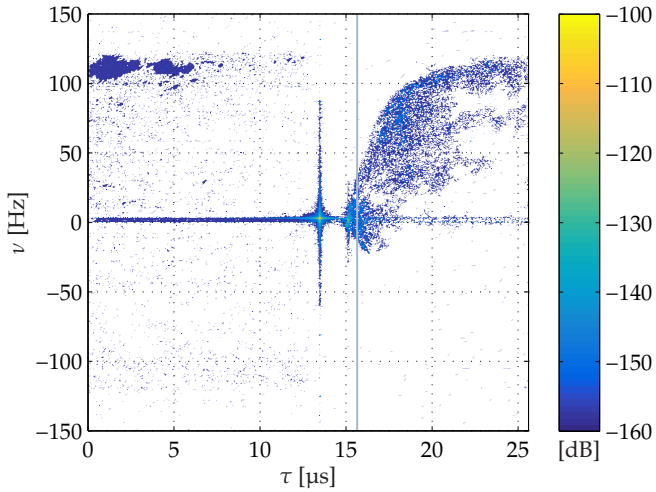

(a) *Normalized estimated spreading function in logarithmic domain:* $20\log_{10}\left(|\hat{s}[t^*;m,k]|/\sqrt{P_\mathrm{t}}\right)$. *Vertical line indicates cut through* $\hat{s}[t^*;m,k]$ *to obtain the Doppler power spectrum shown in (b).*

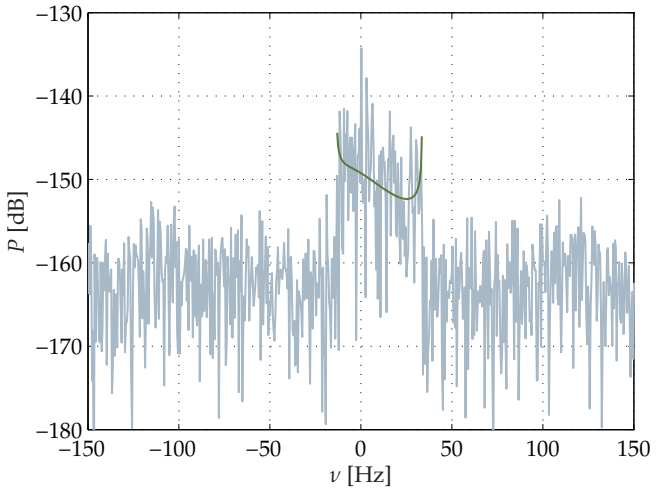

(b) *Doppler power spectrum and scaled, averaged Doppler pdf in logarithmic domain:* $10\log_{10}\left(P_\nu(t^*;\nu|\tau)\right)$ *and* $10\log_{10}\left(\bar{p}(t^*;\nu|\tau)\right)$ *for a delay of* $\tau = 15.65\,\mu\mathrm{s}$.

Figure 5.7. *Scenario XI: Aircraft positions of* $\mathbf{x}_{\mathrm{t}0} = [-2876, 0, 1748]^{\mathrm{T}}\mathrm{m}$ *and* $\mathbf{x}_{\mathrm{r}0} = [107, 0, 612]^{\mathrm{T}}\mathrm{m}$ *and velocity vectors of* $\mathbf{v}_\mathrm{t} = [267, 0, 0]^{\mathrm{T}}\mathrm{km/h}$ *and* $\mathbf{v}_\mathrm{r} = [256, 0, 0]^{\mathrm{T}}\mathrm{km/h}$.

Doppler power distribution due to the difference in altitude is confirmed. For the selected delay the scattering power is about 10 dB above the noise level.

Scenario XII: Fig. 5.8 shows the power of the normalized estimated spreading function and the Doppler power spectrum over water and grass. The normalized estimated spreading function shows a symmetric behavior due to the similar alti-

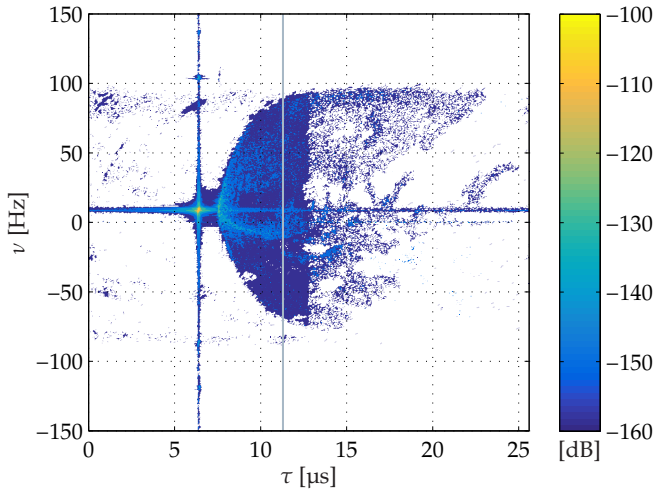

(a) *Normalized estimated spreading function in logarithmic domain:* $20\log_{10}\left(|\hat{s}[t^*;m,k]|/\sqrt{P_\mathrm{t}}\right)$. *Vertical line indicates cut through* $\hat{s}[t^*;m,k]$ *to obtain the Doppler power spectrum shown in (b).*

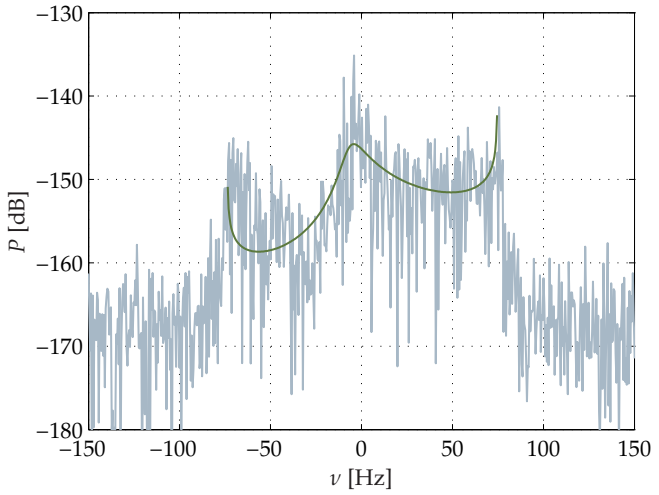

(b) *Doppler power spectrum and scaled, averaged Doppler pdf in logarithmic domain:* $10\log_{10}\left(P_\nu(t^*;\nu|\tau)\right)$ *and* $10\log_{10}\left(\bar{p}(t^*;\nu|\tau)\right)$ *for a delay of* $\tau = 11.35\,\mu\mathrm{s}$.

Figure 5.8. *Scenario XII: Aircraft positions of* $\mathbf{x}_{\mathrm{t}0} = [-949, 0, 595]^{\mathrm{T}}\mathrm{m}$ *and* $\mathbf{x}_{\mathrm{r}0} = [961, 0, 602]^{\mathrm{T}}\mathrm{m}$ *and velocity vectors of* $\mathbf{v}_\mathrm{t} = [163, -178, 0]^{\mathrm{T}}\mathrm{km/h}$ *and* $\mathbf{v}_\mathrm{r} = [182, 199, 0]^{\mathrm{T}}\mathrm{km/h}$, $\kappa = 1.5$ *and* $\bar{\varphi} = -\pi/4$.

tudes of transmitter and receiver. Therefore, the normalized estimated spreading function in Fig. 5.8a matches the joint delay Doppler pdf in Fig. 5.5a. The Doppler frequencies increase symmetrically for increasing delay from the SR component at $\tau = 6.37\,\mu\mathrm{s}$ and can be observed to about $\tau = 12.8\,\mu\mathrm{s}$. The different distribution

of the power inside the normalized estimated spreading function can already be guessed, but is better observed in the Doppler power spectrum.

Fig 5.8b shows the Doppler power spectrum for a delay of $\tau = 11.35\,\mu s$. The scaled and averaged Doppler pdf is calculated with the von Mises scatterer distribution with parameters of $\kappa = 1.5$ and $\bar{\varphi} = -\pi/4$. The parameters are estimated for the measurement scenario, where the aircraft flew with a heading of 95° and Lake Starnberg was directly behind the transmitter. The Doppler power spectrum confirms that more power is received from the scattering from the ground in front of the aircraft and less from behind. Obviously, due to the better scattering properties of the terrain in front of the aircraft, i.e., grass and forest, the signal is received at higher power compared to the signal received from the terrain behind the aircraft, i.e., water. For the selected delay the scattering power is about 15 dB above the noise level for the scattering coming from the terrain in front of the aircraft and only about 10 dB for the scattering coming from behind.

Chapter 6

Summary and Outlook

In this thesis, the influence of scattering in non-stationary mobile-to-mobile channels has been investigated. The investigation was prompted by the fact that mobile-to-mobile channels differ substantially from fixed-to-mobile channels. Most of the fixed-to-mobile channels can be adequately modeled by the wide-sense stationary, uncorrelated scattering models introduced by Bello. The movement of both transmitter and receiver in a mobile-to-mobile channel, however, require new non-stationary models.

In this work, a geometric-stochastic channel model is introduced, because it takes the non-stationarity into account and allows a greater flexibility in describing different scenarios compared to ray tracing models. The geometric part includes the non-stationarity of the channel, whereas the stochastic part makes it possible to describe a wide variety of scenarios. While geometric-stochastic channel models are frequently used to model mobile-to-mobile channels, closed-form solutions of the mathematical descriptions are rare. We present closed-form mathematical descriptions for two examples of the mobile-to-mobile channel, which are the vehicle-to-vehicle and the air-to-air channel.
The main contributions of the thesis are summarized:

- A simulation model is proposed, where the coefficients become time-variant in order to reflect the non-stationarity of the channel. The coefficients can be calculated by employing the equations of the delay-dependent Doppler frequency pdf for every tap. The coefficients are directly influenced by the geometry of the scenario.

- Two measurement campaigns were conducted, which both gave reason to investigate the non-stationarity of mobile-to-mobile channels. Additionally, they

provided the necessary data for validation of the new mathematical models after the processing. The vehicle-to-vehicle campaign was conducted at a carrier frequency $f_c = 5.2\,\text{GHz}$ and with a bandwidth $B = 120\,\text{MHz}$. The air-to-air campaign was conducted at a carrier frequency $f_c = 250\,\text{MHz}$ and with a bandwidth $B = 20\,\text{MHz}$. The evaluation of both measurement campaigns confirmed that the wide-sense stationary uncorrelated scattering assumption has only limited validity for mobile-to-mobile channels. The violation of the wide-sense stationary uncorrelated scattering assumption depends on the geometry of the scenario. For this reason a new geometric-stochastic channel model for mobile-to-mobile channels is needed.

- We derive a new geometric-stochastic channel model for mobile-to-mobile channels. Our focus is on calculating closed-form solutions for the model that give insight into the physical propagation mechanisms of the channel. The model extends the methods and results of wide-sense stationary uncorrelated scattering channels to non-wide-sense stationary uncorrelated scattering channels. The model is kept so general that it can be applied to two different mobile-to-mobile channels, the vehicle-to-vehicle, and the air-to-air channel.

- We present geometric descriptions for the delay and Doppler frequency caused by scattering. Locations of scatterers causing a delay at the receiver are described by an ellipsoid or an ellipse, respectively, if only scattering from the ground is assumed. The Doppler frequency is obtained by the spatial derivation of the distance to the scatterers. This approach allows us to obtain delay-dependent expressions of the Doppler frequencies by inserting the ellipse parameters of the delay ellipse. The delay-dependent description reduces the number of variables to only one, which is necessary to derive the Doppler probability density function.

- The geometric description enables us to derive closed form solutions in the stochastic part of the model. The delay-dependent Doppler probability density functions are calculated by applying probability transformations. The result of our derivations means that there is an infinite number of Doppler probability density functions depending on the geometry of transmitter and receiver. The traditional Jakes Doppler pdf is included as special case in the model. A generalization of the Doppler pdfs is therefore achieved by using the new geometric-stochastic channel model.

- The theoretical geometric-stochastic channel model is validated by measurement data for both the vehicle-to-vehicle and air-to-air case. The validation is an im-

portant confirmation that the model describes the channel adequately. In both cases the measurement data matches the data produced by the model in the delay Doppler domain. Additionally, the model is validated by comparisons to measurement data from other institutions. By having confirmed certain scenarios, the theoretical model can be applied to other scenarios that haven't been measured.

- A suitable coordinate system is introduced to simplify the calculations regarding delay and Doppler frequency. The prolate spheroidal coordinate system is chosen, since the description of the delay is only dependent on one coordinate. The equations reduce to a simpler form and, thus, save computing time when simulating the channel. Furthermore, the characteristic function can be determined in this coordinate representation, which is an important step to determine the temporal correlation in the channel.

Finally, the investigation in this thesis has shown that the presented model is very general and therefore can be applied both to the vehicle-to-vehicle and the air-to-air channel. The non-stationary behavior of the mobile-to-mobile channel is inherently included into the model.

Conclusions and Future Work

The use of time-variant probability density functions for mobile-to-mobile channels in order to describe non-stationary stochastic processes of the scattering is necessary in order to take the fast variations in the channel into account. Instead of using purely stochastic models based on the wide-sense stationary uncorrelated scattering assumption, geometric-stochastic models that do not fulfill the wide-sense stationary uncorrelated scattering assumption have to be employed.

Therefore, we intend to relate our model to the framework of non-wide-sense stationary uncorrelated scattering channels that has been proposed by Matz. A mathematical proof of the proportionality between the presented joint delay Doppler probability density function and the local scattering function is desired similar to the wide-sense stationary uncorrelated scattering case, so that the probability density functions can be used to simulate non-stationary channels.

Appendix A

WSSUS Correlation Functions [Pät02]

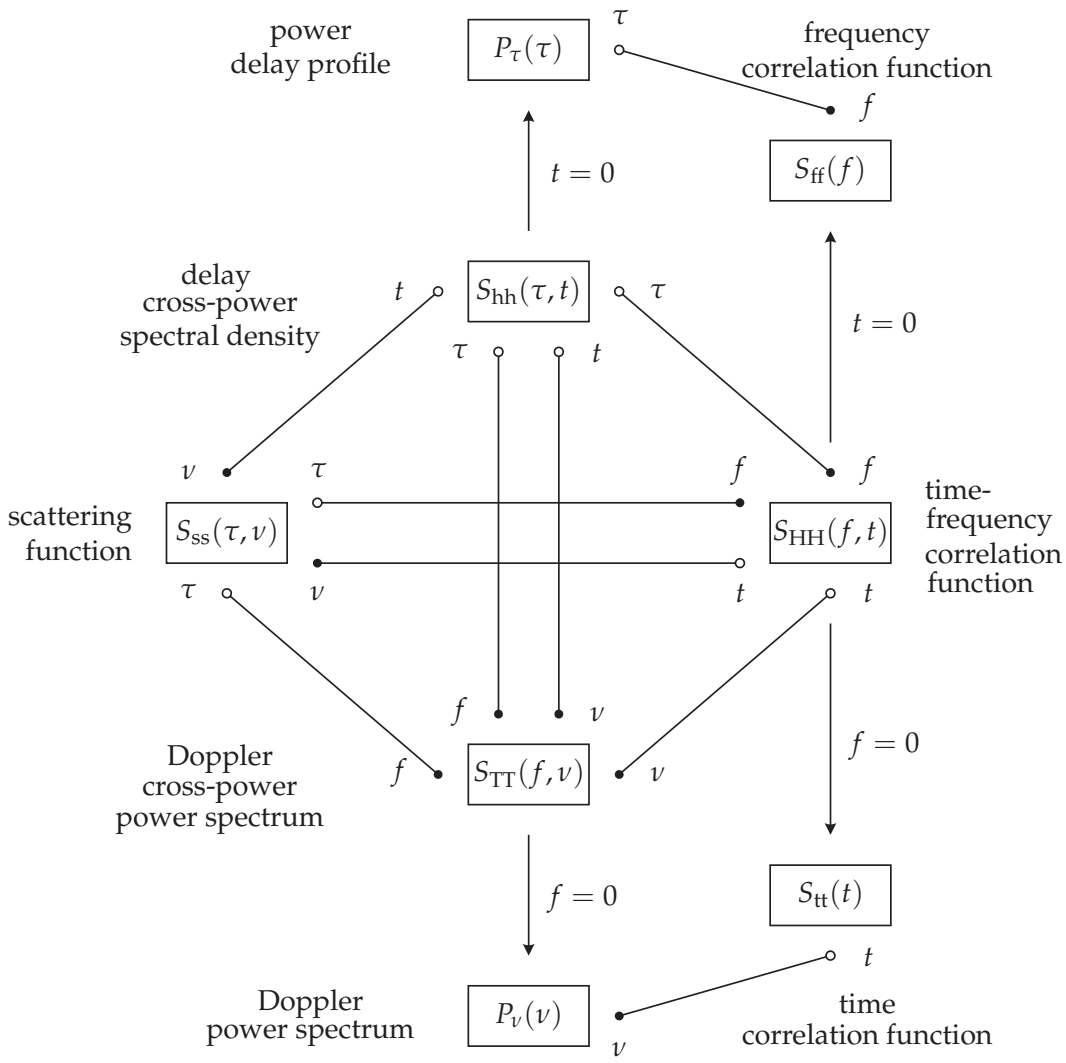

Appendix B

Doppler Frequency

B.1 Expressed in Cartesian Coordinates x

The Doppler frequency for arbitrary velocity vectors is given by

$$\begin{aligned}\nu(\mathbf{x},\mathbf{v}) = &\frac{(x-d_{\mathrm{t}}^{x})}{\sqrt{(x-d_{\mathrm{t}}^{x})^{2}+y^{2}+(z-h_{\mathrm{t}})^{2}}}\frac{v_{\mathrm{t}}^{x}}{c}f_{\mathrm{c}}\\ &+\frac{(x-d_{\mathrm{r}}^{x})}{\sqrt{(x-d_{\mathrm{r}}^{x})^{2}+y^{2}+(z-h_{\mathrm{r}})^{2}}}\frac{v_{\mathrm{r}}^{x}}{c}f_{\mathrm{c}}\\ &+\frac{y}{\sqrt{(x-d_{\mathrm{t}}^{x})^{2}+y^{2}+(z-h_{\mathrm{t}})^{2}}}\frac{v_{\mathrm{t}}^{y}}{c}f_{\mathrm{c}}\\ &+\frac{y}{\sqrt{(x-d_{\mathrm{r}}^{x})^{2}+y^{2}+(z-h_{\mathrm{r}})^{2}}}\frac{v_{\mathrm{r}}^{y}}{c}f_{\mathrm{c}}\\ &+\frac{(z-h_{\mathrm{t}})}{\sqrt{(x-d_{\mathrm{t}}^{x})^{2}+y^{2}+(z-h_{\mathrm{t}})^{2}}}\frac{v_{\mathrm{t}}^{z}}{c}f_{\mathrm{c}}\\ &+\frac{(z-h_{\mathrm{r}})}{\sqrt{(x-d_{\mathrm{r}}^{x})^{2}+y^{2}+(z-h_{\mathrm{r}})^{2}}}\frac{v_{\mathrm{r}}^{z}}{c}f_{\mathrm{c}}\,,\end{aligned} \tag{B.1}$$

where h_{t} and h_{r} are the z-coordinates of the aircraft. d_{t}^{x} and d_{r}^{x} are the x-coordinates, respectively.

B.2 Expressed in Ellipse Parameter ϕ

The Doppler frequency in dependence on the parameter ϕ is obtained by inserting the ellipse equation of (4.16) into (B.1). We get for the Doppler frequency $\nu(\phi|\tau)$ the following expression

$$\begin{aligned}
\nu(\phi|\tau) = & \frac{(a_\tau \cos\phi + x_\mathrm{c} - d_\mathrm{t}^x)}{\sqrt{(a_\tau \cos\phi + x_\mathrm{c} - d_\mathrm{t}^x)^2 + (b_\tau \sin\phi + y_\mathrm{c})^2 + h_\mathrm{t}^2}} \frac{v_\mathrm{t}^x}{c} f_\mathrm{c} \\
& + \frac{(a_\tau \cos\phi + x_\mathrm{c} - d_\mathrm{r}^x)}{\sqrt{(a_\tau \cos\phi + x_\mathrm{c} - d_\mathrm{r}^x)^2 + (b_\tau \sin\phi + y_\mathrm{c})^2 + h_\mathrm{r}^2}} \frac{v_\mathrm{r}^x}{c} f_\mathrm{c} \\
& + \frac{b_\tau \sin\phi + y_\mathrm{c}}{\sqrt{(a_\tau \cos\phi + x_\mathrm{c} - d_\mathrm{t}^x)^2 + (b_\tau \sin\phi + y_\mathrm{c})^2 + h_\mathrm{t}^2}} \frac{v_\mathrm{t}^y}{c} f_\mathrm{c} \\
& + \frac{b_\tau \sin\phi + y_\mathrm{c}}{\sqrt{(a_\tau \cos\phi + x_\mathrm{c} - d_\mathrm{r}^x)^2 + (b_\tau \sin\phi + y_\mathrm{c})^2 + h_\mathrm{r}^2}} \frac{v_\mathrm{r}^y}{c} f_\mathrm{c} \\
& - \frac{h_\mathrm{t}}{\sqrt{(a_\tau \cos\phi + x_\mathrm{c} - d_\mathrm{t}^x)^2 + (b_\tau \sin\phi + y_\mathrm{c})^2 + h_\mathrm{t}^2}} \frac{v_\mathrm{t}^z}{c} f_\mathrm{c} \\
& - \frac{h_\mathrm{r}}{\sqrt{(a_\tau \cos\phi + x_\mathrm{c} - d_\mathrm{r}^x)^2 + (b_\tau \sin\phi + y_\mathrm{c})^2 + h_\mathrm{r}^2}} \frac{v_\mathrm{r}^z}{c} f_\mathrm{c} \,.
\end{aligned} \tag{B.2}$$

B.3 Expressed in Algebraic Parameter s

The Doppler frequency in dependence on the parameter s is obtained by inserting the ellipse equation of (4.46) into (B.2). We get for the Doppler frequency $\nu(s|\tau)$ the following expression

$$
\begin{aligned}
\nu(s|\tau) = & \frac{\left(a_\tau \frac{1-s^2}{1+s^2} + x_\mathrm{c} - d_\mathrm{t}^x\right)}{\sqrt{\left(a_\tau \frac{1-s^2}{1+s^2} + x_\mathrm{c} - d_\mathrm{t}^x\right)^2 + \left(b_\tau \frac{2s}{1+s^2} + y_\mathrm{c}\right)^2 + h_\mathrm{t}^2}} \frac{v_\mathrm{t}^x}{c} f_\mathrm{c} \\
& + \frac{\left(a_\tau \frac{1-s^2}{1+s^2} + x_\mathrm{c} - d_\mathrm{r}^x\right)}{\sqrt{\left(a_\tau \frac{1-s^2}{1+s^2} + x_\mathrm{c} - d_\mathrm{r}^x\right)^2 + \left(b_\tau \frac{2s}{1+s^2} + y_\mathrm{c}\right)^2 + h_\mathrm{r}^2}} \frac{v_\mathrm{r}^x}{c} f_\mathrm{c} \\
& + \frac{b_\tau \frac{2s}{1+s^2} + y_\mathrm{c}}{\sqrt{\left(a_\tau \frac{1-s^2}{1+s^2} + x_\mathrm{c} - d_\mathrm{t}^x\right)^2 + \left(b_\tau \frac{2s}{1+s^2} + y_\mathrm{c}\right)^2 + h_\mathrm{t}^2}} \frac{v_\mathrm{t}^y}{c} f_\mathrm{c} \\
& + \frac{b_\tau \frac{2s}{1+s^2} + y_\mathrm{c}}{\sqrt{\left(a_\tau \frac{1-s^2}{1+s^2} + x_\mathrm{c} - d_\mathrm{r}^x\right)^2 + \left(b_\tau \frac{2t}{1+s^2} + y_\mathrm{c}\right)^2 + h_\mathrm{r}^2}} \frac{v_\mathrm{r}^y}{c} f_\mathrm{c} \\
& - \frac{h_\mathrm{t}}{\sqrt{\left(a_\tau \frac{1-s^2}{1+s^2} + x_\mathrm{c} - d_\mathrm{t}^x\right)^2 + \left(b_\tau \frac{2s}{1+s^2} + y_\mathrm{c}\right)^2 + h_\mathrm{t}^2}} \frac{v_\mathrm{t}^z}{c} f_\mathrm{c} \\
& - \frac{h_\mathrm{r}}{\sqrt{\left(a_\tau \frac{1-s^2}{1+s^2} + x_\mathrm{c} - d_\mathrm{r}^x\right)^2 + \left(b_\tau \frac{2s}{1+s^2} + y_\mathrm{c}\right)^2 + h_\mathrm{r}^2}} \frac{v_\mathrm{r}^z}{c} f_\mathrm{c} \,.
\end{aligned}
\tag{B.3}
$$

B.4 Indefinite Integral in Algebraic Parameter s

$$\int \sqrt{1-\epsilon_\tau^2\left(\frac{1-s^2}{1+s^2}\right)^2}\,\frac{2}{1+s^2}\,\mathrm{d}s = s\sqrt{\frac{(s^2+1)^2-\epsilon_\tau^2\,(s^2-1)^2}{(s^2+1)^2}} - \tag{B.4}$$
$$\Bigg[\left(\mathrm{j}\,(\epsilon_\tau+1)\left(s^2+1\right)\sqrt{\frac{-\epsilon_\tau s^2+\epsilon_\tau+s^2+1}{\epsilon_\tau+1}}\sqrt{-\frac{\epsilon_\tau\,(s^2-1)+s^2+1}{\epsilon_\tau-1}}\right.$$
$$\sqrt{\frac{(s^2+1)-\epsilon_\tau^2\,(s^2-1)^2}{(s^2+1)^2}}\left\{(\epsilon_\tau+1)\,\mathrm{E}\left(\mathrm{j}\sinh^{-1}\left(\sqrt{\frac{\epsilon_\tau+1}{1-\epsilon_\tau}}s\right)\middle|\frac{(\epsilon_\tau-1)^2}{(\epsilon_\tau+1)^2}\right)-\right.$$
$$\left.\left.2\mathrm{K}\left(\mathrm{j}\sinh^{-1}\left(\sqrt{\frac{\epsilon_\tau+1}{1-\epsilon_\tau}}s\right)\middle|\frac{(\epsilon_\tau-1)^2}{(\epsilon_\tau+1)^2}\right)\right\}\right]\Bigg/$$
$$\left(\sqrt{\frac{\epsilon_\tau+1}{1-\epsilon_\tau}}\left(\epsilon_\tau^2\left(s^2-1\right)^2-\left(s^2+1\right)^2\right)\right),$$

where $\sinh^{-1}(s)$ is the inverse hyperbolic sine function, $\mathrm{K}(\phi|k)$ is the incomplete elliptic integral of the first kind and $\mathrm{E}(\phi|k)$ is the incomplete elliptic integral of the second kind with parameter k [AS65]. Without loss of generality the integration constant is assumed to be zero.

Appendix C

Doppler Frequency Derivative

In order to calculate the delay-dependent Doppler pdf $p(\nu|\tau)$ we need to calculate the derivative to transform the pdf $p(\phi|\tau)$. In order to shorten the nomenclature, we set $d_{\mathrm{t}2} = d_{\mathrm{t}}^x - x_{\mathrm{c}}$ and $d_{\mathrm{r}2} = d_{\mathrm{r}}^x - x_{\mathrm{c}}$. The derivative of the Doppler frequency $\frac{d\nu}{d\phi}$ results in

$$\begin{aligned}
\frac{\mathrm{d}\nu}{\mathrm{d}\phi} = & \frac{\sin\phi\left(b_\tau^2 d_{\mathrm{t}2}\cos\phi - a_\tau\left(b_\tau^2 + h_{\mathrm{t}}^2\right)\right)}{\left(\left(a_\tau\cos\phi - d_{\mathrm{t}2}\right)^2 + \left(b_\tau\sin\phi\right)^2 + h_{\mathrm{t}}^2\right)^{3/2}}\frac{v_{\mathrm{t}}^x}{c}f_{\mathrm{c}} \\
& + \frac{\sin\phi\left(b_\tau^2 d_{\mathrm{r}2}\cos\phi - a_\tau\left(b_\tau^2 + h_{\mathrm{r}}^2\right)\right)}{\left(\left(a_\tau\cos\phi - d_{\mathrm{r}2}\right)^2 + \left(b_\tau\sin\phi\right)^2 + h_{\mathrm{r}}^2\right)^{3/2}}\frac{v_{\mathrm{r}}^x}{c}f_{\mathrm{c}} \\
& + \frac{b_\tau\left(2\cos\phi\left(a_\tau^2 + d_{\mathrm{t}2}^2 + h_{\mathrm{t}}^2\right) - a_\tau d_{\mathrm{t}2}\left(\cos 2\phi + 3\right)\right)}{2\left(\left(a_\tau\cos\phi - d_{\mathrm{t}2}\right)^2 + \left(b_\tau\sin\phi\right)^2 + h_{\mathrm{t}}^2\right)^{3/2}}\frac{v_{\mathrm{t}}^y}{c}f_{\mathrm{c}} \\
& + \frac{b_\tau\left(2\cos\phi\left(a_\tau^2 + d_{\mathrm{r}2}^2 + h_{\mathrm{r}}^2\right) - a_\tau d_{\mathrm{r}2}\left(\cos 2\phi + 3\right)\right)}{2\left(\left(a_\tau\cos\phi - d_{\mathrm{r}2}\right)^2 + \left(b_\tau\sin\phi\right)^2 + h_{\mathrm{r}}^2\right)^{3/2}}\frac{v_{\mathrm{r}}^y}{c}f_{\mathrm{c}} \\
& + \frac{h_{\mathrm{t}}\sin\phi\left(\left(b_\tau^2 - a_\tau^2\right)\cos\phi + a_\tau d_{\mathrm{t}2}\right)}{\left(\left(a_\tau\cos\phi - d_{\mathrm{t}2}\right)^2 + \left(b_\tau\sin\phi\right)^2 + h_{\mathrm{t}}^2\right)^{3/2}}\frac{v_{\mathrm{t}}^z}{c}f_{\mathrm{c}} \\
& + \frac{h_{\mathrm{r}}\sin\phi\left(\left(b_\tau^2 - a_\tau^2\right)\cos\phi + a_\tau d_{\mathrm{r}2}\right)}{\left(\left(a_\tau\cos\phi - d_{\mathrm{r}2}\right)^2 + \left(b_\tau\sin\phi\right)^2 + h_{\mathrm{r}}^2\right)^{3/2}}\frac{v_{\mathrm{r}}^z}{c}f_{\mathrm{c}}\,.
\end{aligned} \tag{C.1}$$

The offset of the ellipse center from the origin of the coordinate system $x_{\mathrm{c}} = 0$, if the altitudes are the same. If the altitudes h_{t} and h_{r} are different, the delay ellipse can be offset from the origin. Therefore, x_{c} becomes nonzero, especially for large delays. In order to calculate the delay-dependent Doppler frequency pdf $p(\nu|\tau)$, (B.2) and (C.1) have to be inserted into (4.23).

Appendix D

Jakes Proof

The Doppler frequency for velocity components in the x-direction is given by

$$\begin{aligned}\nu(\phi|\tau) = &\frac{(a_\tau \cos\phi - d_{\mathrm{t}}^x)}{\sqrt{(a_\tau \cos\phi - d_{\mathrm{t}}^x)^2 + (b_\tau \sin\phi)^2}} \frac{v_{\mathrm{t}}^x}{c} f_{\mathrm{c}} \\ &+ \frac{(a_\tau \cos\phi - d_{\mathrm{r}}^x)}{\sqrt{(a_\tau \cos\phi - d_{\mathrm{r}}^x)^2 + (b_\tau \sin\phi)^2}} \frac{v_{\mathrm{r}}^x}{c} f_{\mathrm{c}} \,.\end{aligned} \tag{D.1}$$

If $\tau \to \infty$, the ellipse becomes a circle and the foci coincide at the origin, the semi-major and the semi-minor axis become the same

$$\lim_{\tau\to\infty} b_\tau = a_\tau \qquad \text{for } a_\tau \gg d_{\mathrm{t}}^x,\, d_{\mathrm{r}}^x \,. \tag{D.2}$$

We define the maximum Doppler frequency as

$$f_{\mathrm{m}} = (v_{\mathrm{t}}^x + v_{\mathrm{r}}^x)\, \frac{f_{\mathrm{c}}}{c} \tag{D.3}$$

For $\tau \to \infty$, (D.1) converges to a well-known expression

$$\begin{aligned}\lim_{\tau\to\infty} \nu(\phi|\tau) &= \frac{a_\tau \cos\phi}{\sqrt{a_\tau^2 \left((\cos\phi)^2 + (\sin\phi)^2\right)}} \frac{v_{\mathrm{t}}^x}{c} f_{\mathrm{c}} + \frac{a_\tau \cos\phi}{\sqrt{a_\tau^2 \left((\cos\phi)^2 + (\sin\phi)^2\right)}} \frac{v_{\mathrm{r}}^x}{c} f_{\mathrm{c}} \\ &= (v_{\mathrm{t}}^x + v_{\mathrm{r}}^x)\, \frac{f_{\mathrm{c}}}{c} \cos\phi = \cos\phi f_{\mathrm{m}} \,.\end{aligned} \tag{D.4}$$

In order to calculate the pdf of the Doppler frequency, the following derivative needs to be computed as

$$\begin{aligned}\lim_{\tau\to\infty}\frac{\mathrm{d}\nu}{\mathrm{d}\phi} &= \lim_{\tau\to\infty}\frac{b_\tau^2\sin\phi\,(d_\mathrm{t}^x\cos\phi-a_\tau)}{\left((a_\tau\cos\phi-d_\mathrm{t}^x)^2+(b_\tau\sin\phi)^2\right)^{3/2}}\frac{v_\mathrm{t}^x}{c}f_\mathrm{c}\\ &+\frac{b_\tau^2\sin\phi\,(d_\mathrm{r}^x\cos\phi-a_\tau)}{\left((a_\tau\cos\phi-d_\mathrm{r}^x)^2+(b_\tau\sin\phi)^2\right)^{3/2}}\frac{v_\mathrm{r}^x}{c}f_\mathrm{c}\\ &=\frac{-a_\tau^3\sin\phi}{\left(a_\tau^2\left((\cos\phi)^2+(\sin\phi)^2\right)\right)^{3/2}}\frac{v_\mathrm{t}^x}{c}f_\mathrm{c}\\ &+\frac{-a_\tau^3\sin\phi}{\left(a_\tau^2\left((\cos\phi)^2+(\sin\phi)^2\right)\right)^{3/2}}\frac{v_\mathrm{r}^x}{c}f_\mathrm{c}\\ &=-\left(v_\mathrm{t}^x+v_\mathrm{r}^x\right)\frac{f_\mathrm{c}}{c}\sin\phi=-\sin\phi f_\mathrm{m}\,.\end{aligned}\tag{D.5}$$

Note that for $\tau\to\infty$ the distribution $p(\phi|\tau)$ becomes

$$\lim_{\tau\to\infty}p(\phi|\tau)=\frac{\sqrt{1-\epsilon_\tau^2\cos^2\phi}}{\int_0^{2\pi}\sqrt{1-\epsilon_\tau^2\cos^2\zeta}\,\mathrm{d}\zeta}=\frac{1}{2\pi}\,.\tag{D.6}$$

Finally, the delay-dependent pdf of the Doppler frequency becomes

$$\begin{aligned}\lim_{\tau\to\infty}p(\nu|\tau)&=\sum_{\nu=1}^{2}\frac{1}{2\pi\left|-\left(v_\mathrm{t}^x+v_\mathrm{r}^x\right)\frac{f_\mathrm{c}}{c}\sin\phi_\nu\right|}=\sum_{\nu=1}^{2}\frac{1}{2\pi\left|f_\mathrm{m}\sin\phi_\nu\right|}\\ &=\frac{1}{\pi\left|f_\mathrm{m}\sin\left(\arccos\left(\frac{\nu}{f_\mathrm{m}}\right)\right)\right|}=\frac{1}{\pi f_\mathrm{m}\sqrt{1-\left(\frac{\nu}{f_\mathrm{m}}\right)^2}}\end{aligned}\tag{D.7}$$

which can be recognized as Jakes spectrum. □

Appendix E

Simulation Parameters

Table E.1. *Simulation parameters for the presented V2V and A2A scenarios*

Parameter	I	II	III	IV	V	VI	VII	VIII	IX	X	XI	XII
d_t [m]	−50	−50	−20	−102	93	−1175	−1790	−1175	−1175	−1243	−2876	−949
d_r [m]	50	50	20	102	−93	1175	640	1175	1175	1199	1007	961
v_t^x [km/h]	90	90	30	31	30	250	250	250	250	287	267	163
v_t^y [km/h]	0	0	0	−0.6	0.6	0	0	0	0	0	0	−178
v_t^z [km/h]	—	—	—	—	—	0	0	0	0	0	0	0
v_r^x [km/h]	90	−90	30	−30	−28	250	250	−250	250	254	256	182
v_r^y [km/h]	0	0	0	0.6	−0.5	0	0	0	0	0	0	199
v_r^z [km/h]	—	—	—	—	—	0	0	0	0	0	0	0
h_t [m]	—	—	—	—	—	600	1600	600	600	597	1748	605
h_r [m]	—	—	—	—	—	600	600	600	600	576	612	598
d_LOS [m]	100	100	40	204	186	2350	2627	2350	2350	2442	4046	1910
Δ_1 [m]	0	0	1.875	3.75	3.75	—	—	—	—	—	—	—
Δ_2 [m]	∞	∞	9.375	11.25	11.75							
Δ_3 [m]	0	0	5.625	3.75	3.75	—	—	—	—	—	—	—
Δ_4 [m]	∞	∞	13.125	11.25	11.75	—	—	—	—	—	—	—
κ	—	—	—	—	—	—	—	—	0.5	—	—	1.5
$\bar{\varphi}$ [rad]	—	—	—	—	—	—	—	—	$\pi/4$	—	—	$-\pi/4$

Acronyms and Symbols

List of Acronyms

ADS-B	automatic dependent surveillance-broadcast	31
AGC	automatic gain control	34
AeMC	aeromedical center	47
AOA	angle of arrival	29
AOD	angle of departure	52
A2A	air-to-air	3
AWGN	additive white Gaussian noise	9
DAB	digital audio broadcasting	41
CCF	channel correlation function	22
CIR	channel impulse response	27
CW	continuous wave	40
DC	direct current	35
DGUS	deterministic Gaussian uncorrelated scattering	23
DLR	Deutsches Zentrum für Luft- und Raumfahrt	42
DPS	Doppler power spectrum	15
DRU	digital receiving unit	34
DSRC	dedicated short-range communications	27
DU	doubly-underspread	22
EASA	European Aviation Safety Agency	40
EIRP	effective isotropically radiated power	37
ERP	effective radiated power	42
F2M	fixed-to-mobile	2

GPS	global positioning system	35
GLSF	generalized local scattering function	59
GSCM	geometric-stochastic channel model	4
ICAO	International Civil Aviation Organization	31
IFR	instrument flight rules	42
IGI	Ingenieursgesellschaft für Interfaces	35
ITS	intelligent transportation system	2
KIAS	knots indicated airspeed	43
KTAS	knots true airspeed	43
LNA	low-noise amplifier	38
LPFRS	low cost and profile frequency rubidium standard	35
LSF	local scattering function	22
LOS	line-of-sight	8
MIMO	multiple-input/multiple-output	29
M2M	mobile-to-mobile	1
OFDM	orthogonal frequency division multiplexing	34
PDP	power delay profile	25
pdf	probability density function	3
PSCS	prolate spheroidal coordinate system	75
PTS	portable transmitting station	34
QWSSUS	quasi-wide-sense stationary uncorrelated scattering	59
RFT	radio-frequency tuner	34
RX	receiver	1
SISO	single input/single output	46
STC	supplemental type certificate	40
STFT	short-time Fourier transform	21
SR	specular reflection	10
SUV	suburban utility vehicle	37
TX	transmitter	1
UAV	unmanned aerial vehicle	2

US	uncorrelated scattering	14
UUV	unmanned underwater vehicle	2
WAVE	wireless access in vehicular environments	27
VDL	VHF data link	31
VFR	visual flight rules	42
VHF	very-high frequency	30
VSWR	voltage standing wave ratio	40
V2V	vehicle-to-vehicle	3
WSS	wide-sense stationary	14
WSSUS	wide-sense stationary uncorrelated scattering	3

List of Symbols

f	continuous frequency variable	13
f_c	carrier frequency	9
$f_\mathrm{d,max}$	maximum achievable Doppler frequency	16
f_IF	intermediate frequency	34
f_m	Doppler frequency caused by movement of TX and RX	119
f_r	Doppler frequency caused by movement of receiver	51
f_t	Doppler frequency caused by movement of transmitter	51
f_σ	3 dB cut off frequency	19
G	antenna gain	40
G_r	receive antenna gain	9
G_t	transmit antenna gain	9
$g(\cdot)$	zero mean real continuous time deterministic Gaussian process	23
$g_p(\cdot)$	real deterministic Gaussian process of the p-th path	25
$H(\cdot,\cdot)$	time-variant transfer function	13
$\hat{H}[\cdot,\cdot]$	discrete estimated time-variant transfer function	37
$h(\cdot,\cdot)$	time-variant impulse response	9
h_r	altitude of receiver	41
h_t	altitude of transmitter	41
$h_\mathrm{dir}(\cdot,\cdot)$	time-variant impulse response of direct path	9
$h_\mathrm{ref}(\cdot,\cdot)$	time-variant impulse response of reflected paths	9
$h_\mathrm{sc}(\cdot,\cdot)$	time-variant impulse response of scattered paths	9
h_η	scale factor for η-coordinate	77
h_ϑ	scale factor for ϑ-coordinate	77
h_ξ	scale factor for ξ-coordinate	77
$\mathrm{I}_n(\cdot)$	n-th order modified Bessel function of the first kind	17
$\mathrm{J}_n(\cdot)$	n-th order Bessel function of the first kind	51
K	Ricean K factor	21
$\mathrm{K}(k)$	complete elliptic integral of the first kind	51
$\mathrm{K}(\phi\|k)$	incomplete elliptic integral of the second kind	116
L_f	focus distance	76
L_τ	delay-dependent circumference of ellipse	57
N	number of harmonic functions of $g(t)$	24
N_b	block size of FFT	37
N_p	number of harmonic functions of $g_p(t)$	25
N_ref	number of reflected paths	10
N_sc	number of scattered paths	11
$n(\cdot)$	additive white Gaussian noise	9

P_t	transmit power	33
$P_\nu(\cdot)$	Doppler power spectrum	15
$P_\tau(\cdot)$	power delay profile	25
$p(\cdot)$	Doppler probability density function	15
$p(\cdot,\cdot)$	joint probability density function	15
$p(\cdot\|\cdot)$	conditional probability density function	15
$\bar{p}(\cdot;\cdot,\cdot)$	averaged joint probability density function	67
Q	number of sub-carriers	37
$\mathrm{Q}_n(\cdot)$	Legendre function of the second kind	51
$r_\mathrm{HH}(\cdot,\cdot;\cdot,\cdot)$	frequency time auto-correlation function	14
$r_\mathrm{hh}(\cdot,\cdot;\cdot,\cdot)$	delay time auto-correlation function	14
$r_\mathrm{ss}(\cdot,\cdot;\cdot,\cdot)$	delay Doppler auto-correlation function	14
$r_\mathrm{TT}(\cdot,\cdot;\cdot,\cdot)$	frequency Doppler auto-correlation function	14
$S_\mathrm{HH}(\cdot,\cdot)$	time-frequency correlation function	111
$S_\mathrm{ff}(\cdot)$	frequency correlation function	111
$S_\mathrm{hh}(\cdot,\cdot)$	delay cross-power spectral density	111
$S_\mathrm{ss}(\cdot,\cdot)$	scattering function	15
$S_\mathrm{tt}(\cdot)$	time correlation function	111
$S_\mathrm{TT}(\cdot,\cdot)$	Doppler cross-power spectrum	111
$s(\cdot,\cdot)$	spreading function	12
$\hat{s}[\cdot,\cdot]$	discrete estimated spreading function	37
$T(\cdot,\cdot)$	Doppler-variant transfer function	13
T_g	periodic transmit interval	36
t	continuous time variable	9
t^*	fixed time instant	55
$\mathbf{v}$	velocity vector	16
$\mathbf{v}_\mathrm{r}$	velocity vector of receiver	53
v_max	maximum velocity	42
$\mathbf{v}_\mathrm{t}$	velocity vector of transmitter	53
v_r^x	x-component of velocity vector of receiver	53
v_r^y	y-component of velocity vector of receiver	53
v_r^z	z-component of velocity vector of receiver	78
v_t^x	x-component of velocity vector of transmitter	53
v_t^y	y-component of velocity vector of transmitter	53
v_t^z	z-component of velocity vector of transmitter	78
w_i	weight factors	67
$\mathbf{x}$	position vector	53

$\Phi_{nn}(\cdot)$	noise power spectral density in frequency domain	11
$\bar{\phi}$	mean scattering direction	93
$\phi_{i(+)}, \phi_{i(-)}$	intersection points of ellipse with scattering belt	67
$\bar{\varphi}$	mean angle	93
ϕ_{0i}, ϕ_{1i}	start and end point of integral	67
φ_n	Doppler phase of the n-th component	24
φ_{r}	azimuth angle of arrival	10
φ_{t}	azimuth angle of departure	10

$(\cdot)^*$	complex conjugate	14
$*$	convolution	51
$(\cdot)^{\mathrm{T}}$	transpose of a vector or matrix	53
$\lvert\cdot\rvert$	absolute value	16
$\lVert\cdot\rVert$	L^2-norm of a vector or matrix	16
$\partial/\partial t$	partial derivative with respect to t	55
∇	vector differential operator	55
$\mathbb{E}\{\cdot\}$	expected value operator	14

References

[ABB+07] P. Almers, E. Bonek, A. Burr, N. Czink, M. Debbah, V. Degli-Esposti, H. Hofstetter, P. Kyösti, D. Laurenson, G. Matz, A. F. Molisch, C. Oestges, and H. Özcelik. Survey of Channel and Radio Propagation Models for Wireless MIMO Systems. *EURASIP Journal on Wireless Communications and Networking*, 2007(1):1–19, February 2007.

[Abh90] S. S. Abhyankar. *Algebraic Geometry for Scientists and Engineers*. Mathematical Surveys and Monographs. American Mathematical Society, Providence, RI, USA, 1990.

[ABK02] A. Abdi, J. A. Barger, and M. Kaveh. A Parametric Model for the Distribution of the Angle of Arrival and the Associated Correlation Function and Power Spectrum at the Mobile Station. *IEEE Transactions on Vehicular Technology*, 51(3):425–434, May 2002.

[AH86] A. S. Akki and F. Haber. A Statistical Model of Mobile-to-Mobile Land Communication Channel. *IEEE Transactions on Vehicular Technology*, 35(1):2–7, February 1986.

[AI06] G. Acosta and M. A. Ingram. Model Development for the Wideband Expressway Vehicle-to-Vehicle 2.4 GHz Channel. In *Proceedings IEEE Wireless Communications and Networking Conference (WCNC)*, pages 1283–1288, Las Vegas, NV, USA, April 2006.

[AK98] A. Abdi and M. Kaveh. A New Velocity Estimator for Cellular Systems Based on Higher Order Crossings. In *Proceedings 32nd Asilomar Conference on Signals, Systems and Computers*, pages 1423–1427, Pacific Grove, CA, USA, November 1998.

[Akk94] A. S. Akki. Statistical Properties of Mobile-to-Mobile Land Communication Channels. *IEEE Transactions on Vehicular Technology*, 43(4):826–831, November 1994.

[AKT+11] T. Abbas, J. Karedal, F. Tufvesson, A Paier, L. Bernadó, and A. F. Molisch. Directional Analysis of Vehicle-to-Vehicle Propagation Channels. In *Proceedings IEEE 73rd Vehicular Technology Conference (VTC Spring)*, pages 1–5, Yokohama, Japan, May 2011.

[All66] D. W. Allan. Statistics of Atomic Frequency Standards. *Proceedings of the IEEE*, 54(2):221–230, February 1966.

[AMI06] G. Acosta-Marum and M. A. Ingram. A BER-Based Partitioned Model for a 2.4 GHz Vehicle-to-Vehicle Expressway Channel. *Wireless Personal Communications*, 37(3-4):421–443, 2006.

[AMI07] G. Acosta-Marum and M. A. Ingram. Six Time- and Frequency-Selective Empirical Channel Models for Vehicular Wireless LANs. In *Proceedings IEEE 66th Vehicular Technology Conference (VTC Fall)*, pages 2134–2138, Baltimore, MD, USA, October 2007.

[ANBS10] M. Alsehaili, S. Noghanian, D. A. Buchanan, and A. R. Sebak. Angle-of-Arrival Statistics of a Three-Dimensional Geometrical Scattering Channel Model for Indoor and Outdoor Propagation Environments. *IEEE Antennas and Wireless Propagation Letters*, 9:946–949, 2010.

[AP11] N. Avazov and M. Pätzold. A Geometric Street Scattering Channel Model for Car-to-Car Communication Systems. In *Proceedings International Conference on Advanced Technologies for Communications (ATC)*, pages 224–230, Da Nang, Vietnam, August 2011.

[AS65] M. Abramowitz and I. A. Stegun. *Handbook of Mathematical Functions: With Formulas, Graphs, and Mathematical Tables*. Applied mathematics series. Dover Publications, Mineola, NY, USA, 1965.

[ATI04] G. Acosta, K. Tokuda, and M. A. Ingram. Measured Joint Doppler-Delay Power Profiles for Vehicle-to-Vehicle Communications at 2.4 GHz. In *Proceedings IEEE Global Telecommunications Conference (GLOBECOM)*, pages 3813–3817, Dallas, TX, USA, November 2004.

[AWL08] J. An, Y. Wu, and G. Liu. Delay and Doppler Shift Joint Tracking Method for OFDM Based Aeronautical Communication Systems. In

Proceedings 4th International Conference on Wireless Communications, Networking and Mobile Computing (WiCOM), pages 1–4, Dalian, China, October 2008.

[BD91] W. R. Braun and U. Dersch. A Physical Mobile Radio Channel Model. *IEEE Transactions on Vehicular Technology*, 40(2):472–482, May 1991.

[Bel63] P. A. Bello. Characterization of Randomly Time-Variant Linear Channels. *IEEE Transactions on Communications*, 11(4):360–393, December 1963.

[Bel73] P. A. Bello. Aeronautical Channel Characterization. *IEEE Transactions on Communications*, 21(5):548–563, May 1973.

[Ber12] L. Bernadó. *Non-Stationarity in Vehicular Wireless Channels*. PhD thesis, Technische Universität Wien, Vienna, Austria, April 2012.

[Boa92] B. Boashash. Estimating and Interpreting the Instantaneous Frequency of a Signal–Part I: Fundamentals. *Proceedings of the IEEE*, 80(4):520–538, April 1992.

[BP12] A. Borhani and M. Pätzold. Modeling of Vehicle-to-Vehicle Channels in the Presence of Moving Scatterers. In *Proceedings IEEE 76th Vehicular Technology Conference (VTC Fall)*, pages 1–5, Quebec City, QC, Canada, September 2012.

[BP13] A. Borhani and M. Pätzold. A Non-Stationary One-Ring Scattering Model. In *Proceedings IEEE Wireless Communications and Networking Conference (WCNC)*, pages 2620–2625, Shanghai, China, April 2013.

[BS87] P. Beckmann and A. Spizzichino. *The Scattering of Electromagnetic Waves from Rough Surfaces*. Artech House, London, UK, 1987.

[BSMM07] I. N. Bronstein, K. A. Semendyayev, G. Musiol, and H. Mühlig. *Handbook of Mathematics*. Springer, Berlin, Germany, 2007.

[Bul02] R. J. C. Bultitude. Estimating Frequency Correlation Functions from Propagation Measurements on Fading Radio Channels: A Critical Review. *IEEE Journal on Selected Areas in Communications*, 20(6):1133–1143, August 2002.

[BZP+09] L. Bernadó, T. Zemen, A. Paier, J. Karedal, and B. H. Fleury. Parametrization of the Local Scattering Function Estimator for Vehicular-to-Vehicular Channels. In *Proceedings IEEE 70th Vehicular Technology Conference (VTC Fall)*, pages 1–5, Anchorage, AK, USA, September 2009.

[BZT+12] L. Bernadó, T. Zemen, F. Tufvesson, A. F. Molisch, and C. F. Mecklenbräuker. The (in-) Validity of the WSSUS Assumption in Vehicular Radio Channels. In *Proceedings IEEE 23rd International Symposium on Personal, Indoor and Mobile Radio Communications (PIMRC)*, pages 1757–1762, Sydney, NSW, Australia, September 2012.

[BZT+14] L. Bernadó, T. Zemen, F. Tufvesson, A. F. Molisch, and C. F. Mecklenbräuker. Delay and Doppler Spreads of Nonstationary Vehicular Channels for Safety-Relevant Scenarios. *IEEE Transactions on Vehicular Technology*, 63(1):82–93, January 2014.

[CHBS08] L. Cheng, B. Henty, F. Bai, and D. D. Stancil. Doppler Spread and Coherence Time of Rural and Highway Vehicle-to-Vehicle Channels at 5.9 GHz. In *Proceedings IEEE Global Telecommunications Conference (GLOBECOM)*, pages 1–6, New Orleans, LA, USA, November 2008.

[CK97] R. H. Clarke and W. L. Khoo. 3-D Mobile Radio Channel Statistics. *IEEE Transactions on Vehicular Technology*, 46(3):798–799, August 1997.

[CKZ+10] N. Czink, F. Kaltenberger, Y. Zhou, L. Bernadó, T. Zemen, and X. Yin. Low-Complexity Geometry-Based Modeling of Diffuse Scattering. In *Proceedings 4th European Conference on Antennas and Propagation (EuCAP)*, pages 1–4, Barcelona, Spain, April 2010.

[Cla68] R. H. Clarke. A Statistical Theory of Mobile-Radio Reception. *Bell System Technical Journal*, 47(6):957–1000, July/August 1968.

[Coo] Cooper Antennas website. http://www.cooperantennas.com.

[CP09] A. Chelli and M. Pätzold. The Impact of Fixed and Moving Scatterers on the Statistics of MIMO Vehicle-to-Vehicle Channels. In *Proceedings IEEE 69th Vehicular Technology Conference (VTC Spring)*, pages 1–6, Barcelona, Spain, April 2009.

[CP11] A. Chelli and M. Pätzold. A Non-Stationary MIMO Vehicle-to-Vehicle Channel Model Derived from the Geometrical Street Model. In *Proceedings IEEE 74th Vehicular Technology Conference (VTC Fall)*, pages 1–6, San Francisco, CA, USA, September 2011.

[CSB13] L. Cheng, D. D. Stancil, and F. Bai. A Roadside Scattering Model for the Vehicle-to-Vehicle Communication Channel. *IEEE Journal on Selected Areas in Communications*, 31(9):449–459, September 2013.

[CWL09a] X. Cheng, C.-X. Wang, and D. I. Laurenson. A Geometry-Based Stochastic Model for Wideband MIMO Mobile-to-Mobile Channels. In *Proceedings IEEE Global Telecommunications Conference (GLOBECOM)*, pages 1–6, Honolulu, HI, USA, November 2009.

[CWL+09b] X. Cheng, C.-X. Wang, D. I. Laurenson, S. Salous, and A. V. Vasilakos. An Adaptive Geometry-Based Stochastic Model for Non-Isotropic MIMO Mobile-to-Mobile Channels. *IEEE Transactions on Wireless Communications*, 8(9):4824–4835, September 2009.

[CYW+13] X. Cheng, Q. Yao, M. Wen, C.-X. Wang, L.-Y. Song, and B.-L. Jiao. Wideband Channel Modeling and Intercarrier Interference Cancellation for Vehicle-to-Vehicle Communication Systems. *IEEE Journal on Selected Areas in Communications*, 31(9):434–448, September 2013.

[DG97] G. Dyer and T. G. Gilbert. Channel Sounding Measurements in the VHF A/G Radio Communications Channel, December 1997.

[DW96] L. Darian and W. Wilson. VHF Channel Propagation Measurements. RTCA doc. RTCA/SC-172/WG2/WP147, August 1996.

[Fai89] M. Failli. Digital Land Mobile Radio Communications COST 207. Technical report, European Commission, 1989.

[Gab46] D. Gabor. Theory of Communication. *Journal of the IEE*, 93(26):429–457, November 1946.

[Gan72] M. J. Gans. A Power-Spectral Theory of Propagation in the Mobile-Radio Environment. *IEEE Transactions on Vehicular Technology*, 21(1):27–38, February 1972.

[Gli08] S. Gligorevic. Joint Channel Estimation and Equalisation of Fast Time-Varying Frequency-Selective Channels. *European Transactions on Telecommunications*, 19(1):1–13, 2008.

[Gli13] S. Gligorevic. Airport Surface Propagation Channel in the C-Band: Measurements and Modeling. *IEEE Transactions on Antennas and Propagation*, 61(9):4792–4802, September 2013.

[GR00] I. S. Gradshteyn and I. M. Ryzhik. *Table of Integrals, Series, and Products*. Academic Press, San Diego, CA, USA, 2000.

[Haa02] E. Haas. Aeronautical Channel Modeling. *IEEE Transactions on Vehicular Technology*, 51(2):254–264, March 2002.

[HH99] P. Hoeher and E. Haas. Aeronautical Channel Modeling at VHF-band. In *Proceedings IEEE 50th Vehicular Technology Conference (VTC Fall)*, pages 1961–1966, Amsterdam, Netherlands, September 1999.

[HM11] F. Hlawatsch and G. Matz. *Wireless Communications over Rapidly Time-Varying Channels*. Academic Press, Oxford, UK, 2011.

[Hoe92] P. Hoeher. A Statistical Discrete-Time Model for the WSSUS Multipath Channel. *IEEE Transactions on Vehicular Technology*, 41(4):461–468, November 1992.

[Höh11] P. A. Höher. *Grundlagen der digitalen Informationsübertragung: Von der Theorie zu Mobilfunkanwendungen*. Springer Vieweg, Wiesbaden, Germany, 2011.

[HPYK05] B. O. Hogstad, M. Pätzold, N. Youssef, and D. Kim. A MIMO Mobile-To-Mobile Channel Model: Part II — The Simulation Model. In *Proceedings IEEE 16th International Symposium on Personal, Indoor and Mobile Radio Communications (PIMRC)*, pages 562–567, Berlin, Germany, September 2005.

[IEE10] IEEE Standard for Information technology – Local and Metropolitan Area Networks– Specific Requirements– Part 11: Wireless LAN Medium Access Control (MAC) and Physical Layer (PHY) Specifications Amendment 6: Wireless Access in Vehicular Environments, July 2010.

[Jak94] W. C. Jakes. *Microwave Mobile Communications*. IEEE press classic reissue. Wiley, New York, NY, USA, 1994.

[KP08] J. Kunisch and J. Pamp. Wideband Car-to-Car Radio Channel Measurements and Model at 5.9 GHz. In *Proceedings IEEE 68th Vehicular Technology Conference (VTC Fall)*, pages 1–5, Calgary, BC, Canada, September 2008.

[KTC+09a] J. Karedal, F. Tufvesson, N. Czink, A. Paier, C. Dumard, T. Zemen, C. F. Mecklenbräuker, and A. F. Molisch. A Geometry-Based Stochastic MIMO Model for Vehicle-to-Vehicle Communications. *IEEE Transactions on Wireless Communications*, 8(7):3646–3657, July 2009.

[KTC+09b] J. Karedal, F. Tufvesson, N. Czink, A. Paier, C. Dumard, T. Zemen, C. F. Mecklenbräuker, and A. F. Molisch. Measurement-Based Modeling of Vehicle-to-Vehicle MIMO Channels. In *Proceedings IEEE International Conference on Communications (ICC)*, pages 1–6, Dresden, Germany, June 2009.

[LLZ+08] M. Li, K. Lu, H. Zhu, M. Chen, S. Mao, and B. Prabhakaran. Robot Swarm Communication Networks: Architectures, Protocols, and Applications. In *Proceedings 3rd International Conference on Communications and Networking in China (ChinaCom)*, pages 162–166, Hangzhou, China, August 2008.

[Mat03a] G. Matz. Characterization of Non-WSSUS Fading Dispersive Channels. In *Proceedings IEEE International Conference on Communications (ICC)*, pages 2480–2484, Anchorage, AK, USA, May 2003.

[Mat03b] G. Matz. Doubly Underspread Non-WSSUS Channels: Analysis and Estimation of Channel Statistics. In *Proceedings IEEE 4th Workshop on Signal Processing Advances in Wireless Communications (SPAWC)*, pages 190–194, Rome, Italy, June 2003.

[Mat05] G. Matz. On Non-WSSUS Wireless Fading Channels. *IEEE Transactions on Wireless Communications*, 4(5):2465–2478, September 2005.

[Mat08] D. W. Matolak. Channel Modeling for Vehicle-to-Vehicle Communications. *IEEE Communications Magazine*, 46(5):76–83, May 2008.

[Mat12] D. W. Matolak. Air-Ground Channels & Models: Comprehensive Review and Considerations for Unmanned Aircraft Systems. In *Proceedings IEEE Aerospace Conference*, pages 1–17, Big Sky, MT, USA, March 2012.

[Mau05] J. Maurer. *Strahlenoptisches Kanalmodell für die Fahrzeug-Fahrzeug-Funkkommunikation*. PhD thesis, Institut für Höchstfrequenztechnik und Elektronik (IHE), Universität Karlsruhe (TH), Karlsruhe, Germany, July 2005. (published in German).

[Med] Medav website. http://www.channelsounder.de.

[MF85] W. Martin and P. Flandrin. Wigner-Ville Spectral Analysis of Nonstationary Processes. *IEEE Transactions on Acoustics, Speech, and Signal Processing*, 33(6):1461–1470, December 1985.

[MFSW04] J. Maurer, T. Fügen, T. Schäfer, and W. Wiesbeck. A New Inter-Vehicle Communications (IVC) Channel Model. In *Proceedings IEEE 60th Vehicular Technology Conference (VTC Fall)*, pages 9–13, Los Angeles, CA, USA, September 2004.

[MFW02] J. Maurer, T. Fügen, and W. Wiesbeck. Narrow-Band Measurement and Analysis of the Inter-Vehicle Transmission Channel at 5.2 GHz. In *Proceedings IEEE 55th Vehicular Technology Conference (VTC Spring)*, pages 1274–1278, Birmingham, AL, USA, May 2002.

[MH06] G. Matz and F. Hlawatsch. Nonstationary Spectral Analysis Based on Time-Frequency Operator Symbols and Underspread Approximations. *IEEE Transactions on Information Theory*, 52(3):1067–1086, March 2006.

[MHRR12] D. Medina, F. Hoffmann, F. Rossetto, and C.-H. Rokitansky. A Geographic Routing Strategy for North Atlantic In-Flight Internet Access Via Airborne Mesh Networking. *IEEE/ACM Transactions on Networking*, 20(4):1231–1244, August 2012.

[Mil] Current version of MIL-STD-810. http://www.atec.army.mil/publications/Mil-Std-810G/Mil-Std-810G.pdf.

[ML11] Y. S. Meng and Y. H. Lee. Measurements and Characterizations of Air-to-Ground Channel Over Sea Surface at C-Band With Low Airborne Altitudes. *IEEE Transactions on Vehicular Technology*, 60(4):1943–1948, May 2011.

[MMK+11] C. F. Mecklenbräuker, A. F. Molisch, J. Karedal, F. Tufvesson, A. Paier, L. Bernadó, T. Zemen, O. Klemp, and N. Czink. Vehicular Channel Characterization and Its Implications for Wireless System Design and Performance. *Proceedings of the IEEE*, 99(7):1189–1212, July 2011.

[Mob] Mobile Mark website. http://www.mobilemark.com.

[MS14] D. W. Matolak and R. Sun. Air-Ground Channel Characterization for Unmanned Aircraft Systems: The Hilly Suburban Environment. In *Proceedings IEEE 80th Vehicular Technology Conference (VTC Fall)*, pages 1–5, Vancouver, BC, Canada, September 2014.

[MSX08] D. W. Matolak, I. Sen, and W. Xiong. The 5-GHz Airport Surface Area Channel—Part I: Measurement and Modeling Results for Large Airports. *IEEE Transactions on Vehicular Technology*, 57(4):2014–2026, July 2008.

[MT14] A. F. Molisch and F. Tufvesson. Propagation Channel Models for Next-Generation Wireless Communications Systems. *IEICE Transactions on Communications*, 97-B(10):2022–2034, 2014.

[MTKM09] A. F. Molisch, F. Tufvesson, J. Karedal, and C. F. Mecklenbräuker. A Survey on Vehicle-to-Vehicle Propagation Channels. *IEEE Wireless Communications Magazine*, 16(6):12–22, December 2009.

[MW09] D. W. Matolak and Q. Wu. Vehicle-to-Vehicle Channels: Are We Done Yet? In *IEEE Global Communications Conference Workshop (GLOBECOM)*, pages 1–6, Honolulu, HI, USA, November 2009.

[NA98] O. Nørklit and J. B. Andersen. Diffuse Channel Model and Experimental Results for Array Antennas in Mobile Environments. *IEEE Transactions on Antennas and Propagation*, 46(6):834–840, June 1998.

[Nak60] N. Nakagami. *The m-Distribution-A General Formula for Intensity Distribution of Rapid Fading*. Pergamon Press, Oxford, UK, 1960.

[NMD+03] W. G. Newhall, R. Mostafa, C. Dietrich, C. R. Anderson, K. Dietze, G. Joshi, and J. H. Reed. Wideband Air-to-Ground Radio Channel Measurements Using an Antenna Array at 2 GHz for Low-Altitude Operations. In *Proceedings Military Communications Conference (MILCOM)*, pages 1422–1427, Monterey, CA, USA, October 2003.

[NR02] W. G. Newhall and J. H. Reed. A Geometric Air-to-Ground Radio Channel Model. In *Proceedings Military Communications Conference (MILCOM)*, pages 632–636, Anaheim, CA, USA, October 2002.

[ODC09] M. M. Olama, S. M. Djouadi, and C. D. Charalambous. Stochastic Differential Equations for Modeling, Estimation and Identification of Mobile-to-Mobile Communication Channels. *IEEE Transactions on Wireless Communications*, 8(4):1754–1763, April 2009.

[OHN+10] U. A. K. C. Okonkwo, S. Z. M. Hashim, R. Ngah, N. F. Nanyan, and T. A. Rahman. Time-Scale Domain Characterization of Nonstationary Wideband Vehicle-to-Vehicle Propagation Channel. In *Proceedings IEEE Asia-Pacific Conference on Applied Electromagnetics (APACE)*, pages 1–6, Port Dickson, Malaysia, November 2010.

[Ong03] K. P. Ong. *Signal Processing for Airborne Bistatic Radar*. PhD thesis, University of Edinburgh, Edinburgh, UK, 2003.

[Pai10] A. Paier. *The Vehicular Radio Channel in the 5 GHz Band*. PhD thesis, Institut für Nachrichtentechnik und Hochfrequenztechnik (E389), Vienna University of Technology, 2010.

[Par00] J. D. Parsons. *The Mobile Radio Propagation Channel*. Wiley, Chichester, UK, 2000.

[Pät02] M. Pätzold. *Mobile Fading Channels*. Wiley, Chichester, UK, 2002.

[PB82] J. D. Parsons and A. S. Bajwa. Wideband Characterisation of Fading Mobile Radio Channels. *IEE Proceedings F (Communications, Radar and Signal Processing),*, 129(2):95, April 1982.

[PHY08] M. Pätzold, B. O. Hogstad, and N. Youssef. Modeling, Analysis, and Simulation of MIMO Mobile-to-Mobile Fading Channels. *IEEE Transactions on Wireless Communications*, 7(2):510–520, February 2008.

[PHYK05] M. Pätzold, B. O. Hogstad, N. Youssef, and D. Kim. A MIMO Mobile-To-Mobile Channel Model: Part I – The Reference Model. In *Proceedings IEEE 16th International Symposium on Personal, Indoor and Mobile Radio Communications (PIMRC)*, pages 573–578, Berlin, Germany, September 2005.

[PKC+07a] A. Paier, J. Karedal, N. Czink, H. Hofstetter, C. Dumard, T. Zemen, F. Tufvesson, C. F. Mecklenbräuker, and A. F. Molisch. First Results from Car-to-Car and Car-to-Infrastructure Radio Channel Measurements at 5.2 GHz. In *Proceedings IEEE 18th International Symposium on*

Personal, Indoor and Mobile Radio Communications (PIMRC), pages 1–5, Athens, Greece, September 2007.

[PKC+07b] A. Paier, J. Karedal, N. Czink, H. Hofstetter, C. Dumard, T. Zemen, F. Tufvesson, A. F. Molisch, and C. F. Mecklenbräuker. Car-to-Car Radio Channel Measurements at 5 GHz: Pathloss, Power-Delay Profile, and Delay-Doppler Spectrum. In *Proceedings 4th International Symposium on Wireless Communication Systems (ISWCS)*, pages 224–228, Trondheim, Norway, October 2007.

[PKLL98] M. Pätzold, U. Killat, F. Laue, and Y. Li. On the Statistical Properties of Deterministic Simulation Models for Mobile Fading Channels. *IEEE Transactions on Vehicular Technology*, 47(1):254–269, February 1998.

[PP02] A. Papoulis and S. U. Pillai. *Probability, Random Variables, and Stochastic Processes*. McGraw-Hill electrical and electronic engineering series. McGraw-Hill, New York, NY, USA, 2002.

[Pro00] J. G. Proakis. *Digital Communications*. McGraw-Hill, New York, NY, USA, 2000.

[PRR02] P. Petrus, J. H. Reed, and T. S. Rappaport. Geometrical-Based Statistical Macrocell Channel Model for Mobile Environments. *IEEE Transactions on Communications*, 50(3):495–502, March 2002.

[PSP05] C. S. Patel, G. L. Stüber, and T. G. Pratt. Simulation of Rayleigh-Faded Mobile-to-Mobile Communication Channels. *IEEE Transactions on Communications*, 53(11):1876–1884, November 2005.

[PWK+08] P. Paschalidis, M. Wisotzki, A. Kortke, W. Keusgen, and M. Peter. A Wideband Channel Sounder for Car-to-Car Radio Channel Measurements at 5.7 GHz and Results for an Urban Scenario. In *Proceedings IEEE 68th Vehicular Technology Conference (VTC Fall)*, pages 1–5, Calgary, BC, Canada, September 2008.

[PZB+08] A. Paier, T. Zemen, L. Bernadó, G. Matz, J. Karedal, N. Czink, C. Dumard, F. Tufvesson, A. F. Molisch, and C. F. Mecklenbräuker. Non-WSSUS Vehicular Channel Characterization in Highway and Urban Scenarios at 5.2 GHZ Using the Local Scattering Function. In *International ITG Workshop on Smart Antennas (WSA)*, pages 9–15, Darmstadt, Germany, February 2008.

[RC99] B. Roturier and B. Chateau. A General Model for VHF Aeronautical Multipath Propagation Channel. AMCP doc. AMCP/WG-D/WP6, Honolulu, HI, USA, January 1999.

[Ric44] S. O. Rice. Mathematical Analysis of Random Noise. *Bell System Technical Journal*, 23(3):282–332, July 1944.

[Ric45] S. O. Rice. Mathematical Analysis of Random Noise. *Bell System Technical Journal*, 24(1):46–156, January 1945.

[Sch89] H. Schulze. Stochastische Modelle und digitale Simulation von Mobilfunkkanälen. *Kleinheubacher Berichte*, 32:473–483, 1989.

[Sep] Septentrio website. http://www.septentrio.com.

[SK98] J. S. Sadowsky and V. Kafedziski. On the Correlation and Scattering Functions of the WSSUS Channel for Mobile Communications. *IEEE Transactions on Vehicular Technology*, 47(1):270–282, February 1998.

[SM08a] I. Sen and D. W. Matolak. The 5-GHz Airport Surface Area Channel—Part II: Measurement and Modeling Results for Small Airports. *IEEE Transactions on Vehicular Technology*, 57(4):2027–2035, July 2008.

[SM08b] I. Sen and D. W. Matolak. Vehicle-Vehicle Channel Models for the 5-GHz Band. *IEEE Transactions on Intelligent Transportation Systems*, 9(2):235–245, June 2008.

[SN11] R. Sivakami and G. M. K. Nawaz. Secured Communication for MANETS in Military. In *Proceedings International Conference on Computer, Communication and Electrical Technology (ICCCET)*, pages 146–151, Tirunelveli, India, March 2011.

[Sta08] D. Stacey. *Aeronautical Radio Communication Systems and Networks*. Wiley, Chichester, UK, first edition, 2008.

[TAG03] C. Tepedelenlioğlu, A. Abdi, and G. B. Giannakis. The Ricean *K* Factor: Estimation and Performance Analysis. *IEEE Transactions on Wireless Communications*, 2(4):799–810, July 2003.

[Tem] Rubidium atomic clock website. http://www.spectratime.com.

[TGZ96] M. K. Tsatsanis, G. B. Giannakis, and G. Zhou. Estimation and Equalization of Fading Channels with Random Coefficients. In *Proceedings*

IEEE International Conference on Acoustics, Speech, and Signal Processing (ICASSP), pages 1093–1096, Atlanta, GA, USA, May 1996.

[VLC62] W. C. Vergara, J. Levatich, and T. J. Carroll. VHF Air-Ground Propagation Far Beyond the Horizon and Tropospheric Stability. *IRE Transactions on Antennas and Propagation*, 10(5):608–621, September 1962.

[vM18] R. von Mises. Über die "Ganzzahligkeit" der Atomgewichte und verwandte Fragen. *Physikalische Zeitschrift*, 19:490–500, 1918.

[WCL09] C.-X. Wang, X. Cheng, and D. I. Laurenson. Vehicle-to-Vehicle Channel Modeling and Measurements: Recent Advances and Future Challenges. *IEEE Communications Magazine*, 47(11):96–103, November 2009.

[WFS10] M. Walter, N. Franzen, and M. Schnell. New Concepts for a Decentralized, Self-Organizing Air-to-Air Radio Link. In *Proceedings IEEE/AIAA 29th Digital Avionics Systems Conference (DASC)*, pages 3.D.1–1–3.D.1–12, Salt Lake City, UT, USA, October 2010.

[WFZ14] M. Walter, U.-C. Fiebig, and A. Zajić. Experimental Verification of the Non-Stationary Statistical Model for V2V Scatter Channels. In *Proceedings IEEE 80th Vehicular Technology Conference (VTC Fall)*, pages 1–5, Vancouver, BC, Canada, September 2014.

[WGDS10] M. Walter, S. Gligorević, T. Detert, and M. Schnell. UHF/VHF Air-to-Air Propagation Measurements. In *Proceedings 4th European Conference on Antennas and Propagation (EuCAP)*, pages 1–5, Barcelona, Spain, April 2010.

[WS11] M. Walter and M. Schnell. The Doppler-Delay Characteristic of the Aeronautical Scatter Channel. In *Proceedings IEEE 74th Vehicular Technology Conference (VTC Fall)*, pages 1–5, San Francisco, CA, USA, September 2011.

[WSF14a] M. Walter, D. Shutin, and U.-C. Fiebig. Delay-Dependent Doppler Probability Density Functions for Vehicle-to-Vehicle Scatter Channels. *IEEE Transactions on Antennas and Propagation*, 62(4):2238–2249, April 2014.

[WSF14b] M. Walter, D. Shutin, and U.-C. Fiebig. Joint Delay Doppler Probability Density Functions for Air-to-Air Channels. *International Journal of Antennas and Propagation*, 2014:1–11, 2014.

[WSF15] M. Walter, D. Shutin, and U.-C. Fiebig. Prolate Spheroidal Coordinates for Modeling Mobile-to-Mobile Channels. *IEEE Antennas and Wireless Propagation Letters*, 14:155–158, 2015.

[YWC+14] Y. Yuan, C.-X. Wang, X. Cheng, B. Ai, and D. I. Laurenson. Novel 3D Geometry-Based Stochastic Models for Non-Isotropic MIMO Vehicle-to-Vehicle Channels. *IEEE Transactions on Wireless Communications*, 13(1):298–309, January 2014.

[Zaj12] A. Zajić. *Mobile-to-Mobile Wireless Channels*. Artech House, Boston, MA, USA, first edition, 2012.

[Zaj14] A. G. Zajić. Impact of Moving Scatterers on Vehicle-to-Vehicle Narrowband Channel Characteristics. *IEEE Transactions on Vehicular Technology*, 63(7):3094–3106, September 2014.

[ZS08] A. G. Zajić and G. L. Stüber. Three-Dimensional Modeling, Simulation, and Capacity Analysis of Space-Time Correlated Mobile-to-Mobile Channels. *IEEE Transactions on Vehicular Technology*, 57(4):2042–2054, July 2008.

[ZS09] A. G. Zajić and G. L. Stüber. Three-Dimensional Modeling and Simulation of Wideband MIMO Mobile-to-Mobile Channels. *IEEE Transactions on Wireless Communications*, 8(3):1260–1275, March 2009.

[ZSPN08] A. G. Zajić, G. L. Stüber, T. G. Pratt, and S. Nguyen. Statistical Modeling and Experimental Verification of Wideband MIMO Mobile-to-Mobile Channels in Highway Environments. In *Proceedings IEEE 19th International Symposium on Personal, Indoor and Mobile Radio Communications (PIMRC)*, pages 1–5, Cannes, France, September 2008.

[ZWGL12] Y. Zhou, X. Wang, A. Guo, and F. Liu. Channel Characterization and Simulation Modeling of Diffuse Scattering in Highway Mobile Communications. *Journal of Information and Computational Science*, 9(2):293–303, 2012.

[ZXZJ14] R. Zhao, C. Xu, M. Zhao, and G. Jia. A Novel Broadband Model for MIMO Vehicle-to-Vehicle Fading Channel. *Journal of Computational Information Systems*, 10(2):573–580, 2014.